Investigation and Manipulation of Thin Oxide Films Supported on Metal Single Crystals

A Scanning Tunneling Microscopy Study

D I S S E R T A T I O N

zur Erlangung des akademischen Grades

Doctor rerum naturalium
(Dr. rer. nat)

im Fach Physik

eingereicht am
Fachbereich Physik der Freien Universität Berlin

von
Diplom Physiker **Jan-Frederik Karl Jerratsch**

im
März 2011

Abstract

Thin oxide films are complex systems that have attracted great scientific interest over the past decades. They do not only allow to model and study the physical and chemical properties of bulk oxide materials but also display distinct properties of their own right. Two aspects are of particular interest: the physical and chemical properties of the films themselves and their ability to support small metal particles on top or even inside the oxide matrix. Therefore thin oxide films are models for real oxide systems used in catalysis. The aim of this study is to deepen the understanding of two distinct oxide-film systems using the scanning tunneling microscope. The systems that have been investigated are an ultrathin silica film grown on a molybdenum (112) single crystal and a ceria film grown on a ruthenium (0001) single crystal.

In the first part of this thesis it is shown that the silica film is a suitable model for an atomic sieve. While some smaller atoms such as palladium, silver, lithium and iron can penetrate the regular pores of the film and bind to the metal-oxide interface, larger atoms such as gold cannot. This property of the thin silica film is then further exploited to tailor the physical and chemical properties of the system. It is shown using scanning tunneling microscopy and scanning tunneling spectroscopy that the work function of the silica/Mo system shifts monotonously to smaller values upon incorporation of lithium atoms at the metal-oxide interface. This is shown to have dramatic consequences on the adsorption behavior of the system: whereas gold is unable to bind to the pristine silica film it can form particles of various sizes on the modified adsorption system. The new adsorption mechanism is described in terms of charging and a local polaronic distortion of the oxide structure. Furthermore the silica/Mo system is used to store single iron atoms in the pore structure of the oxide. It is demonstrated that the single iron atoms remain dispersed as single atomic features even at non-cryogenic temperatures and that they retain a magnetic moment.

In the second part of this thesis new insights into the local electronic structure of the ceria film are presented. It is demonstrated that strongly localized Ce $4f$-states within the bandgap are accessible with tunneling spectroscopy measurements. This experimental possibility yields a new understanding of the electron localization upon oxygen-defect creation in this film which is crucial for the understanding of the unique catalytic properties of this system. Beyond that also new findings regarding the polarity of different step edges and line defects are presented along with the implications for their local electronic structure. In the last part of this thesis the adsorption of vanadium on ceria is discussed.

Zusammenfassung

Dünne Oxid-Filme sind komplexe Systeme, die über die letzten Jahrzehnte beachtliches wissenschaftliches Interesse genossen haben. Sie dienen nicht nur als Modellsysteme für die entsprechenden Oxid-Einkristalle, sondern offenbaren auch interessante eigene Eigenschaften. Vor allem zwei Aspekte sind dabei von grossem Interesse: Die physikalischen und chemischen Eigenschaften der Oxid-Filme selbst und ihre Fähigkeit Metallpartikel auf der Oberfläche oder sogar im Film zu adsorbieren. Das Ziel dieser Arbeit ist die Vertiefung des Verständnisses von zwei speziellen Oxid-Filmen mit Hilfe des Raster-Tunnel-Mikroskops (RTM). Die beiden Systeme sind Silica, gewachsen auf einem Molybdän Einkristall und Ceria, gewachsen auf einem Ruthenium Einkristall.

Im ersten Teil dieser Arbeit wird gezeigt, dass der Silica-Film ein Modell für ein atomares Sieb darstellt. Kleinere Atome, wie Pd, Ag, Li und Fe können in die Poren des Films eindringen, während grössere Atome wie Au nur an Defekten binden.

Diese Eigenschaft des Silica-Films wird im Weiteren genutzt um die physikalischen und chemischen Eigenschaften zu beeinflussen. Positive Lithium-ionen an der Metall-Oxid Grenzfläche führen zu einer Absenkung der Austrittsarbeit des Systems. Das wiederum hat dramatische Konsequenzen auf das Adsorptionsverhalten des Films: Gold kann nun auf dem Film stabilisiert werden. Dieser neue Bindungsmechanismus wird anhand einer elektrostatisch vermittelten Gitterverbiegung erklärt.

Darüberhinaus wird die Oxidmatrix genutzt um monoatomare magnetische Einheiten zu stabilisieren. Es kann gezeigt werden, dass einzelne Eisenatome stabil in den Film gebunden werden und ein magnetisches Moment behalten.

Im zweiten Teil dieser Arbeit werden neue Erkenntnisse bezüglich der lokalen elektronischen Struktur von Ceria-Filmen präsentiert. Stark lokalisierte Ce $4f$-Zustände können mit Hilfe des RTM nachgewiesen werden, was ein neues Verständniss der Elektronen-Lokalisierung nach Defektformation erlaubt. Darüberhinaus werden die Eigenschaften ultra dünner Filme diskutiert und Ergebnisse bezüglich der Polarität verschiedener Stufenkanten vorgestellt. Im weiteren werden Unterschiede zwischen stochiometrischen und reduzierten Ceria-Filmen aus einer RTM-Perspektive beschrieben.

Im letzten Teil dieser Arbeit werden Experimente zur Adsorption von Vanadium auf dünnen Ceria-Filmen vorgestellt und die Formation von charackteristischen Adsorbatgrössen reproduziert und diskutiert.

Contents

Contents

1 Introduction

Oxide materials play an important role in many commercial applications such as design of new materials, coating, sensor technology, microelectronics and heterogeneous catalysis. Therefore great efforts have been made to investigate the properties of oxide materials. For a comprehensive understanding of chemical processes a characterization down to the atomic level is required. Hence the application of powerful surface science techniques plays a vital role. Many off those spectroscopic and microscopic techniques require a conductive sample and a flat, accessible, macroscopic surface. In this context the use of thin oxide films supported on metal single-crystals has been proven to be a fruitful approach [1–9]. Many surface science techniques such as X-Ray Diffraction (XRD), Infrared Absorption Spectroscopy (IRAS), Ultraviolet and X-Ray Photoelectron Spectroscopy (UPS/XPS), Auger Electron Spectroscopy (Auger), Low Energy Electron Diffraction (LEED) or Temperature Programmed Desorption (TPD) provide valuable information regarding the structural, chemical and electronic properties of surfaces. However all these methods average over a macroscopic area of the sample surface and are therefore not suitable to characterize the local properties of the surface.

In order to investigate the local structural and electronic behavior, scanning probe methods such as scanning tunneling microscopy (STM) and atomic force microscopy (AFM) provide the possibility to study these properties with a sub nanometer lateral resolution. Beyond the characterization of the bare oxide surface, also the structural and electronic properties of metal adsorbates may be studied. Such metal-oxide model systems yield valuable insights into the working principle of real catalysts that are not accessible with most investigation techniques [10].

While oxide films mimic some properties of their bulk counterparts and are therefore suitable model-systems for the understanding of bulk oxides, they also display unique properties of their own. The contact to the metal substrate underneath, the limited thickness and the symmetry breaking at the surface have many interesting consequences for the properties of thin oxide films. In certain cases the thin film displays a different crystal structure than its bulk counterpart due to the influence of the metal substrate. This is the case for alumina grown on a NiAl single crystal [11], but also for the mono layer silica film grown on Mo(112) that is discussed in this thesis. For very thin oxide films also electron tunneling from the substrate into adsorbates on the film might be possible and thus a charging of adsorbates with suitable affinity levels occurs [12, 13]. This effect has been found to be a unique property of ultra thin films of up to five monolayers, which vanishes for thicker films. Obviously the charging has consequences for many chemical and physical properties of the adsorbate system including its catalytic properties. Recently it has been found that a monolayer FeO film on a platinum single crystal dramatically enhances the CO oxidation rate while a thick

magnetite (Fe_3O_4) film does not [14].

For this thesis the STM has been used to study structural, electronic and chemical properties of thin oxide films on metal supports with various adsorbates relevant for heterogeneous catalysis. The results are presented in the following chapters. Wherever results from different theory groups are available they are also included and interpreted in the light of the experimental results.

The first system investigated for this thesis is a monolayer silica (SiO_2) film grown on a molybdenum single-crystal. The chemical properties of this thin film have been tailored using the implementation of lithium atoms into the metal-oxide interface. The lithium atoms become positively charged and induce a dipole. The resulting system offers new chemical interaction possibilities. The special characteristics of this system have also been used to store single-atom magnetic units in a stable and inert environment. This possibility yields new insights with regards to ultra-small magnetic units for information storage. The results on the silica system are presented in chapter 4.

The second system that has been investigated for this thesis is a ceria (CeO_2) film grown on a ruthenium single-crystal. This system is known to readily store or release oxygen during a chemical reaction due to its rather similar energy in the reduced and the oxidized state. This makes ceria an important support for active metal nanoparticles in heterogeneous catalysis. The reducibility that leads to occupied and empty cerium *4f*-states has been investigated locally using STM and STS. Those results are found in chapter 5. Vanadium oxide species play a major role in catalysts for selective oxidation reactions [15–18]. Therefore the structural and chemical properties of VO_x species supported on ceria are of great interest. The results of the experiments with vanadium on ceria are presented in section 5.3 of chapter 5.

2 Description of the Experimental Methods

Investigating things that are too small to be seen with the human eye has been of interest for mankind for a long time. In the late 16th century the first operational optical microscope was developed by the dutch lens grinders Hans and Zacharias Janssen by simply placing two lenses in a tube. They realized an idea first described by Roger Bacon in 1267 [19]. After the telescope that was used for large, remote objects, optical microscopes provided the first possibility to overcome the limits of the human eye and explore the microscopic world. However optical microscopes are limited in their resolution due to the finite wavelength of light. This is described by Abbe's law [20]:

$$d = \frac{\lambda}{2nsin(\alpha)} \tag{2.1}$$

with d being the smallest distance of two distinguishable objects, λ the wavelength of light, n the refraction index and α half the aperture angle.

Assuming perfect conditions only objects with a distance of about 0.2 μm can be distinguished with an optical microscope, leaving objects of atomic dimensions way out of reach.

The development of electron microscopy by Ernst Ruska and others in the 1930's, using electrons with shorter wavelengths lowered this limit considerably into the nanometer range. However electron microscopes require vacuum and a rather complicated system of electron lenses. Furthermore, the highly energetic electrons interact with the sample surface and may cause damage to certain systems [21].

The idea of scanning a metal surface with a tip that changes its z-position according to the surface topography was first realized in 1972 by Young *et al.* [22]. The so called Topografiner uses the tip as a field emission electrode where the voltage between the tip and the sample is directly related to the spacing between the electrodes.

Roughly ten years later a breakthrough in the concept of scanning a metal tip over a sample surface has been achieved by Binnig and Rohrer in the IBM research labs in Rüschlikon, Switzerland. Making use of quantum mechanical tunneling they invented the STM [23]. Only a few years later, in 1987, they were awarded the nobel prize in physics together with Ernst Ruska, the pioneer of electron microscopy.

Quickly the STM became the standard tool to investigate the surface structure of metals and materials with a sufficiently small band gap at the atomic level. The ability to operate an STM in vacuum, ambient and even liquid environments makes it a powerful tool in many areas of research.

In recent years the concept has been further developed [24]. Today the STM is a local probe for many physical properties: the local density of states using scanning tunneling spectroscopy (STS) [25], magnetic properties using spin-polarized STM (SP-STM) [26], vibrational properties of adsorbed molecules using inelastic-electron-tunneling-Spectroscopy (IETS) [27], or optical properties using a photon emission STM (PSTM) [28, 29]. Furthermore the STM has been proven to be a powerful tool in order to investigate quantum conductance [30] and local bond formation between the tip-apex atom and a surface atom [31].

2.1 Scanning Tunneling Microscopy

The STM exploits the unique properties of quantum mechanical tunneling. The exponential dependence of the tunneling current on the distance of the two electrodes enables a very sensitive adjustment of this distance if the current is kept constant. In an STM one of those two electrodes is an atomically sharp, well defined metal tip and the other is the sample. Bringing the tip as close as a few Å to the surface and applying a bias of a few Volts a tunneling current starts to flow. In a simple picture, electrons can tunnel from the last atom of the metal tip into the sample. The resistivity of the tip-sample tunnel junction depends on the distance between the tip and the sample. This means that the tip will be positioned at a different height when scanning on top of a sample-surface atom than when scanning between sample-surface atoms. This leads to atomically resolved images of the sample-surface even for metal-surfaces with a small lattice constant and a small corrugation between adjacent atoms due to the delocalized electronic structure of a metal [32].

The setup of a simple STM as sketched in figure 2.1 consists of a piezo scan and positioning system with three degrees of freedom, an atomically sharp and conductive tip, a tunnel-current amplifier, a supply for the bias and an electronic feedback loop.

2.1.1 Imaging Modes of Operation of an STM

An STM can be operated in different imaging modes. In the following paragraphs the relevant modes are listed and briefly explained.

Constant Current Mode

In this mode the tunneling current is kept constant with a feedback loop. The tip distance to the sample surface is adjusted according to the current signal. Recording the z-position of the tip yields an image that shows a convolution of the sample topography
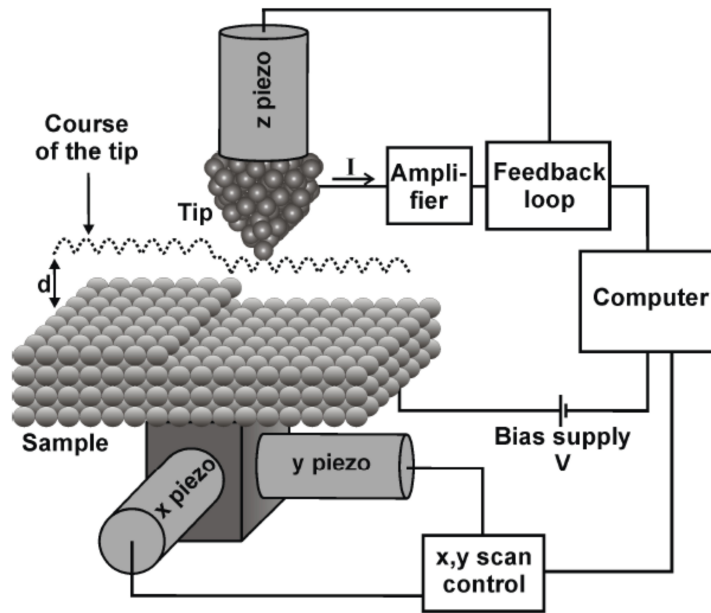
Figure 2.1: Working principle of an STM with an atomically sharp tip, a feedback loop system and positioning piezos. Adapted from [33].

and the available local density of states up to the given tunneling bias. The fact that the tip is positioned at a variable distance from the surface allows the scanning of surfaces with a rather large corrugation or adfeatures. This mode is the most common STM-imaging mode and all topography images in this thesis are recorded in this mode.

Constant Height Mode

In the constant height mode the feedback is disabled and the varying tunneling current is recorded. This yields an image of the surface that contains topographic as well as electronic information. It is important to know that this mode is only suitable for the scanning of small, rather flat areas because otherwise frequent tip crashes would be inevitable. On the other hand scanning can be fast in this modes because no feedback needs to react. This enables for instance the recording of STM movies with a millisecond time resolution.

2.1.2 Spectroscopy Modes of Operation of an STM

The tunneling current recorded with an STM depends critically on the local density of states (LDOS) of the surface at the position of the tip. Therefore the STM can be used to obtain local spectroscopic information of a surface. This allows to determine several electronic phenomena such as surface state onsets [34–36], electronic band gaps of semiconductor surfaces [37], superconductor band gaps [38], electronic structure of single atoms and small aggregates [39], the electronic gap between the highest occupied

and the lowest unoccupied orbital of a molecule (HOMO-LUMO gap) [5, 40], and band onsets in insulating films [5, 41, 42]. This long list of possible applications indicates the power of tunneling spectroscopy for various purposes.

The tunneling current represents the integrated LDOS from the Fermi-level up to the tunneling bias. In order to obtain the LDOS at a certain energy one is interested in the differentiated current, the $\frac{dI}{dV}$ signal.

Experimentally, local conductance spectra are obtained by placing the tip on top of the surface region of interest, e.g. an adatom or the pristine surface. Tunneling spectroscopy is performed with a lock-in-amplifier to modulate a high frequency sinusoidal signal onto the tunneling bias and directly read the $\frac{dI}{dV}$ response.

In the following paragraphs the relevant modes of Scanning Tunneling Spectroscopy are listed and briefly explained.

Differential Conductance Imaging

In order to maintain the capability to collect a stable constant current topography image the modulation frequency of the lock-in-amplifier is chosen well above the cut-off frequency of the feedback loop. By recording the in-phase current modulation with a lock-in amplifier, a laterally resolved spectroscopic signal $\frac{dI}{dV}$ is obtained simultaneously to the constant current topographic image. By comparing both, the topographic and the differential conductance images at various voltages one obtains informations about the LDOS at different areas of the surface, e.g. around an adsorbate or at the pristine surface.

Constant Distance $\frac{dI}{dV}$ Tunneling Spectroscopy

Constant distance $\frac{dI}{dV}$ tunneling spectroscopy is performed with a constant tip sample distance that depends on the setpoint conditions, e.g. the tunneling bias U_B and the tunneling current I_T. The feedback is turned off and the bias swept across the energy-region of interest. During this bias change the tunneling current I_T is recorded as a function of sample bias. This yields the I-U characteristic. Modulating the bias voltage during the sweep with a lock-in-amplifier allows for a direct measurement of the differential conductance signal $\frac{dI}{dV}$. Due to the exponential dependence of the transmission coefficient, the current signal might change over several orders of magnitude when ramping the bias over a large range. Therefore this technique is limited to a rather small bias range in one measurement, e.g. 1-3 V. If not mentioned otherwise all tunneling spectra shown in this thesis are recorded in the constant distance $\frac{dI}{dV}$ tunneling spectroscopy mode.

Linear Ramp $\frac{dI}{dV}$ Tunneling Spectroscopy

Linear ramp $\frac{dI}{dV}$ tunneling spectroscopy is performed by changing the tip-sample distance linearly during the bias sweep. This allows for a larger bias range to be covered

during one spectra. The problem of this method is to find the right slope for the linear ramp. Also in general the real tip-sample distance at a given time is not known. This technique has been successfully applied by Feenstra *et al.* [37, 43].

Constant Gap $\frac{dI}{dV}$ Tunneling Spectroscopy

During constant gap $\frac{dI}{dV}$ tunneling spectroscopy the bias and the current setpoint are being swept simultaneously in such a way that the resistance of the tunnel junction remains constant. During this spectroscopy the feedback remains active in order to adjust the tip-sample distance. This spectroscopy mode yields a signal proportional to the normalized differential conductance $\frac{dI}{dV}$. One has to be aware of the fact that the current set point goes to zero at the Fermi-level, thus this spectroscopy mode is unsuitable for measurements across or very close to the Fermi-level. This method has been applied by Kaiser *et al.* [44].

Constant Current $\frac{dI}{dV}$ Tunneling Spectroscopy

During constant current $\frac{dI}{dV}$ tunneling spectroscopy the feedback is switched on. This allows for a very large energy range to be covered without crashing the tip because the current is kept constant. Again it is not possible to cross the Fermi-level because zero-bias would lead to an infinitely small tip-sample distance and thus a tip crash. This method is used in particular in order to measure Field Emission Resonances (FER) [33, 45–47].

Ineleastic Tunneling Spectroscopy

Just like for the case of constant distance $\frac{dI}{dV}$ tunneling spectroscopy the bias is swept across the region of interest with the feedback turned off. Unlike for the other spectroscopy modes, the electrons are now able to excite a vibration for example in an adsorbate on the surface. Therefore the tunneling electrons lose energy in this mode. While the first derivative yields information about the LDOS, the second derivative yields information about vibrational modes of adsorbate species on the surface. This technique has been successfully applied by Ho *et al.* to study vibrational modes of single adsorbates [27] but also by Pascual *et al.* to induce motion or desorption of individual molecules on metal surfaces [48].

2.2 Theoretical Description

The following section describes the physics behind the tunneling process and thus the STM. The very basic concept of electron tunneling will be presented as well as the most basic description for the application in the STM. A comprehensive theoretical description of the processes in an STM is extremely difficult due to the number of unknown factors contributing to the non-equilibrium conditions and the breaking of symmetry in the tunnel junction. For a closer discussion of the topic the reader is referred to the

abundant wealth of literature about STM-theory, for example [24, 25, 49–51].

In order to describe the tunneling of electrons one has to make a clear distinction between elastic and inelastic tunneling processes. In the first case the energy of the electron is conserved and thus equal before and after tunneling, in the latter case the electron gains or loses energy due to excitations in the gap such as plasmonic or phononic excitations. The following basic considerations are valid for the case of elastic electron tunneling.
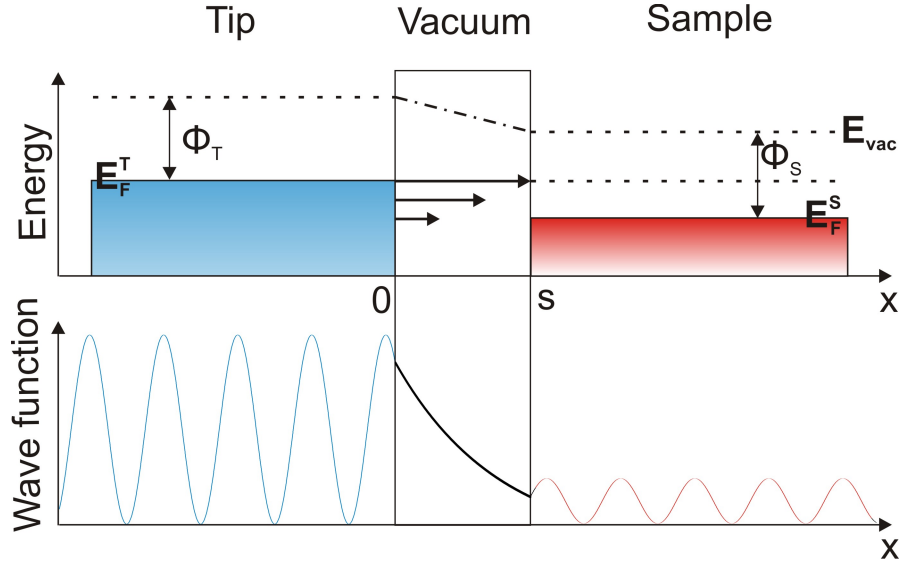
Figure 2.2: Schematic sketch of the tunneling junction and the wave function in the idealized case of one electron tunneling through a one dimensional potential barrier with the barrier width s.

Figure 2.2 schematically shows the idealized situation of one electron with the energy E and the mass m tunneling through a rectangular, one dimensional potential barrier. Assuming a height $V_0 > E$ and a width s, the Schrödinger equation writes as:

$$-[\frac{\hbar^2}{2m}\frac{\partial^2}{\partial x^2} + V(x)]\psi(x) = E\psi(x) \tag{2.2}$$

where V(x) is the potential barrier the electron is tunneling through, ψ is the wave function of the electron and $\hbar$ is Planck's constant.

The potential is:

$$V(x) = 0 \quad \text{for } x \notin [0, s] \tag{2.3}$$
$$V(x) = V_0 \quad \text{for } x \in [0, s] \tag{2.4}$$

In order to solve 2.2, the wave functions ψ writes as:

$$\psi(x) = e^{\pm iKx} \quad \text{for } x \notin [0, s] \tag{2.5}$$
$$\psi(x) = e^{\pm \kappa x} \quad \text{for } x \in [0, s] \tag{2.6}$$

with

$$K = \sqrt{\frac{2mE}{\hbar^2}} \tag{2.7}$$

and

$$\kappa = \sqrt{\frac{2m(V_0 - E)}{\hbar^2}} \tag{2.8}$$

One part of the wave function is reflected at the potential barrier and another part is transmitted. In order to ensure that the wave function is continuously differentiable everywhere one has to match the solutions of the Schrödinger equation and their derivatives at the points x=0 and x=s. This yields the barrier transmission coefficient T, which is the transmitted current density divided by the incident current density [49]:

$$T = \frac{1}{1 + \frac{(K^2 + \kappa^2)^2 \sinh^2(\kappa s)}{4K^2 \kappa^2}} \tag{2.9}$$

This exact expression for T may be simplified for the limit of a large barrier ($\kappa s \gg 1$)

$$T \approx \frac{16K^2\kappa^2}{(K^2 + \kappa^2)^2} e^{-2\kappa s} \tag{2.10}$$

The largest contribution to T stems from the term $e^{(-2\kappa s)}$. This strong dependence of the transmission coefficient on the barrier width and the square root of an effective barrier height $(V_0 - E)^{1/2}$ is a typical feature for a tunneling contact regardless of the actual shape of the barrier. Changing the barrier width by 1 Å leads to a change in the exponential factor in the barrier transmission by one order of magnitude. This very strong dependency on the tunneling barrier width has been exploited for the high spa-

tial resolution of the STM.

For the case of a metal-insulator-metal tunnel junction the time dependent Bardeen model may be applied [52]. The tunneling process through a three-dimensional barrier is treated as a time dependent perturbation. Applying Fermi's Golden Rule the transition probability from an unperturbed initial state μ before the tunneling barrier, described by a wave function ψ_μ, to an unperturbed final state ν after the barrier described by a wave function ψ_ν, may be calculated. This transition probability is given by the tunneling matrix element $M_{\mu\nu}$:

$$M_{\mu\nu} \quad = \quad -\frac{2m}{\hbar^2}\int_S dS(\psi_\mu^*\overline{\nabla}\psi_\nu - \psi_\nu\overline{\nabla})\psi_\mu^* \tag{2.11}$$

The integration is done over an arbitrary surface area between the tip and the sample through which the whole tunneling current flows. The transmission rate is given by the square of the matrix element $\left|M_{\mu\nu}\right|^2$.

In order to calculate reasonable values for the matrix element one needs good knowledge about the wave functions of the tip and the sample. In general, the structure and therefore the wave functions of the tip-apex are not known. This poses a major problem in simulating STM-images. Therefore Tersoff and Hamann extended the theory of tunneling by modeling the tip as a locally spherical potential well with s-character [50, 51]. This assumption allowed them to calculate actual tunneling matrix elements. Furthermore, the tunneling current is found to be proportional to the LDOS near the Fermi-level for the limit of small tunneling biases.

These assumptions lead to a simplified picture where the tunneling current is only dependent on the tunneling bias and the sample-LDOS at the center of the assumed tip:

$$I_T \propto eV\rho_s(r_0, E_F) \tag{2.12}$$

Where I_T is the tunneling current, V the tunneling bias and ρ_s the sample LDOS.

The main restriction of this model is the limitation to tip wave functions with s-character and thus an angular momentum $l = 0$. Despite the wide application of the Tersoff and Hamann model it fails to correctly describe the high corrugations observed for some metal surfaces [25]. Chen improved the model by allowing localized tip orbitals oriented towards the surface such a the tungsten $3d_z^2$ [53]. With this method a suitable orbital is chosen for the tip to correctly reproduce the experimentally observed resolution.

2.3 STM on Thin Insulating Films

As described in the previous sections the formation of an STM topographic image depends on various factors such as the topography, the local density of states up to the tunneling bias and the tip-sample geometry. This holds true already for the simplest possible system e.g. a tunneling junction between a metallic tip and a clean metal surface. The situation is more complicated for the case of a semiconducting or even insulating surface. In general, only conductive samples that do not charge up are suitable for investigation with the STM. For bulk oxide materials this is only the case at sufficiently high temperatures [54, 55] or with a sufficiently high defect-concentration [56].

Another possibility to investigate large band-gap oxide materials with the STM is the preparation of thin films supported on metal substrates [57, 58]. In this case the STM measurements are possible as long as the electrons overcome the oxide barrier sufficiently fast and flow to the metal substrate. This only holds for films with limited thickness. Both systems that have been investigated in this thesis fall into this category.

The thickness dependent electronic properties of thin insulating films have been studied to some detail for the case of NaCl on Al(111) and Al(100) [59], MgO on Ag(111) [60], or Al_2O_3 on NiAl [61, 62]. It is found that thin oxide films with a thickness of a few monolayers already exhibit the bulk band-gap value. Yet those films can still be investigated with the STM and even atomic resolution is readily obtained in many cases.
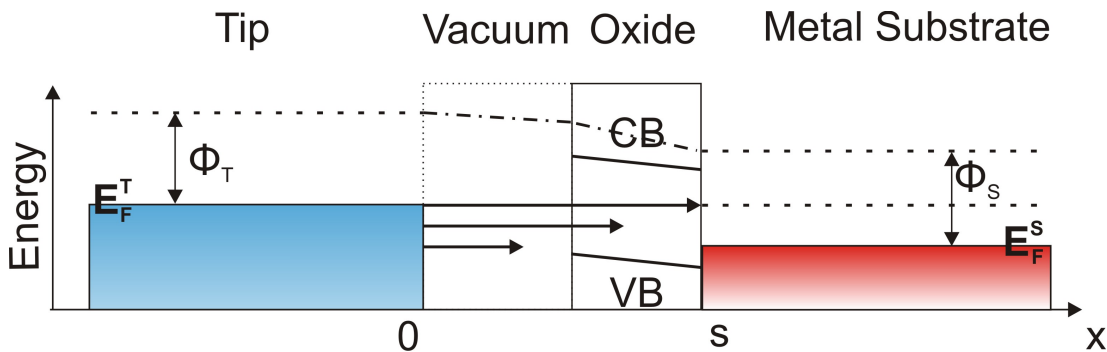
Figure 2.3: Schematic sketch of the tunneling junction with the oxide layer on top of the metal substrate for the idealized case of one electron tunneling through a one dimensional potential barrier with the barrier width s consisting of the vacuum and the oxide film. In this case the tunneling bias is not sufficient to reach empty states in the oxide conduction band. The electric field leads to a bending of the oxide conduction- and valence band.

Even though the STM has been used to explore such metal-oxide systems with great success a detailed theoretical description of the tunneling process itself is still missing. The tunneling junction for the case of an oxide film on top of a metal support consists of the two metal electrodes, the tip and the substrate and the two tunneling barriers,

the vacuum gap and the oxide film. This situation is visualized in figure 2.3. The oxide displays a band gap between the occupied valence band and the empty conduction band. Therefore two different tunneling modes must be distinguished:

1. The tunneling bias is chosen inside the band gap of the oxide. In this case the oxide states cannot contribute to the tunneling process and the STM is sensitive only to the states at the interface of the metal substrate. It is demonstrated in chapter 5 that this simple assumption does not always hold true, especially if there are localized states available in the oxide band gap. In many cases atomic resolution of the oxide film has been obtained at tunneling voltages within the oxide band gap (see [5] and references therein) being another hint that the tunneling matrix elements are influenced by the presence of the oxide film even at low bias.

2. The tunneling bias is chosen to be outside the oxide band gap. In this case states of the oxide layer directly contribute to the tunneling process. The apparent height of the film is then in the range of the real film thickness [63]. Due to the large tip sample distances at those tunneling conditions no atomic resolution is obtained in most cases. One has to be aware of the fact that for the case of thicker oxide films tunneling becomes impossible even at voltages for which the oxide bands are reached because electron transport into the metal is inhibited and the oxide charges up.

Being aware of these assumptions thin oxide films are systems very well suited for investigations with the STM even though especially STS results cannot always be interpreted in a straight forward way because of the many competing influences to the final tunneling signal.

3 Experimental Setup

The experiments have been performed in a home-built ultra-high-vacuum (UHV) low-temperature scanning-tunneling-microscope. The experimental setup consists of two chambers, a preparation chamber and the STM chamber. The two chambers are separated by a gate valve. The STM is used with a commercial control electronics (SPM 100 by RHK Technology). Recorded STM images are treated using the WSxM software [64].

3.1 The UHV Preparation Chamber

The UHV preparation chamber is equipped with standard sample preparation and analysis facilities, including Low Energy Electron Diffraction (LEED), Auger Electron Spectroscopy (AES), Ion Sputtering, Quadropol Mass Spectrometry (QMS) and a heating stage. Up to three samples and three tips can be stored in the preparation chamber. This allows a quick and convenient switching between samples and tips without breaking the vacuum. The chamber is pumped by a turbo-molecular pump and an ion-pump. The base pressure is maintained below 5×10^{-10} mbar and measured with a Leybold Heraeus IM220 Ionivac ion gauge. A photography of the setup is shown in figure 3.1.

Samples can be heated up to 2500 K with electron bombardment in the heating stage that is shown with a glowing sample in figure 3.2. Electrons emitted from the filament are hereby accelerated onto the backside of the sample with up to 2000 V. Emission currents of up to $\approx$100 mA may be reached. Temperatures are measured with a pyrometer (Metis MI16 by Sensotherm GmbH) that is connected to a computer in order to record temperature curves.

For the preparation of oxide-films the chamber contains a leak valve that is connected to a 12 bar oxygen bottle in order to create high partial oxygen pressures and two electron beam evaporators that allow for a total of five different evaporants. The thickness of deposited films is controlled via evaporation flux and exposure time.

A manipulator with four degrees of freedom is used to transfer the samples and tips between the different positions in the preparation chamber and the STM. The manipulator can be cooled with liquid nitrogen, bringing the sample down to approximately 100 K or heated using resistive heating up to approximately 550 K. The temperatures are measured with a Chromel/Alumel thermocouple spot welded to the end of the manipulator.

The preparation chamber is also equipped with a load-lock in order to transfer samples and tips into and out of the vacuum without opening the chamber. The load-lock is pumped by a separate turbo-pump and reaches high-vacuum conditions with a pressure of around 1×10^{-7} mbar after two hours of pumping.
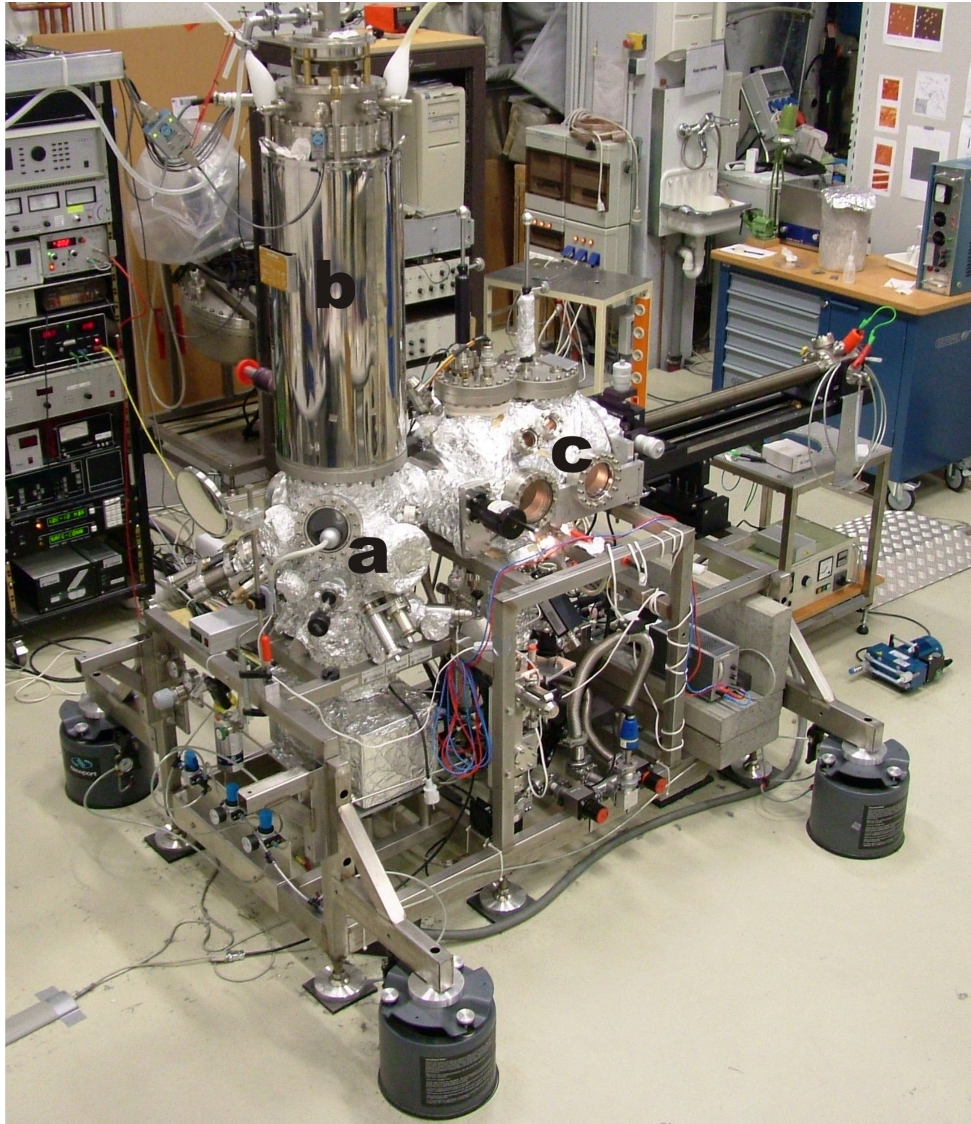
Figure 3.1: Photography of the UHV-chamber with the STM-chamber (a), the cryostat (b) and the preparation-chamber (c).
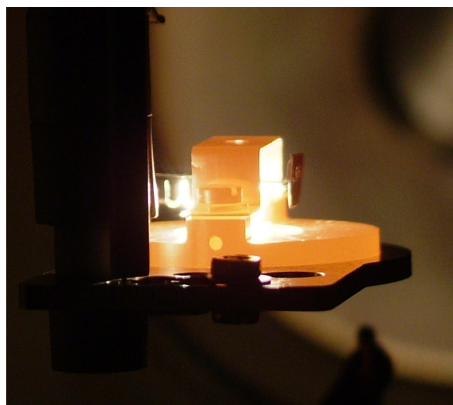
Figure 3.2: Glowing sample holder in the heating stage. The W-filament slides on top of the backside of the sample. Voltages of up to 2 kV may be applied to the sample to accelerate the electrons emitted from the filament.

3.2 The STM Chamber

The STM chamber contains the STM and the cooling shields in order to guarantee stable temperatures during operation at around 7 K.

The scan head has been realized as a Besocke type beetle STM [65] and is shown in figure 3.3 and schematically in 3.4. The sample is sitting in a metal sampleholder with a triple-helix structure at the bottom shown in figure 3.4. This triple-helix structure can be positioned on three piezo tubes with sapphire heads that enable the approach and rough positioning of the sample. The tip is mounted on an fourth piezo in the middle of the three outer piezos. This is the scan piezo. A detailed description of the beetle type STM can be found elsewhere [66] and a detailed description of this setup can be found in the PhD-thesis of Stefan Ulrich [67].

The STM-chamber also contains two metal evaporators that can be used to evaporate metal atoms in situ onto the sample at low temperatures. One of the evaporators can be separated by a valve from the STM-chamber allowing a change of evaporant without venting the chamber.

The temperature of the STM is measured with the characteristic curve of a diode (DT 470 BO by Lake Shore) connected to the baseplate of the STM. The STM is operated at low temperatures around 7 K. In order to achieve this low temperature and simultaneously allow for a good optical access to the tunnel junction the STM head is surrounded by movable cryo-shields. A top-mount bath cryostat (by CryoVac GmbH) contains a dewar for liquid Helium (8.5 l) that is surrounded by a second dewar for liquid nitrogen (19 l). In order to lower the liquid helium consumption the helium exhaust line is equipped with a recuperator which channels the cold gas to cool two baffles in form of aluminum disks. The upper one reaches a temperature of 70 K. The lower one goes down as low as 30-40 K. This setup allows for a very low liquid Helium consumption: filling the inner dewar with 8.5 l of liquid Helium can keep the STM at low tempera-
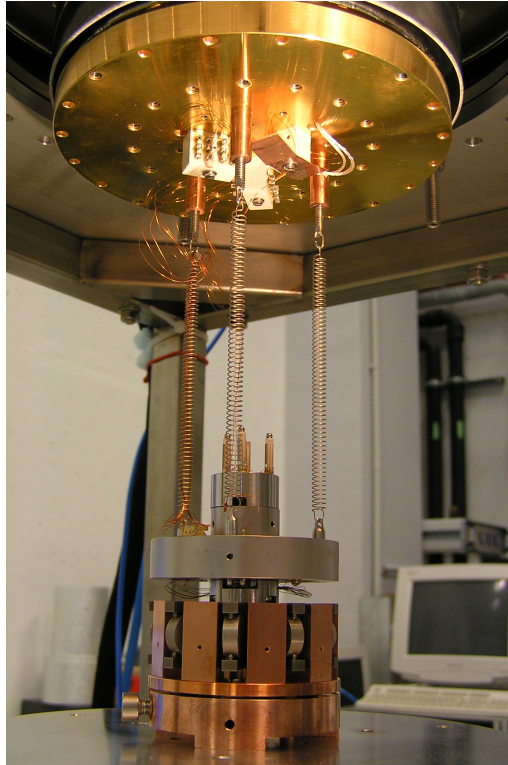
Figure 3.3: Photo of the scan head hanging in springs and damped by an Eddy Current Unit, photo taken by Stefan Ulrich.

ture for up to 7 days without refilling. The liquid nitrogen needs to be refilled every 36 hours but this can be done with an automatic timer, so it does not require the presence of the experimenter.

The whole UHV-setup is damped against external vibrations with six active damping elements (AVI 350S by JRS Scientific Instruments). These elements actively damp vibrations with piezo-elements in a frequency window between 0.8 Hz to 200 Hz. Higher frequencies are damped passively with a suspension system. Additionally the STM stage itself is damped against the cryo-shields with an eddy current damping system.

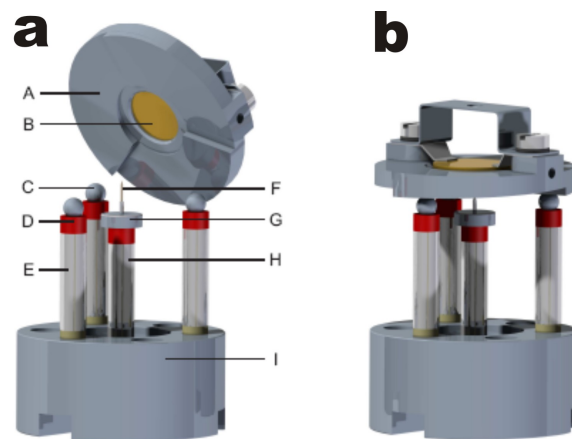A more detailed description of this setup is presented in the PhD-thesis of Stefan Ulrich [67].

Figure 3.4: Drawing of the scan head setup. (a) A: ramp with different sectors, inclination $1mm/120°$, B: sample, C: support ball, D: sapphire, E: support-piezo, F: tip, G: tip-holder, H: scan-piezo, I: base, (b) Scan head with sample holder sitting in scan position; taken from [67].

17

4 Tailoring the Chemical and Physical Properties of a Thin Silica-Film on Mo(112)

Silicon dioxide (silica) is a material of great interest not only to the scientific community. It is being used in modern metal oxide semiconductor field-effect transistors (MOS-FET) and thus an important part of integrated circuit technology and the digital world. Moreover, Silica is employed as catalyst support, in optical fibers and in solar cells. Therefore its properties are of great interest and extensively studied.

In order to study physical and chemical properties of such oxide systems with the wide range of surface science techniques that require a conductive sample, such as STM, PES, LEED or Auger, thin films have been grown on metal substrates. These thin films circumvent charging problems but still mimic certain properties of the bulk materials while also displaying new, interesting properties of their own right [1–5].

Tailoring the structural and chemical properties of solid materials has been of great interest in surface science for a long time [2, 68]. In order to functionalize a surface several aspects are of importance. One needs to controll the density and spatial arrangement of binding sites, the chemical selectivity of the adsorption behavior and the internal structure of the ad-material. Systems that display these properties have a wide range of applications, e.g. as catalysts in stereo-selective reactions, chemical sensors, and template surfaces for self organization processes. Mechanisms that have been implemented towards tailored surfaces include lithographic techniques [69], molecular and colloidal self-organization techniques [70] and imprinting methods [71]. However, these methods are not, or only in very few and limited cases such as [72], suitable for tailoring at the atomic scale.

In this chapter a case study for a crystalline, ultra-thin oxide film is presented using results from STM and STS experiments. A possibility to tune the physical and chemical properties of this system by inserting alkali-atoms into the interface between the oxide film and the metal support is discussed, opening a way of tailoring surface properties at the atomic scale. Moreover, the capabilities of this ultra-thin oxide film to store single magnetic units in a stable and chemically inert environment have been explored, showing a possibility to create an array of magnetic units consisting of single atoms.

4.1 Preparation and Structure of a Mono-Layer Silica Film on a Mo(112) Single Crystal

The Mo(112) single-crystal is prepared via several cycles of sputtering with argon ions and annealing. Hereby the argon ions are accelerated to an energy of 1 keV. Each sput-

ter cycle is followed by an annealing cycle where the crystal is kept at 1600 K for 10 minutes. After every second annealing cycle the crystal is exposed to 1000 L molecular oxygen at a temperature of around 700 K before being sputtered again. This oxygen treatment is aimed at the removal of carbon contaminations arising from carbon segregation from the bulk to the surface upon the annealing. This treatment gives rise to the well known, atomically ordered clean Mo(112) surface consisting of a [-1-11] oriented row and furrow structure [73].
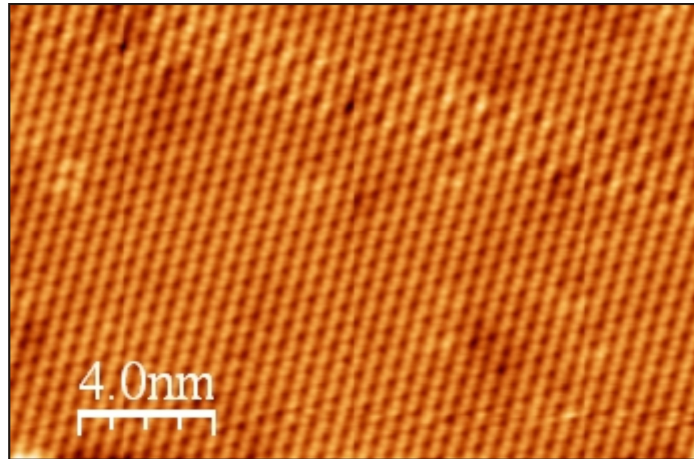

Figure 4.1: STM image of the bare, crystalline silica film. Two anti-phase domain boundaries that constitute the line defects of this film are visible in the upper third of the image. Tunneling conditions were $U_B = 0.5$ V and $I_T = 0.4$ nA

Before film preparation the clean surface is preoxidized with 50 L O_2. The oxidized surface is subsequently exposed to a mono layer of silicon evaporated from a silicon rod in an electron-beam evaporator (Oxford Scientific), in an ambiance of 1×10^{-7} mbar O_2 at a sample temperature of 550 K. After evaporation the sample is annealed to 1200 K in UHV. This preparation gives rise to an ordered, crystalline, mono layer silica film [74] which can be nicely imaged with the STM as shown in figure 4.1.

The detailed structure of this film has been investigated with various experimental and theoretical methods yet different structural models had been proposed. These models explained the monolayer silica film either as an arrangement of isolated SiO_4 units on the Mo(112) surface [75] or as a two-dimensional Si-O-Si network [74, 76, 77]. Those models could not be distinguished with STM, LEED or AES experiments alone and only combined efforts by theory and various experimental techniques [78, 79] could finally determine the discussion in favor of the two-dimensional network model. The growth behavior and morphological properties of this film have been described in detail elsewhere [80, 81], therefore only a brief overview over the most important aspects is given here. Further experimental details regarding the properties of this film are reported here [74, 76, 77, 82].

The film consists of a two-dimensional network of corner sharing SiO_4 tetrahedra.

One oxygen atom of each tetrahedra is bond to a molybdenum atom of the substrate while the remaining three form Si-O-Si bonds with the neighboring tetrahedra. The in plane Si-O-Si units form rings consisting of six members with a diameter of 5 Å. The hole in the middle of the ring reaches all the way down to the surface of the molybdenum substrate. Formally the silicon and oxygen surface atoms are in a +4 and -2 oxidation state respectively. This configuration renders the film chemically inert to molecular adsorption processes [83]. The most frequently observed structural defects of this oxide film are anti-phase domain boundaries that are formed to release strain in the film induced by coalescence of misfit oxide domains. These boundary lines consist of eight membered Si-O rings with a larger opening in the middle compared to the regularly observed six membered rings. This is visible in the upper part of figure 4.1.

4.2 Adsorption of Metal Atoms on Silica: the Realization of an Atomic Sieve

Previous experiments have revealed the special adsorption characteristics of the silica film [84–87]. Due to its porous structure strong adsorption sites at the metal-oxide interface become available whereas the inert oxide surface itself interacts only weakly with adsorbates. The pore structure resembles that of bulk-zeolites and thus constitutes a two dimensional realization of a nanoporous zeolite material [88]. Due to the small size of the pores, 5 Å, the silica film acts as an atomic sieve. Some atoms can penetrate the pores and bind to the interface whereas other atoms cannot enter the pores and subsequently bind only on defect sites. This has been shown for several cases where the atoms either penetrate the pores like palladium [84] and silver [85] or are unable to enter, such as gold [85, 86].

STM images taken after depositing palladium atoms onto the freshly prepared silica film at 10 K reveal structures that seem to be incompatible with atomic adsorption on top of the oxide film. This is shown in figure 4.2. Instead of round protrusions as observed for the adsorption of metal atoms on other oxide surfaces [89] distinct hexagonal star-shaped features appear in low bias STM images as can be seen in figure 4.2 a. The fact that the star-shaped features resemble parts of the bare silica film gives rise to the interpretation that not the metal adsorbates themselves are imaged but rather the modified electronic structure of the oxide film. This interpretation is supported by the fact that the features show a strong bias-dependency as shown in figure 4.2 c. At biases well below 2 V the bright, star-like contrast stems from additional LDOS due to the hybridization of the palladium *5s* orbital with the *2p* states of the oxygen atoms. Additional contrast from the palladium *5s* becomes available only at higher biases close to 2 V. The features in STM images then transform into round protrusions centered in the middle of a silica pore. Density functional theory (DFT) calculations also support the finding that the palladium atoms penetrate the silica pores. This is illustrated in figure 4.2 d and [84].

A similar behavior was observed for silver adsorption on the silica film [85]. As shown in figure 4.3 a, STM images taken after exposing the silica film to silver atoms
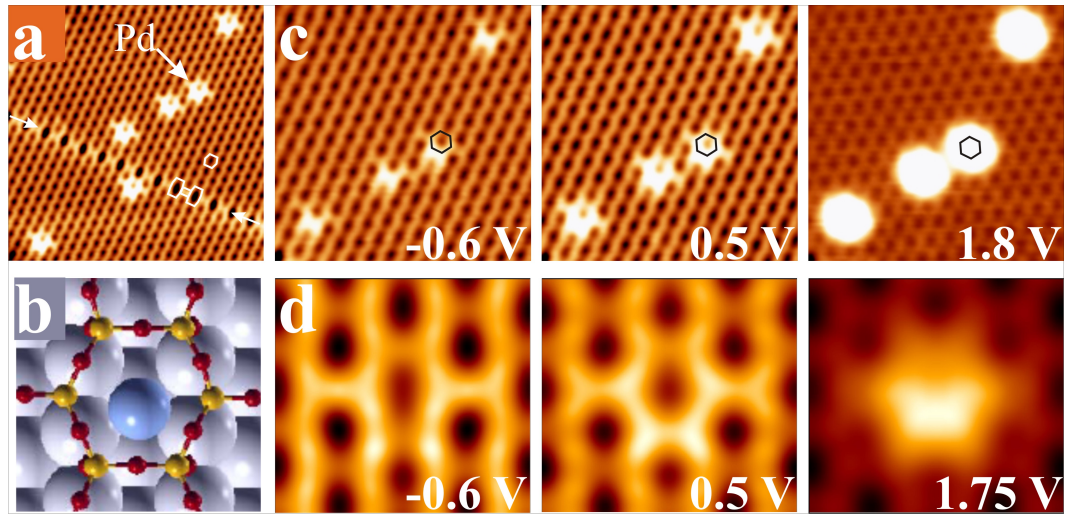
Figure 4.2: (a) STM image (0.5 V, 13 x 13 nm^2) of 0.1 ML Pd on SiO$_2$ on Mo(112). (b) Structure model of the Pd adsorption site (small black spheres: O, small gray spheres: Si, large gray sphere: Pd). Bias dependence of the topographic contrast of Pd atoms in (c) experimental (5 x 5 nm^2) and (d) simulated STM images (1.8 x 1.6 nm^2, 6 x 4 supercell). Adapted from [84].
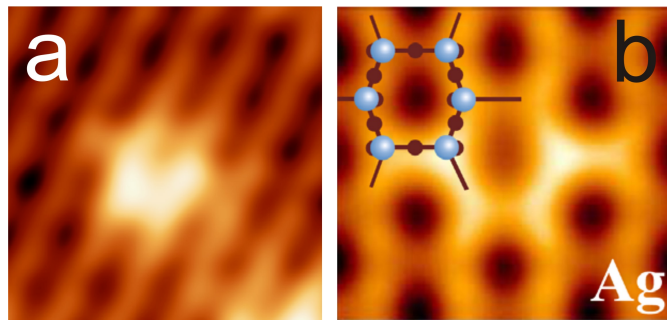
Figure 4.3: (a) STM image (0.5 V, 13 x 13 nm^2) of an Ag-atom incorporated into the SiO$_2$ thin film grown on Mo(112). (b) Simulated STM image of an Ag-atom incorporated into the SiO$_2$ thin film. Adapted from [85].

at a temperature of 20 K show somewhat similar star-like features as for palladium. Again the adsorption of silver atoms at the metal-oxide interface results in enhanced contrast of the surrounding O-Si-O network. The bias dependency is different than the one observed for palladium atoms [85].

A completely different behavior is found for the adsorption of gold onto the silica film [84]. Unlike for the case of palladium and silver, no distinct contrast enhancement is found upon gold adsorption on the defect free film. Instead protrusions of various sizes appear along the line defects after the deposition of gold atoms at 20 K as shown in figure 4.4. The smallest features found on the film after gold deposition affect only a single octagonal pore of a line defect. This feature shows a similar bias dependency as the palladium atoms found in the regular pores of the silica film which can be seen in figure 4.4 c. With increasing gold coverage bigger features start to appear along the line defects while the patches of stoichiometric silica remain free of gold induced features. Evidently gold is able to penetrate only the holes at the line defects where the pore diameter is larger.
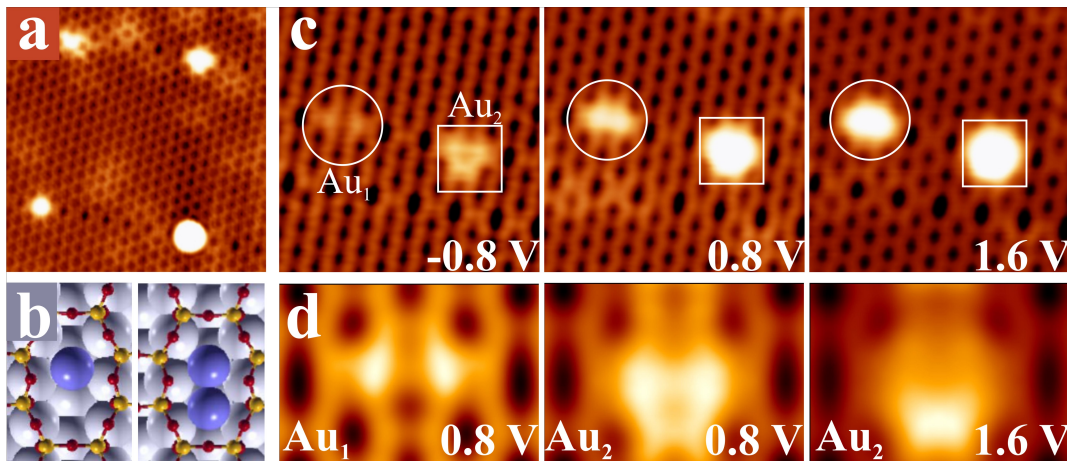

Figure 4.4: (a) STM image (0.5 V, 13 x 13 nm^2) of gold on silica/Mo(112). (b) Structure model of an Au monomer and dimer in an octagonal -Si-O- ring located along the silica domain boundaries (O: small, red; Si: small, yellow and Mo: large, blue spheres). Bias dependence of the topographic contrast for different Au aggregates in (c) experimental (4.5 x 4.5 nm^2) and (d) simulated STM images (2.1 x 1.4 nm^2). Adapted from [84].

Due to its selective adsorption behavior the silica film grown on Mo(112) acts as an atomic sieve: smaller atoms such as palladium or silver can penetrate the nano-pores and bind strongly to the metal-oxide interface whereas larger atoms such as gold can not enter the regular pores. Hereby the van der Waals radius of an atom does not play the decisive role but rather the spatial diffusivity of the top most filled atomic orbital. Filled atomic orbitals with a large spatial diffusivity such as an *s*-orbital hamper the

pore penetration whereas more confined orbitals such as *p*-orbitals do not hinder the pore penetration. Atoms that cannot enter the oxide pores therefore diffuse on the surface even at low temperatures until they eventually bind to line defects in the silica film.

The incorporation of metal atoms into the metal-oxide interface dramatically changes the adsorption properties of the system. It has been found that palladium as well as silver atoms can act as surface-anchors enabling the adsorption of atoms on top of the otherwise inert silica film [86]. Therefore the insertion of metal atoms to the interface is a first step to locally modify the adsorption characteristics of the silica/Mo(112) system [86].

4.3 Incorporating Lithium Atoms into the Silica Thin Film

The work for this thesis starts from the idea to further explore the opportunities of tailoring the chemical properties of the thin silica film. In order to modify the global properties of the silica/Mo(112) system lithium has been chosen as a promising candidate for incorporation [90].

Due to their low ionization potential alkali metals have different chemical properties than all other chemical elements. This special characteristic is due to the weak bonding of the unpaired *s*-electron that can easily be removed from the valence shell. Corresponding to this property alkalies have the lowest Pauling electronegativity in the periodic table.

Therefore, alkali metals are of great technological importance. Alkalies are used as promoters in catalytic reactions where they provide weakly bound electrons for reduction processes. They can also be found in low work function materials that display a high electron emissivity and of course in modern lithium-ion batteries with high energy density [91–93].

Due to this low ionization potential charge transfer processes play a crucial role in the adsorption of alkali atoms. While alkali atoms adsorbed on noble metal surfaces give away almost an entire electron charge, the interaction between alkali atoms and transition metal surfaces is more covalent [94, 95]. In the case of the tungsten or molybdenum surface the dominant part of the interaction stems from the hybridization between the valence *s*-state of the alkali atom and the *d*-band of the metal. This leads to a strong polarization of the alkali *s*-electron towards the metal support [96, 97]. The charged or polarized alkali atoms on the metal surface lead in any case to a positive surface dipole that induces a significant reduction of the work function. Increasing the amount of alkali atoms per surface area first enhances the effect of work function reduction up to a critical amount when the repulsive interaction between the surface dipoles inhibits the electron transfer from the alkali atoms to the metal support. The alkali adlayer gradually loses its polarity and the alkalies become metallic which in turn leads to a work function increase towards the bulk value of the respective alkali metal [94, 95, 98, 99]. The ionization of alkali metal atoms often causes a self assembly behavior in the adsorp-

tion due to the repulsion between the equally charged adatoms [100–102]. This simple picture of alkali adsorption on metals, first elaborated by Lamgmuir and Gurney [103–105], already explains most features of the general adsorption behavior of alkali atoms on metal surfaces. However, as described in this thesis not all observations follow those basic assumptions.

One of the main technological challenges in the use of alkali metals is the protection of the very reactive alkalies from unwanted interaction with the surrounding atmosphere, that would lead to a quick degeneration of the desired properties. Therefore alkali atoms are usually embedded in a metal or oxide matrix that prevents reaction with the environment but also hampers the desired effects, i.e. the work function reduction. In a theoretical study Pacchioni and coworkers suggested an elegant way to combine both desired properties, the protection and the work function lowering [90]. In their work Pacchioni *et al.* explore the possibility to place single alkali atoms in the pores of the mono layer, crystalline silica film. While for the larger alkali atoms potassium and sodium adsorption sites on top of the film are predicted, lithium being the smallest alkali atom was found to preferentially bind at the metal-oxide interface. The position at the interface between the metal substrate and the oxide film protects the lithium atoms from reacting with the environment. The lithium is expected to give away its complete *2s*-electron to the molybdenum conduction band. The resulting lithium ion at the metal surface induces a sufficient dipole for the desired reduction of the work function. Another advantage of this system is the accessibility of the adsorption sites in the oxide pores even after the preparation of the oxide film [90].

Within the framework of this thesis the possibility to place lithium atoms in the pores of a mono layer crystalline silica film has been explored experimentally with the means of STM and STS. Furthermore, additional details on the interaction of the lithium atoms with the metal support, the influence of the oxide film and the resulting change in the work function have been studied. In addition the distinct spatial arrangement of the lithium atoms at the metal-oxide interface is discussed and explained in terms of the screening response of the metal surface below.

4.3.1 Single Lithium Adsorbates

The lithium atoms are deposited from a commercial dispenser made by SAES Getters S.p.A. onto the bare silica film at a temperature of around 77 K.

Already after depositing less than 0.05 lithium atoms per silica pore distinct features start to appear in STM images as can be seen in Figure 4.5. Two different configurations can be distinguished, ringlike protrusions that coincide with one Si-O hexagon, as shown in figure 4.5 a, and X-shaped protrusions that are oriented along the [110] direction of the molybdenum substrate as shown in figure 4.5 b. Starting from those elementary configurations also larger adstructures are assembled yielding especially high imaging contrast at the intersection points of two adjacent elements. For instance,
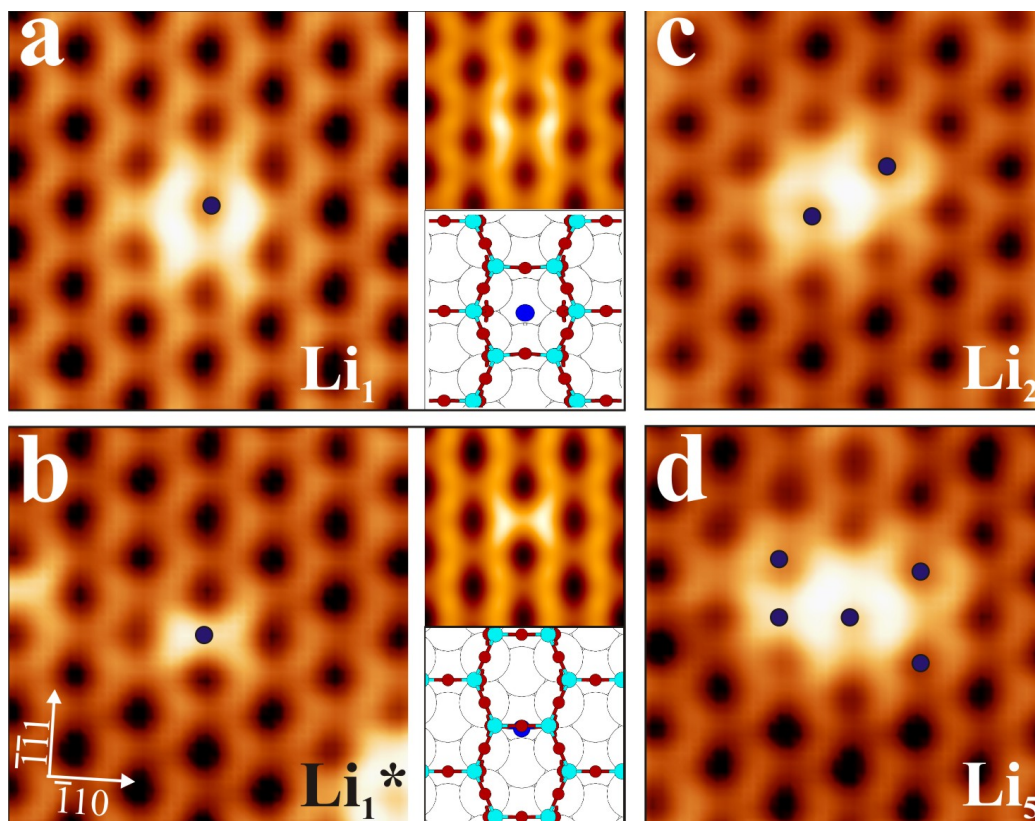
Figure 4.5: (a) and (b): Experimental (0.1 V, 3 x 3 nm^2) and simulated STM images and structure models for two different adsorption sites of single Li atoms bound at the interface between the oxide film and the Mo(112) support. In the model the oxygen atoms are red, the silicon atoms cyan and the Li atoms are depicted in blue. (c) and (d): Experimental STM images of larger Li aggregates (0.1 V, 3 x 3 nm^2) with Li atoms (position marked by blue dots) bound to neighboring interface sites.

the structure in figure 4.5 c is assigned to a lithium dimer and figure 4.5 d might be comprised of five lithium atoms bound to neighboring sites at the interface.

In all observed cases the enhanced topographic contrast in the STM images seems to stem not from the adatom itself but rather from distinct building blocks of the silica film. A similar behavior has been revealed before for palladium and silver atoms deposited onto the same system as described in section 4.2 and in [84, 85]. The contrast is triggered by a hybridization of the valence *s*-state of the adatom and the O *2p* orbitals of the surface oxygen atoms which locally increases the density of unoccupied states of the silica pore above the adsorbate feature. This is addressed in section 4.3.4 of this thesis. The absence of spherical protrusions and the observation of pores with enhanced contrast lead to the assumption that the lithium atoms penetrate the pores and bind to the interface rather than on top of the silica film. This observation is in agreement with the palladium and the silver results and confirms the theoretical predictions mentioned above [90].

The distinct appearance of the ring-like and the X-shaped features is only observed at small tunneling biases. At higher positive voltages they transform into round protrusions as can be observed in figure 4.6 a and b. The lithium features do not only change their shape but also display a larger apparent height at tunneling voltages above a certain threshold. The value of this threshold depends critically on the size of the lithium feature. While mono atomic lithium features become bright at around 2.75 V, this value shifts to about 2.25 V for larger aggregates containing more than three lithium atoms. This behavior is plotted in figure 4.6 b. These observations may be explained by the availability of new conductance channels at higher energies that are responsible for the new contrast in the STM images. DFT calculations performed by Pacchioni *et al.* support this assumption [42]. The calculated LDOS of the silica in the vicinity of a sub-surface lithium atom reveals an availability of extra states at lower energies compared to the bare silica film as shown in image 4.6 c. The experimentally observed threshold energy for larger lithium features corresponds to the calculated energy position of empty states, even though DFT is known to underestimate the energy position of states in materials with a band gap.

The experimentally observed adsorption behavior is in good agreement with DFT calculations performed for this system [42]. Therefore a comprehensive picture of lithium adsorption on the silica/Mo(112) system emerges. Single lithium atoms penetrate the pores of the silica film with a low activation barrier of 0.3 eV and bind at two different sites at the interface between the oxide film and the metal support. For the first adsorption site directly below a silica ring (Li$_1$, see figure 4.5 a) the binding strength is calculated to be 2.43 eV. In this configuration the lithium atom gives away almost its complete *2s* electron to the molybdenum support. The Bader analysis reveals a charge of +0.88 $|e|$ located at the lithium ion. The Li *2s* orbital hybridizes with the unoccupied Si *3s*-O *2p* hybrid states of the oxide film above the adsorption site providing additional empty states at the oxide surface. Those additional states are probed in
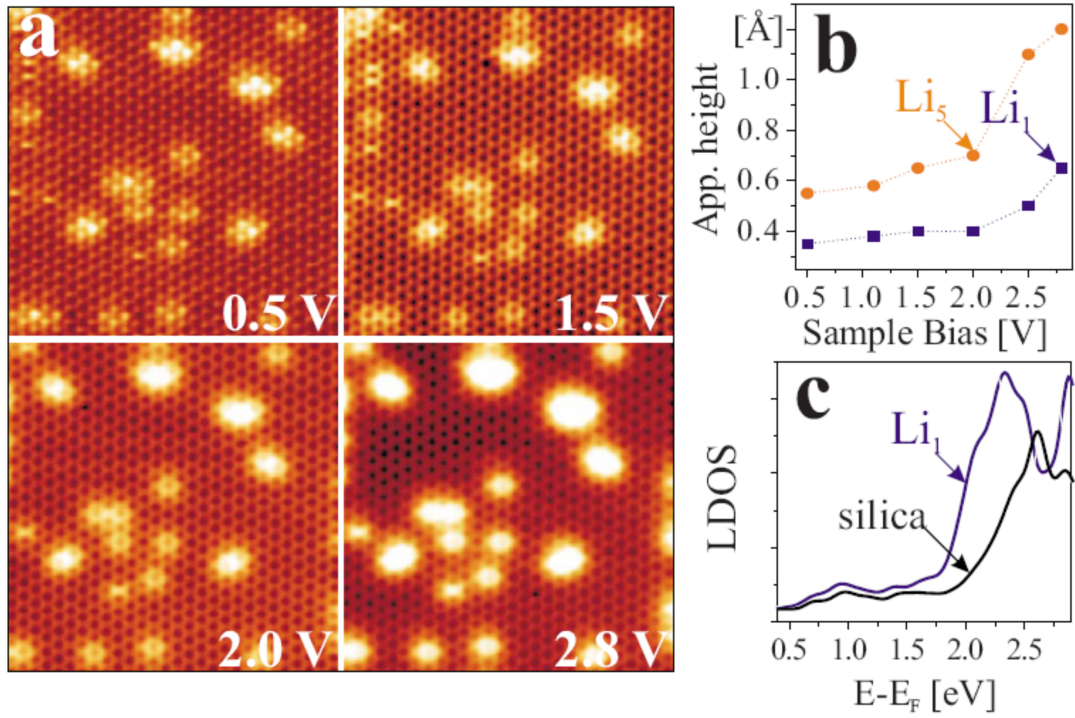
Figure 4.6: (a) Bias dependence of single Li atoms and small aggregates at the silica/Mo(112) interface (15 x 15 nm^2). (b) Evolution of the apparent height of Li features as function of tunneling voltage. (c) Calculated LDOS of the bare silica film and a mono atomic Li adsorbate. The increase in the Li LDOS at higher energy is reflected by the experimental height increase for higher tunneling bias. DFT Calculations were performed by Pacchioni and coworkers [42].

the low bias measurements and give rise to the ring-like contrast in the STM images observed in figure 4.5 a.

The second interfacial site (Li_1^*) that can be occupied by a lithium atom is a molybdenum hollow site below a [$\bar{1}$10]-oriented segment of a silica pore. The calculated binding energy for this adsorption site is 2.41 eV, almost equal to the binding strength at the other adsorption site. In this adsorption configuration the lithium hybridizes with empty states in the Si-O-Si unit above, giving rise to the X-shaped contrast in the STM images as observed in figure 4.5 b. Again the interaction with the molybdenum substrate is strong and according to a Bader analysis a charge transfer of +0.82 $|e|$ from the lithium to the molybdenum takes place. The reduced charge transfer and especially the shorter Li-Mo distance with respect to the ring-like adsorption site (1.25 Å versus 1.57 Å) reduces the induced surface dipole by 20% with respect to ring adsorption site. Therefore, also a lower effect on the work function is expected from lithium ions at this binding site. For the two cases described above no interaction between neighboring lithium ions is considered. The situation changes for higher coverages where additional aspects have to be taken into account. This is addressed in the next section.

4.3.2 Higher Lithium Coverages

As described in the previous section 4.3.1 the adsorption behavior for single lithium atoms largely follows the well established picture of alkali adsorption on metal surfaces [94, 103, 105]. Despite the presence of the oxide film the lithium becomes cationic and binds to highly-coordinated sites along the Mo(112) furrows. This picture changes however as larger amounts of lithium are dosed onto the silica film.

With increasing lithium coverage the distinct ring-like and X-shaped fingerprints of the single lithium atoms adsorbed at the interface can not be resolved anymore because neighboring features start to overlap in the STM images. However, areas with a high lithium concentration remain clearly distinguishable from areas with a low lithium concentration. The reason is the additional empty state density for tunneling above 2 V that leads to a larger apparent height in topographic STM images, which is shown in figure 4.7. At higher lithium coverages the density distribution of lithium atoms at the interface becomes more and more inhomogeneous. This is surprising because the simple picture of repelling ions with equal charge would lead to a maximization of the distance between the ions. Already at nominal coverages of about 0.2 lithium atoms per silica pore the lithium starts to assemble into groups of roughly six atoms adsorbed in neighboring pores, as visible in figure 4.7 a. A further increase of the lithium coverage leads to an amplification of this ordering behavior. Elongated lithium rich islands start to form at the silica/Mo(112) interface. These islands display a certain order with mean inter-island distances of about 30-50 Å and 15-20 Å in [$\bar{1}$10] and [$\bar{1}\bar{1}$1] direction respectively, as can be observed in figure 4.7 a and b. Above a critical coverage of about 0.4 lithium atoms per pore the lithium rich areas start to merge into long stripes along the [$\bar{1}\bar{1}$1] direction displaying a clearly visible long range order. The stripes are about 15 Å wide and up to 200 Å long, interrupted only by anti phase domain boundaries of the

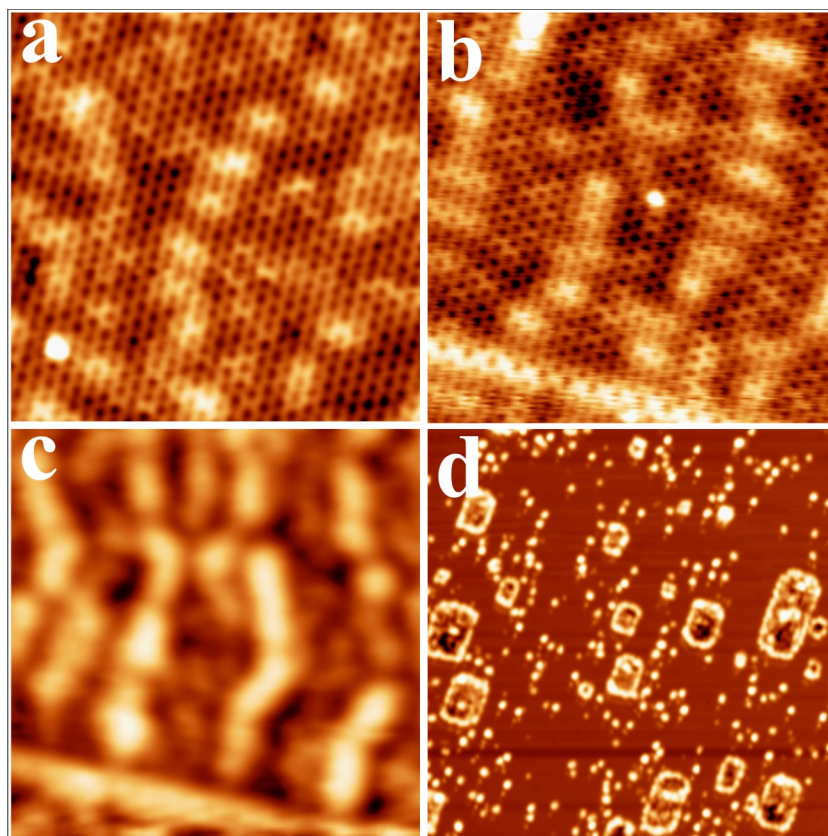Figure 4.7: STM images of silica films with increasing Li coverages. (a) 0.2 Li atoms per silica pore, 15 x 15 nm^2, 0.5V. (b) 0.3 Li atoms per silica pore, 15 x 15 nm^2, 0.5V. (c) 0.5 Li atoms per silica pore, 15 x 15 nm^2, 2.5V. (d) more that 1 Li atom per silica pore, 150 x 150 nm^2, 3.5V, after filling of all available adsorption sites at the interface large Li-adclusters start to form on the surface.

oxide film. This long range order is shown in figure 4.7 c and 4.8 a.
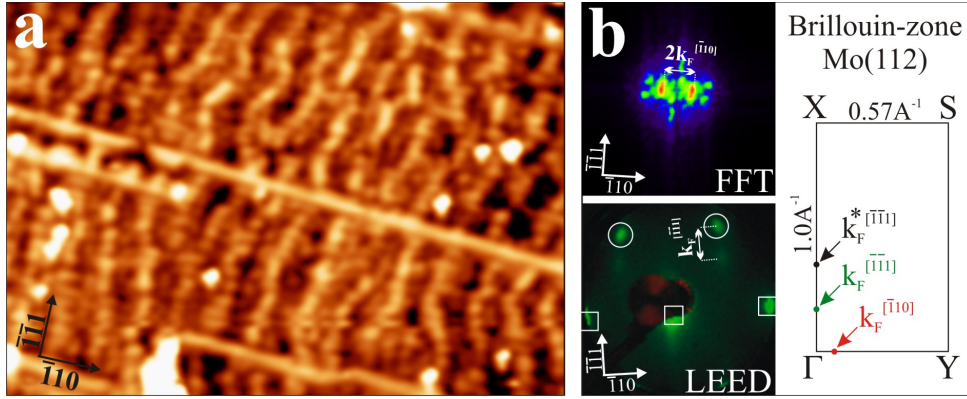

Figure 4.8: (a) Large scale STM image showing the ordered Li pattern on silica/Mo(112) (3.0 V, 65 x 45 nm^2). (b) Reciprocal space information deduced from a Fourier transformation of (a) and a LEED measurement performed at 30 eV electron energy. The fundamental silica and Mo LEED spots are marked by circles and squares, respectively. The faint spot below each silica reflex reflects the long-range order in the Li distribution along the Mo[$\bar{1}\bar{1}$1] direction. The [$\bar{1}$10] periodicity is not revealed due to the limited coherence length of the LEED system. The right inset depicts the Brillouin zone of Mo(112) with the k vectors of prominent surface resonances marked by dots.

The direction of the lithium rich stripes roughly follows the direction of the furrows in the Mo(112) surface even though a mismatch of up to $\pm$ 20° is observed. A characteristic distance between two lithium rich stripes separated by a lithium poor region of (44 $\pm$ 4) Å is observed. This long range ordering phenomenon in real space gives rise to distinct extra spots in Fourier-transformed images at a wave vector of $k_{\bar{1}10} = 2\pi/45$ Å^{-1} as shown in figure 4.8 b.

A further increase in the lithium coverage above 0.6 lithium atoms per silica pore triggers the formation of a second set of [$\bar{1}\bar{1}$0]-oriented lithium stripes which are located between the initial ones and appear with lower topographic contrast in the STM images. This leads to a doubling in the superstructure periodicity to (22$\pm$4) Å in real space, while in the Fourier transformed images a second reflex starts to appear as shown in figure 4.8 b.

Along the lithium stripes, only weak and less regular intensity modulations are observed in the STM. However, LEED measurements of the lithium-doped silica film reveal an extra spot next to the silica reflex that indicates an additional periodicity of (19$\pm$4) Å along the Mo [$\bar{1}\bar{1}$1] direction, which is also shown in figure 4.8 b. On the other hand the (44$\pm$4) Å periodicity along the [$\bar{1}$10] direction is not resolved in the diffraction pattern due to the limited coherence length of the employed LEED system.

The enhanced contrast of the lithium also appears at the line defects of the silica film

as visible in figure 4.7 b and c and figure 4.8 a. This indicates that the lithium atoms preferentially penetrate the larger pores of the anti phase domain boundaries (APDB). This is expected since the eight-membered rings of the APDB are associated with a smaller penetration barrier than the regular six-membered pores of the silica film and should be filled with lithium as well [84, 85]. For lithium coverages exceeding one atom per pore, nucleation of lithium adclusters is observed on the silica surface, as shown in figure 4.7 d. Apparently, all interfacial binding sites are saturated at this stage and atom penetration through the oxide film is not feasible any more. This also correlates with the finding that only one lithium atom can penetrate each pore.

4.3.3 Discussion of the Structural Aspects of Lithium Incorporation

The formation of long range lithium patterns at the silica/Mo(112) interface that has been found for this system deviates from the adsorption behavior observed on metal surfaces where the alkali ions usually adopt open configurations in order to minimize their Coulomb repulsion [94, 98, 99, 102]. Even on the bare Mo(112) surface without the oxide film, the development of (4x1) and (2x1) superstructures has been reported in LEED experiments after alkali deposition [98–100]. In contrast to those earlier findings, for the silica/Mo(112) system the lithium forms small assemblies at the metal-oxide interface. Already at relatively low exposure although the calculated Bader charge of at least $+0.8|e|$ clearly indicates the ionic character of the adsorbed lithium species. The difference to bare metal surfaces can be rationalized by the presence of the dielectric silica film on the molybdenum support, which facilitates the screening of the Li^+-Li^+ interaction. The screening efficiency becomes manifest in the weak coverage dependence of the lithium binding energy, as computed by DFT and shown in figure 4.9 a. An increase in the nominal coverage from zero to one Li^+ per silica pore reduces the adsorption strength by less than 3%. This indicates that even if all neighboring pores are already filled, there is no sizeable repulsion from the other positive charges. A steeper decline in the binding energy is observed in calculations only when a second lithium atom is forced into the pore. In this case the increasing Coulomb repulsion between the ions cannot be screened by the oxide any more and becomes dominant. This finding is in good agreement with the STM results, which indicate a maximum coverage of one lithium atom per silica pore at the chosen experimental conditions.

As incorporation of more lithium would be favorable from a thermodynamic point of view, the saturation coverage seems to be related to a kinetic hindrance, for instance the penetration barrier into the pores. The weak initial coverage dependence of the lithium binding energy enables the formation of lithium islands at the metal-oxide interface. This effect has been illustrated by computing the stability of three hypothetical lithium-silica structures with different inter atomic spacings as shown in figure 4.9 b.

In the calculations three different cases are considered: adsorption of lithium trimers in three adjacent pores, well separated lithium monomers with all adjacent pores being empty, and finally a lithium row structure. These configurations are shown in figure 4.9 b. The trimer configuration is calculated to be the energetically most favorable whereas the isolated lithium ions and the row pattern are higher in energy by 0.025 and 0.07 eV
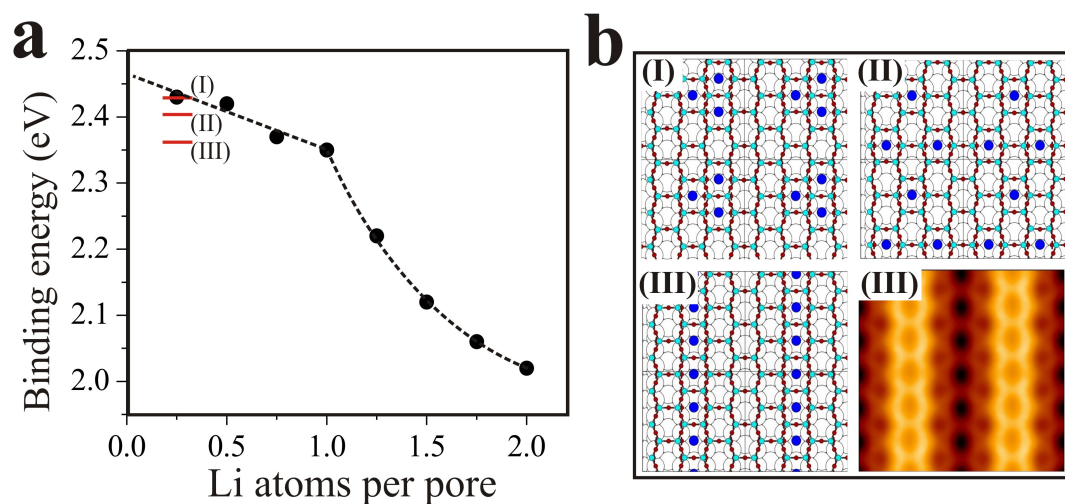
Figure 4.9: (a) Calculated coverage dependence of the Li binding energy at the silica/Mo interface. (b) Structure model for three configurations with identical Li coverage of θ=0.25. The corresponding Li binding energies are depicted in (a). A simulated STM image for configuration (III) is shown in the lower right panel (+2.0 V, 3.3 x 3.3 nm^2). The Li-rich areas are imaged with enhanced contrast although the geometric corrugation is negligible, corroborating the strong electronic contribution to the STM contrast. Adapted from [42].

per ion, respectively. The three energy levels are indicated as I, II and III in 4.9 a. This energy difference is too small to conclude the thermodynamically favored lithium distribution at the interface. Still, the results clearly demonstrate that Li island formation is not hindered by the Coulomb repulsion between the Li^+ species in neighboring silica pores.

The second property after the interfacial binding energy that has to be analyzed in order to understand the driving force for the observed assembly effect is the lithium penetration process trough the silica top layer. This penetration process is associated with an energetic penetration barrier. Island formation would be favored if the lithium penetration barrier is lowered in the presence of preadsorbed Li^+ in adjacent pores at the interface, a mechanism that is indeed revealed in DFT. The initial penetration barrier for lithium is calculated to be ≈ 0.3 eV but gradually decreases when neighboring adsorption sites are occupied with alkali ions. In the limiting case of lithium incorporation into a pore with all six neighboring pores filled with other lithium ions, the activation barrier drops to ≈ 0.11 eV and atom penetration becomes more favorable. The reduction of the energetic penetration barrier is related to a lattice distortion induced by the preadsorbed Li^+ ions at the interface.

The lithium ordering process into $[\overline{1}\overline{1}1]$-oriented stripes on the silica/Mo(112) system cannot be treated with ab initio DFT calculations due to the mere size of the adsystem. However already a simple analysis of the Mo(112) screening response provides valuable insight into the origin of pattern formation.

Every adsorbate on a metal surface, especially if it holds an extra charge, perturbs the electron density of the support by initiating Friedel oscillations [106, 107]. Their periodicity is given by half the Fermi wavelength λ_F along a certain crystallographic direction, while their amplitude decays with $k_F r^{-2}$ as a function of distance r from the binding site (with k_F being the Fermi wave vector). Via such substrate-mediated interactions, adspecies are coupled over large distances on the metal surface, as they reciprocally influence the available charge density for binding. This perturbation is sufficiently strong to determine the spatial arrangement of adatoms and molecules on homogeneous surfaces, leading to distinct maxima in the pair-distribution function at multiples of $\frac{1}{2}\lambda_F$ [98, 99, 108–111].

A similar mechanism can now be applied to the present adsorption system. Each lithium ion creates a depletion zone in the Mo(112) charge density at multiples of $\approx \frac{1}{4}\lambda_F$ around its adsorption site, whereas the electron density increases at multiples of $\frac{1}{2}\lambda_F$ and λ_F. This is schematically depicted for a one dimensional Friedel oscillation in figure 4.10. The adsorption of another lithium atom will be unfavorable within the depletion zone while it might be facilitated in regions with higher electron density due to the superior screening ability of the substrate. The oversimplified picture of a one dimensional modulation along a line is of course not sufficient for the two-dimensional surface. The two-dimensional Friedel-type screening response is different along and perpendicular to the furrows of the Mo(112) surface, which is in accordance with figure 4.8 b. According to bandstructure calculations [112] and angle-resolved photoelec-
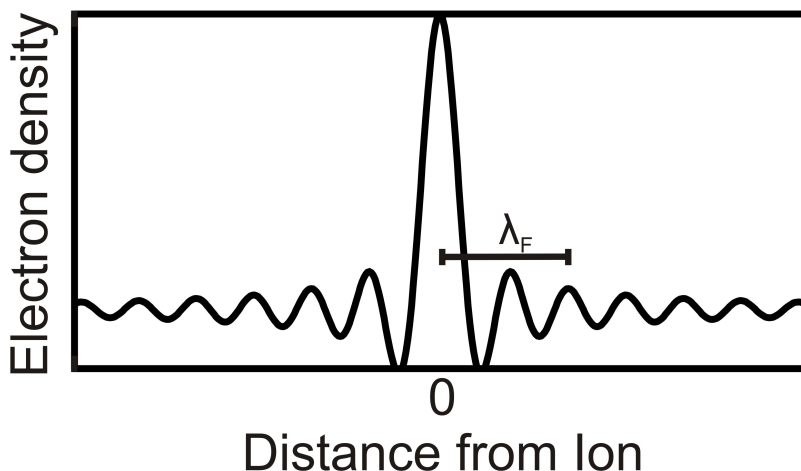
Figure 4.10: Schematic representation of Friedel oscillations. The electron density oscillates with a periodicity of $\frac{1}{2}\lambda_F$. The 0 position denotes the position of the perturbing ion. A possible second ion would prefer sites with distances of $N \times \frac{1}{2}\lambda_F$ from the first ion where the electron density peaks.

tron spectroscopy experiments [113], two surface resonances are of relevance to screen electronic pertubations along the $[\bar{1}\bar{1}1]$-oriented furrows with k_F=0.36 Å^{-1} (λ_F=17.5 Å) and k$_F^*$=0.86 Å^{-1} (λ_F=7.3 Å), respectively, whereas one band crosses the Fermi level at k$_F$=0.14 Å^{-1} (λ_F=45 Å) in $[\bar{1}10]$ direction. The states are surface resonances with a strong bulk contribution, not genuine surface states and therefore less susceptible to the presence of the silica film above. However, small shifts of the wave vectors can be expected on the silica covered surface with respect to the bare Mo(112) surface.

The periodicity of λ_F=45 Å along the $[\bar{1}10]$ direction matches the distance between neighboring lithium stripes almost perfectly suggesting that charge-density oscillations in the molybdenum surface are indeed responsible for the spatial distribution of the lithium ions. It is observed that lithium-rich stripes develop first with λ_F distance while the intermediate $1/2\,\lambda_F$ positions are only occupied at higher lithium load. The retarded occupation of the half-wavelength sites hints towards a residual influence of direct, repulsive interactions between adjacent lithium islands. Using a similar argument, also the less pronounced lithium-density modulations along the $[\bar{1}\bar{1}1]$ stripes can be explained. STM images taken at low lithium exposure and LEED data reveal a partly ordered lithium arrangement that is compatible with Friedel oscillations mediated by the surface resonance at k_F=0.36 Å^{-1}, which corresponds to a Fermi wavelength of λ_F = 17.5 Å , as shown in figure 4.7 c and figure 4.8. Its stabilizing effect on the Li$^+$ binding energy interferes however with direct interaction mechanisms such as electrostatic forces between the Li$^+$ and the template effect of the silica/Mo(112) film.

It should be noted that lithium ordering into $[\bar{1}\bar{1}1]$ oriented, interfacial stripes is also

supported by the strong anisotropy in the Mo(112) diffusion barriers. While lithium diffusion perpendicular to the pristine molybdenum furrows is activated by 0.75 eV, this value drops to 0.09 eV along the [$\overline{1}11$] direction [114]. The latter barrier rises to 0.27 eV in presence of the silica film; however, transient lithium diffusion remains possible along the furrows due to the thermal energy of the incoming atoms ($\approx$ 800 K when leaving the lithium dispenser). In contrast, hopping between the furrows is inhibited at the experimental conditions. Nonetheless, the succession of lithium rich and lithium poor islands can still be realized by inclining the stripes against the Mo[$\overline{1}11$] direction, a phenomenon that is indeed revealed in the STM data as shown in figure 4.7 c.

4.3.4 Lithium Induced Electronic Properties of the Silica Film

The deposition of higher lithium quantities leads to an agglomeration of positive ions at the metal-oxide interface. This has consequences for the electronic structure of the silica film which are demonstrated by conductance imaging and spectroscopy with the STM. As discussed in the previous sections 4.3.1 and 4.3.2, a first indication for a changed electronic structure comes from the large bias-dependent contrast between lithium rich and lithium poor surface regions. Similar to isolated lithium species, like the ones shown in figure 4.6, lithium-rich islands exhibit large apparent heights of 1.2 Å in images taken at elevated bias but are hardly visible at the Fermi level. The same effect is observed in simulated STM images and shown in figure 4.9 b. This indicates an electronic origin of the measured surface corrugation. The fact that lithium-rich stripes turn bright at higher bias values suggests the local availability of new conductance channels in those regions. STM conductance spectra taken on silica patches with different lithium content provide direct evidence for this assumption as demonstrated in the following and shown in figure 4.11 a.

The pristine, lithium-free film displays a smoothly increasing dI/dV curve with only a small kink at $\approx$ 3.0 eV. This kink marks the sudden availability of empty states for electron transport in the silica film. A similar step in the state density is revealed in the calculated LDOS which is shown in figure 4.11 and assigned to the onset of unoccupied Si-O hybrid states forming a precursor of the silica conduction band. Experimentally, the band onset E_c is defined by the bias value, where either the slope of the dI/dV curve becomes maximal or the dI/dV signal reaches 50% of the kink intensity. This is drawn with a dashed line in figure 4.11 a. This definition determines the band onset of bare silica at 2.9 eV. Complementary to this, another kink may be observed in filled state spectra at -3.6 eV. This provides an estimation of the band gap of the pristine silica film of $E_g \approx 6.5$ eV. Not surprisingly, it is smaller than in bulk SiO_2 ($E_g \approx 9$ eV) [115], reflecting the reduced oxide thickness and the residual influence of the metal support.

The kink in the empty-state spectra, being an indicator for the conduction band onset, now experiences a gradual shift to lower energies upon increasing lithium coverage, as shown in figure 4.11 a. Additionally, the absolute dI/dV intensity is getting lower and the spectra considerably broaden with increasing lithium load. This spectral broadening may be explained by a certain averaging over oxide areas with different lithium
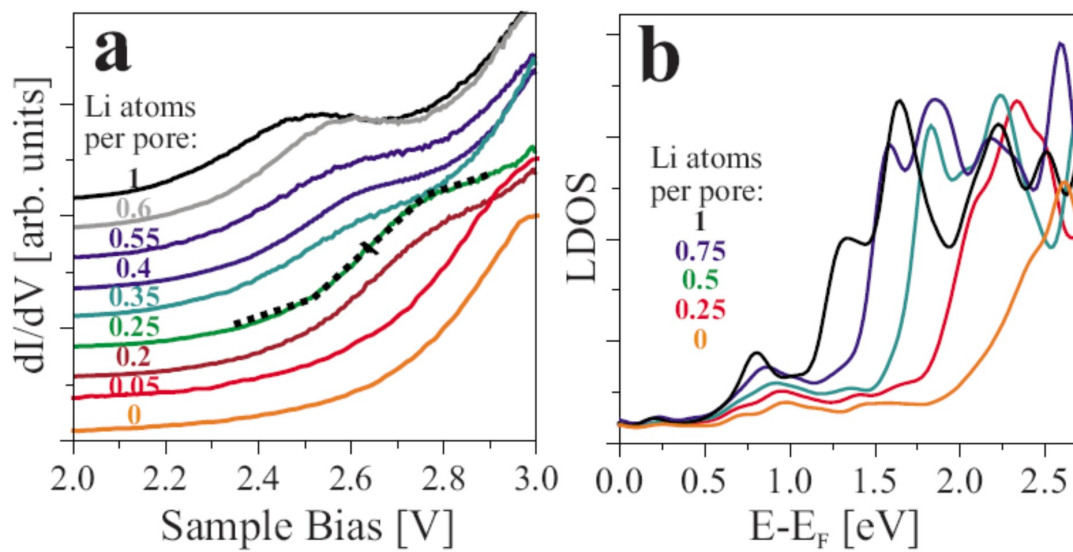
Figure 4.11: (a) Conductance spectra taken on silica/Mo(112) regions with different Li concentrations. The set point for spectroscopy is adjusted to 2.9 V; all spectra are offset for clarity. (b) Calculated silica/Mo LDOS as a function of Li concentration. The gradual down shift of the silica conductance states is clearly visible.

contents. A careful analysis of the experimental data indicates a monotonous down shift of the silica conduction band from 2.9 to 2.4 eV as the lithium coverage increases towards one atom per pore. The measured and calculated band shift is shown in figure 4.12 a. An even larger band shift is observed when the tip is positioned on top of a lithium-filled domain boundary, for this case the band onset shifts down to ≈ 2.3 eV.
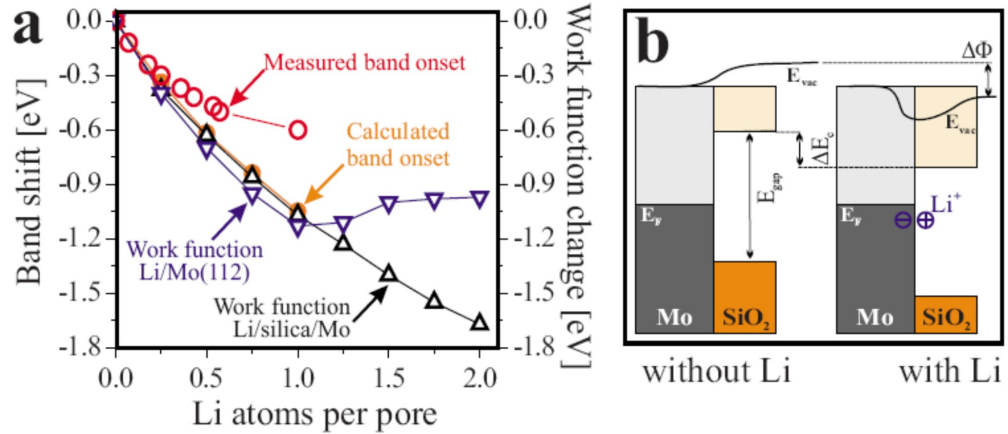

Figure 4.12: (a) Evolution of the measured and calculated conduction band onset and the silica/Mo(112) and Mo(112) work function as a function of Li coverage. (b) Sketch of the silica/Mo electronic structure before and after Li incorporation. The model visualizes the interrelation between the Li-induced surface dipole, the work function change $\Delta\phi$ and the down shift of the silica conduction states ΔE_c.

A spatial correlation between the topographic and electronic information from the lithium-doped silica film is obtained from several spectral series taken across one period of the lithium-induced superstructure. The dI/dV spectra shown in figure 4.13 a are recorded along the Mo[$\bar{1}$10] direction, thus perpendicular to a line of high lithium concentration, differentiated with respect to the bias voltage and displayed as a color-coded matrix. In this representation, the position of maximum slope that marks the band onset E_c is clearly visible due to the maximum in the d^2I/dV^2 signal. When moving the tip along the spectroscopy line, the band onset varies between 2.45 and 2.65 eV, indicating the inhomogeneous lithium concentration at the interface.

The lithium coverage θ at the interface varies along the spectral line. Whereas near-saturation coverage $\theta = 1$ (meaning one lithium atom per pore) is revealed for the lithium stripes, the intermediate regions have an E_c value that is higher but still well below the one for the pristine film, suggesting a substantial lithium concentration.

Another way to convey the same information is dI/dV mapping as a function of sample bias, as demonstrated in figure 4.13 b. In maps taken at 2.5 V, the local down shift
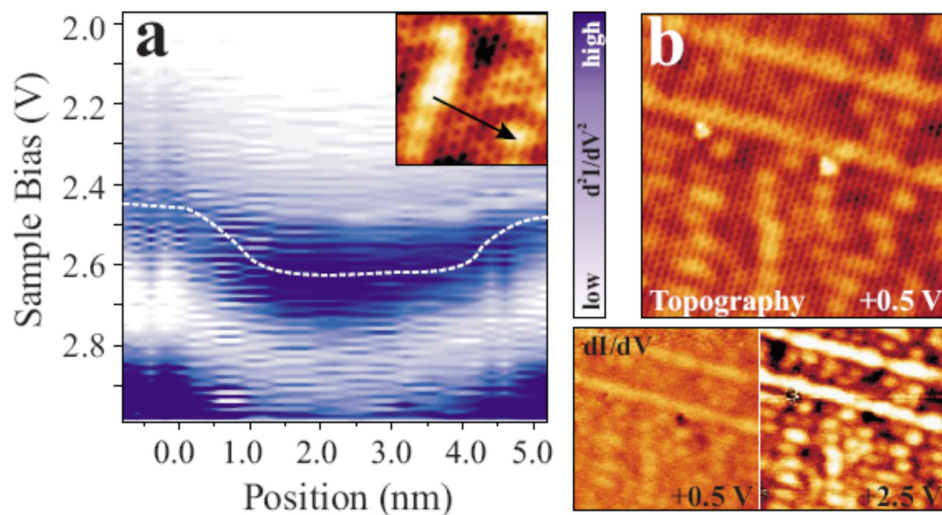
Figure 4.13: (a) Series of 64 dI/dV spectra taken along the line shown in the inset (STM: 0.5 V, 7 x 7 nm^2). Every spectrum has been differentiated with respect to the bias voltage and dark colors represent regions with large dI/dV slopes. The dashed line approximates the position of maximum slope, which is taken as a measure for the conduction-band onset. (b) Topographic and conductance images of silica/Mo(112) loaded with nominally 0.3 Li atoms per pore (20 x 20 nm^2). Whereas little dI/dV contrast is visible at low bias, Li-rich regions appear bright in dI/dV maps taken at 2.5 V.

of the silica conduction band is evident from the high conductance signal above the lithium-rich stripes, where electrons from the tip can tunnel into the conduction band, while lithium poor regions remain dark in the image because of the lack of available states. At a low sample bias of 0.5 V the dI/dV contrast is much weaker, indicating that the silica conduction band is not reached at any place of the surface.

The gradual down shift of silica conduction band with increasing lithium load can be rationalized by a work function reduction in the silica/Mo(112) system upon lithium incorporation, in agreement with the old Langmuir-Gurney model [103–105]. The positive surface dipole formed by interfacial Li^+ and respective image charges in the metal trigger a lowering of the vacuum energy of the system. As the oxide electronic states are mainly adjusted to the vacuum level, the band positions experience an equivalent down shift with increasing lithium load. This is schematically shown in figure 4.12 b.

The large band gap of the silica film prevents charge transfer from the substrate into the oxide film and a pinning of the energy levels. This explains the direct proportionality between the work function and the band onsets for wide band gap oxide systems. The dependence of work function ϕ and silica band onsets E_c on the lithium coverage θ has been calculated by DFT and is depicted in figure 4.12 a. It is found that for low lithium concentrations, the work function decrease depends almost linearly on the lithium coverage according to $\delta\phi / \delta\Theta$ = -1.2 eV. This leads to a work function decrease of $\approx$ 1.2 eV for the limiting case of $\theta = 1$ (one lithium ion per silica pore).

The slope gradually decreases for higher coverages but remains negative up to two Li^+ per silica ring ($\delta\phi / \delta\Theta$ =-0.65 eV/Li). Even at this maximum load $\theta = 2$ that could not be reached experimentally, the work function of the system is clearly higher than the tabulated lithium bulk value of 2.9 eV [116] (which would correspond to $\Delta\phi$= -2.0 eV in figure 4.12 a). This finding suggests that the charge transfer out of the lithium does not saturate and the alkali atoms remain cationic at the silica-molybdenum interface. Apparently, metalization of the alkali layer is prevented by the small number of atoms that fit into the silica-molybdenum interface region. Bulk values for the lithium work function are only expected if all interfacial sites are saturated and lithium starts nucleating above the oxide surface. Although this cluster formation is observed experimentally, as shown in figure 4.7 d, the associated work function is not accessible to STM anymore due to the vanishing influence on the silica conduction states in this case.

Unlike for the case of Li/silica/Mo(112), the universal work function versus coverage curve is restored on the bare Mo(112) surface as shown in figure 4.12 a. In this case ϕ initially decreases with lithium coverage but runs through a minimum at $\Theta \approx$1 and increases again toward the lithium-bulk value. The different behavior of the oxide-covered system can be traced back to the special role of the interfacial oxygen atoms in the silica film, which act as an additional sink for the lithium electrons and further screen the lithium charge distribution at the interface. Not surprisingly, the universal coverage dependence of ϕ appears when the alkali atoms do not bind at the interface

but on top of the oxide film where screening is inefficient. Such a behavior is revealed, for instance, for potassium atoms, which are too big to penetrate the silica nano-pores [90].

The experimentally determined onset of the silica conduction band mimics the computed trend with lithium coverage, although absolute values are about 40% smaller as shown in figure 4.12 a. This discrepancy can be explained by the known deficiency of DFT in reproducing the correct band gaps of insulating materials. On the experimental side, the lithium-induced band shift might partly be compensated by the tip-induced counter field during spectroscopy. Nonetheless, experimental and theoretical data consistently demonstrate the strong effect of incorporated Li^+ on the silica/Mo(112) work function. The effect of the modified electronic structure upon lithium dosage on the silica adsorption behavior is adressed in the next section 4.4.

4.4 Modified Adsorption Properties: Gold on Silica

The stabilization of highly dispersed metal particles on oxide supports is of decisive importance for applications in heterogeneous catalysis [91] and for the development of sensor, magnetic storage, and optoelectronical devices [117–119]. High catalytic activity often depends critically on the dimension of the active particles and breaks down when the particle size increases and the adsorbate material adapts bulk like properties [120]. This has drawn considerable attention especially for the case of gold where the catalytic activity is completely confined to small particles [121].

The anchoring of metal deposits to inert, wide-gap oxides usually involves surface defects that offer substantially higher binding energies than the regular surface [122, 123]. The underlying binding mechanisms rely on the locally different chemical environment created by the defect. In order to be independent of defect concentrations and retain other, wanted, properties of the substrate, a mechanism that globally modifies the adsorption properties of an oxide would be ideal. For the case of lithium doped silica such a new stabilization mechanism is presented in this section. It is shown that the binding happens independent of defect sites and exploits the possibility to globally tailor the charge state of adparticles on thin oxide films.

Charged adspecies are of special interest because they are able to activate new interaction schemes with the oxide surface such as Coulomb attraction towards oppositely charged oxide ions, polaronic distortions of the oxide lattice, and interactions with image charges formed in the metal underneath [124]. Therefore they experience an enhanced binding strength to the oxide film with respect to their neutral counterparts. Charging occurs via electron tunneling between low-lying affinity levels in the adsorbate and the electron sea in metal support below the oxide spacer. The direction of the electron flow is governed by the work function ϕ of the metal-oxide system [125]. For systems with small work function values electrons readily tunnel from the metal to the adsorbate leading to negatively charged adspecies. Charge-mediated binding mech-

anisms have been revealed by theory and experiment for gold on different thin film systems such as MgO grown on Ag(001) [12, 124, 126–128], alumina on NiAl(110) [129], and FeO supported on Pt(111) [130, 131]. In the first two examples negative charging of the gold takes place, whereas the gold becomes cationic in the latter case, reflecting the high ϕ value of the FeO/Pt system.

However, charging and stabilization of adparticles does not occur spontaneously on every oxide film. On silica/Mo(112) films, for example, gold remains neutral and is unable to bind to defect-free oxide patches [84, 132]. Even at low temperatures it diffuses towards defect sites in the oxide film. Charge transfer is inhibited in this case by the negative surface dipole associated with the silica growth, which raises ϕ and acts against an electron flow into the gold [125]. Doping the film with electropositive species, e.g. alkali atoms reverses the oxide induced dipole as discussed in section 4.3 of this thesis. Calculations have shown that lithium, sodium, or potassium easily ionize on the silica film, thereby lowering the work function and enabling electron transfer from the metal substrate into gold adspecies [13, 90].

In this section experimental prove aimed at demonstrating that a lithium-doped silica/Mo(112) film is indeed able to anchor gold particles is presented. All DFT calculations relating to this project have been performed by Dr. Umberto Martinez from the group of Prof. Pacchioni in Milano.

4.4.1 The Modified Silica Film

As discussed in section 4.3, the global properties of the silica film may be altered by doping the film with lithium atoms. This has been investigated using STM and STS as described in the previous sections.

The implications of the resulting work function decrease for the adsorption properties of the the silica/Mo(112) system are discussed in this section for the case of gold. It is demonstrated that the lithium doping creates a completely new adsorption system with many desirable properties. The main new property of this system is the charge transfer that occurs because of the lower work function and enables electrons to tunnel from the metal support to adspecies on top of the film. This property opens up a whole range of new possibilities because charged adspecies in general display a different behavior than their neutral counterparts. One difference is that charged species repel each other and thus tend to form smaller aggregates. Another important aspect is that the charging process itself comes along with chemical selectivity. In order to gain energy upon charge transfer into an adatom, this adspecies needs to have a low lying affinity level. For the case of MgO grown on silver this leads to a chemical selective charging process: While gold with its low lying *6s* level binds anionically to the surface, palladium remains neutral [124]. For this case both, gold and palladium bind strongly to the surface, therefore the chemical selectivity is only associated to the charging process and not to the binding. As described in the next section for the case of gold on silica, the selective charging can also lead to a chemically selective binding behavior. A detailed description of charge transfer into adspecies on various oxide films can be found in [5].

4.4.2 Gold Adsorption on the Modified Silica Film

The lithium doping is responsible for a dramatic change in the adsorption behavior of the silica/Mo(112) film with respect to gold as shown in figure 4.14. Without lithium gold atoms are unable to bind to the defect-free film and rapidly diffuse on the surface until they become trapped at domain boundaries between two oxide patches as shown in figure 4.14 a. These anti phase domain boundaries consist of larger pores with eight silicon atoms instead of the regular six membered pores of the defect free oxide film. Only the larger diameter of those pores allows the accommodation of the gold. Larger three-dimensional gold particles may then start to grow from those defect-bound gold atoms at the line defects as shown in figure 4.14 a and in [84, 85, 133]. After lithium deposition this adsorption behavior completely changes. Gold atoms and clusters now appear everywhere, including the defect-free oxide terraces away from the domain boundaries, as demonstrated in figure 4.14 b.

For low gold coverages mainly single adatoms with spherical shape and a height of ≈ 0.8 Å as in figure 4.14 c are observed. Since those features display a spherical shape and represent a protrusion at different biases it is concluded that the gold atoms are located above the oxide film. Also the absence of star like shapes which were identified as fingerprints for embedded species [42, 84] suggests a gold location above the oxide surface. Apparently gold is now able to bind to the pristine silica surface without the need to enter the nano-pores. This conclusion is further corroborated by the fact that single adatoms are found on top of the -Si-O- network and not above the center of the nano-pores. The gold atoms and clusters mostly attach to the lithium-rich stripes where the work function is lower but occasionally also bind to lithium-poor regions as visible in figure 4.14 b.

For an increasing gold coverage, three-dimensional particles start to appear on the modified surface with an average density of 2.5×10^{12} cm^{-2}. The aggregates adopt a prolate shape with a large height to diameter ratio of ≈ 0.3 even though triangular and hexagonal base planes are also readily observed as for example in figure 4.14 e and f. In STS experiments the gold monomers do not show conductance peaks that would indicate tunneling into defined atomic orbitals.

The experimentally observed stabilization of gold atoms and clusters on lithium-doped silica/Mo(112) films is fully consistent with the predictions derived from the DFT calculations. In those calculations three local energy minima are revealed for three different adsorption sites on the silica film. These sites are above an oxygen atom in [$\bar{1}10$]-oriented Si-O-Si bridges (site 1), above a [$\bar{1}\bar{1}1$]-oriented Si-O-Si unit running on top of a protruding molybdenum row (site 2), and above the center of a silica ring (site 3). These sites are indicated in figure 4.15 a. For an assumed mean coverage of one Li$^+$ per pore, the binding strength of a gold atom in the most favorable position 1 is found to be 1.33 eV. This is an order of magnitude stronger than for the undoped film. The binding energies of the other two adsorption sites are found to be 0.18 eV and 0.34 eV respectively. Those values are much smaller and hence unimportant for the adsorption behavior.
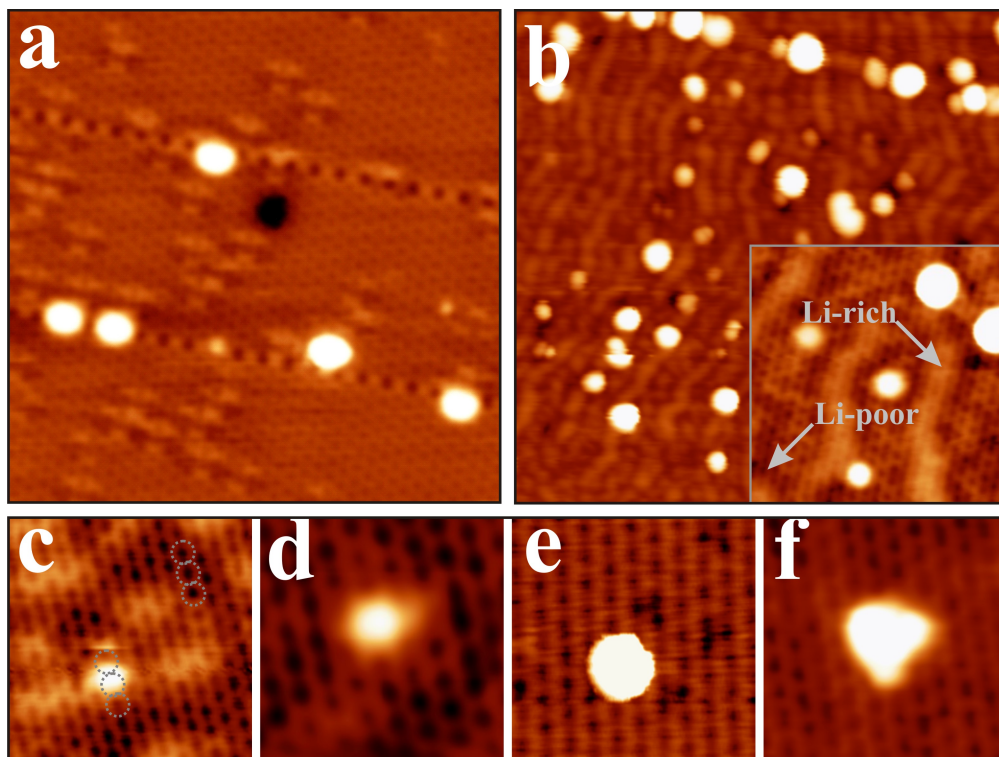
Figure 4.14: (a) Pristine (2.0 V, 20 x 20 nm^2) and (b) lithium-doped silica film after deposition of 0.1 mono layer Au (2.0 V, 50 x 50 nm^2). Whereas Au attaches exclusively to domain boundaries for the undoped film, it binds to defect-free oxide patches after incorporation of 0.7 lithium$^+$ ions per silica pore. The inset in (b) shows an oxide region with enhanced resolution (0.6 V, 11 x 11 nm^2). (c) Single Au atom on lithium-doped silica. The adatom does not sit above a pore but between two hexagonal rings as marked by the dashed circles. (d)-(f) Au clusters with increasing size stabilized on lithium-doped silica. The Au growth follows the Vollmer-Weber regime and leads to the formation of 3D particles.
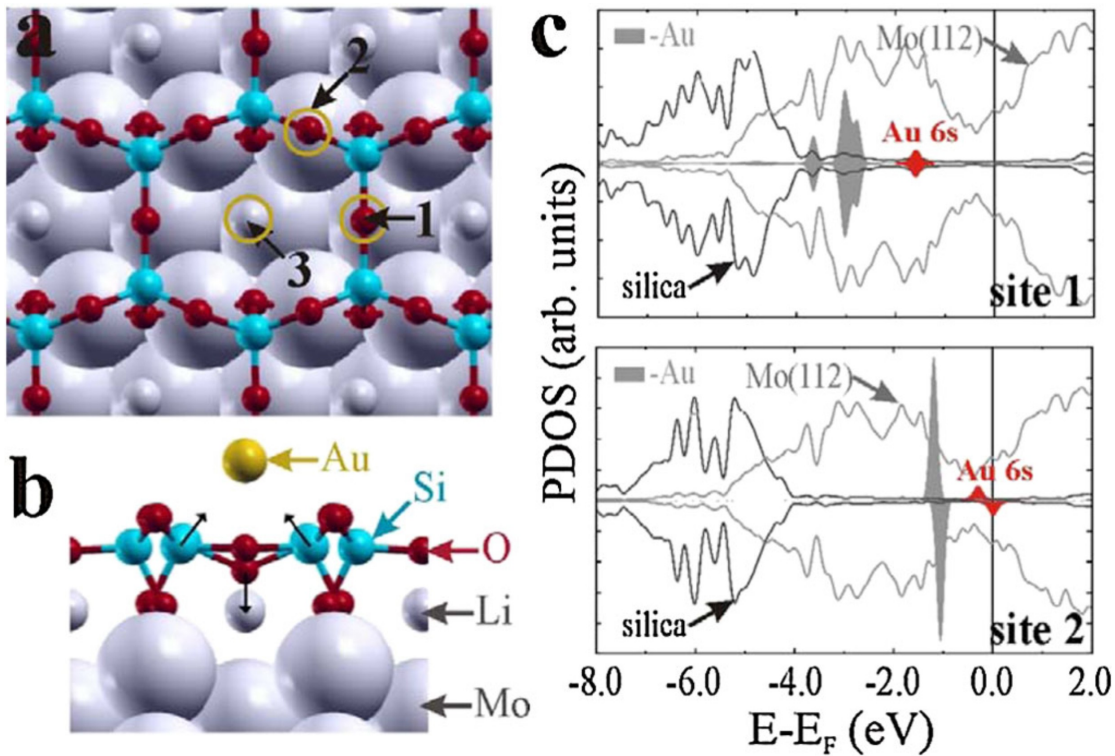
Figure 4.15: (a) Structure model showing potential Au adsorption sites on silica/Mo(112) doped with one Li$^+$ per pore: (1) on the O atom of a [$\bar{1}$10]-oriented Si-O-Si bridge that suspends two Mo rows, (2) on a Si-O-Si bridge on top of a Mo row, and (3) above a nanopore filled with an interfacial lithium atom. (b) Schematic representation of the polaronic distortion around the adsorbed Au atom on site 1. (c) Partial density of states projected onto an Au atom adsorbed on position 1 (top) and 2 (bottom). Adapted from [13]

The combination of experimental results and DFT calculation allows for a description of the mechanism behind the gold adsorption. LDOS calculations reveal that the gold adatom in the preferred position has a completely filled Au *6s* orbital and zero spin density. This indicates the transfer of one extra electron from the support into the gold atom with respect to the neutral gas phase gold species. The neutral gas phase gold atom has a singly occupied *6s* orbital and therefore also a net spin. In figure 4.15 c the partial density of states for the adsorbed gold atom is shown for two different adsorption sites. Only for the most favorable adsorption site 1, the gold *6s*orbital completely shifts below the Fermi-level. This indicates that a charging only happens at this position and is therefore crucial in the binding process. The question of charge in the gold ad-species is addressed by calculating the Bader charge value of -0.8 $|e|$. This charge leads to a strong polaronic distortion of the silica as a response to the electronic perturbation by the negatively charged gold as indicated in figure 4.15 b. The nominally positively charged silicon atoms move towards the negatively charged gold, while the nominally negatively charged oxygen atoms are repelled by the negative charge of the gold. This lattice distortion plays a crucial role in stabilizing the charge state of gold, and is only possible for this particular adsorption site 1, where the oxygen atom bridges the [$\overline{1}\overline{1}1$]-oriented furrow of the Mo(112) surface. For the two other local binding minima of gold, a significant lattice distortion is not possible because the negatively charged oxygen atoms cannot move towards the surface. Therefore the charge transfer from the molybdenum support into the gold is suppressed and the interaction energy remains relatively small.

A polaronic distortion has also been found in other examples for gold adsorption on thin ionic films, e.g. NaCl on Cu(111) [134] and MgO on Ag(100) [124], and seems to be of general importance to stabilize charged species on ionic films. Not surprisingly, the charging of gold atoms is most efficient for a low silica/Mo(112) work function and hence for high lithium coverage. The formation of anionic gold prevails, however, for a minimum lithium content of one atom per four silica pores although the gold binding energy to [$\overline{1}10$]-oriented Si-O-Si units decreases to 0.48 eV in this case compared to 1.33 eV for one lithium per silica pore.

The strongly bound Au^- species on a lithium-doped silica/Mo(112) film is now able to act as a nucleation center for particle growth. The resulting deposits adopt pronounced 3D shapes as shown in figure 4.14 e and f, which indicates a rather small overall Au-silica adhesion. Also DFT calculations demonstrate that an Au_{20} cluster with pyramidal shape is by 0.97 eV more stable than a flat-lying 2D island of similar size. Although this energy difference is smaller than between the respective gas phase isomers (1.9 eV), the Au-Au and not the Au-support interaction dictates the growth regime of gold particles on the silica film. This finding is easily explained by the fact that strong Au-silica bonds are only formed to oxygen atoms in the [$\overline{1}10$]-oriented Si-O-Si bridges, while on adjacent surface sites the amount of charge transfer and hence the gold binding strength are much smaller. The gold particles are thus pinned to distinct positions in the silica film and a true 2D interaction is absent. On MgO/Ag(001) thin films in contrast, negative charging takes place for every gold atom in contact with the

MgO [124, 127] and single-layered gold islands develop due to this spatially homogeneous adhesion [12, 128].

This study demonstrates that the silica/Mo(112) system is a suitable system for stabilizing potentially interesting adspecies on top of the film. This might be of relevance for chemical and catalytical purposes since the particles on the film are exposed to the surrounding atmosphere and would readily react with molecules from the gas phase. However also the opposite effect might be interesting for other purposes: stabilizing atoms inside the film in order to protect them from any unwanted reactions with the surrounding atmosphere. The unique properties of the porous silica are therefore not only suitable to tailor the chemical properties of the metal-oxide system. In the next section a route towards the creation of an artificial system with tailored magnetic properties is presented.

4.5 Putting the Silica-Matrix to Work: Single Fe-Atoms at the Metal-Oxide Interface

Not only tailored chemical properties offer big potential for possible applications. Also tailored physical properties such as magnetic behavior offer a wealth of interesting applications if controlled in an easy and reproducible way.

The system silica on molybdenum turned out to be a suitable support system to realize single-atomic magnetic units. Very small, and ideally single-atomic, magnetic units would be of importance for a wide field of applications, especially for information storage in magnetic hard drives.

The storage capacity of commercial magnetic hard disks has exponentially increased over the last several years, largely following a variation of Moore's famous law that has originally been formulated to describe the exponential growth of the number of transistors per area [135] in integrated circuit technology. This immense progress in storage capacity was achieved by applying new read-out technologies based on the giant magneto-resistance effect [136], but also because of ever smaller areas needed to store one bit of information on a hard disk. In the present state-of-the-art technology, one magnetic bit comprises an area of roughly 10^3 to 10^4 nm^2 in a Co-Cr-Pt alloy film. In the next steps of miniaturization, the continuous magnetic films could be replaced by ordered arrays of Fe, Co, or Ni clusters with superparamagnetic properties fabricated via wet-chemical synthesis or bufferlayer assisted growth [117, 118, 137]. However, the ultimate goal of down-scaling would be a single adatom or molecule that represents one magnetic unit. The information could then be retained in the orientation of a single magnetic moment and not in the collective magnetization of hundreds of atoms. Experiments along this line have been performed for single magnetic adatoms, e.g. Co and Mn [138–140] and molecules, e.g. CoPc and FePc [141, 142], employing magnetic dichroism and STM. However, there are fundamental problems in the use of magnetic atoms and molecules. The magnetic building blocks need to be arranged in regular

arrays and stabilized against diffusion and aggregation at room temperature. Furthermore, the interaction of an isolated moment with its environment has to be balanced in a way that controlled switching of the spin direction is possible while unwanted thermal fluctuations are suppressed. Only if these structural and magnetic requirements are fulfilled, single adatoms and molecules might become key elements in the next generation of storage devices. For the system iron in silica/Mo(112) an approach is presented that focuses on the structural side of this problem and marks a step forward for some of the requirements mentioned above.

The ultrathin silica/Mo(112) film that has been described in the previous sections of this thesis and in greater detail elsewhere [74, 76, 77, 82] allows the stabilization of single magnetic atoms in near-surface sites even at elevated temperatures. The film can be considered a two-dimensional counterpart of a porous silicate. The in-plane -Si-O- units form six-membered rings of 5 Å diameter which enclose a hole reaching down to the molybdenum surface. As shown in the previous sections of this thesis and other experiments [84–86], those oxide nano-pores can be loaded with suitable metal atoms such as lithium, silver or palladium, whereas other atoms such as gold are too large for penetration. As previously discussed, the incorporation of metal atoms has been used to tailor the intrinsic properties and the adsorption behavior of the oxide material on the local and global scale. The porous structure of the silica film may also be exploited to produce a thermally stable ensemble of iron monomers. The incorporation of iron into the oxide matrix has a number of advantages with respect to conventional atom deposition onto flat metal or oxide surfaces. Leaving the adsorption site at the interface is associated with a substantial energy barrier [85, 132], therefore iron is stabilized against diffusion and desorption even at elevated temperature. Besides that, only one iron atom can enter each pore, therefore aggregation of iron is prevented. Finally the iron is well protected against environmental influences as the silica surface is chemically inert and does not interact with molecules from the gas phase [83].

Incorporation of iron into the silica/Mo(112) film is therefore a promising route to fabricate a dense ensemble of monomeric magnetic entities for potential storage applications. The unique properties of the Fe/silica system have been studied with STM and STS in the framework of this thesis as well as with DFT [143]. The results are presented in the following sections.

4.5.1 Structural and Electronic Properties of Fe-Atoms in the Silica Film

Iron is deposited from a high purity rod in an Oxford Scientific electron beam evaporator onto the freshly prepared silica film at 200 K. After the physical vapor deposition characteristic features start to appear in STM images. Figure 4.16 a shows an overview STM image of the silica surface after deposition of $\approx 1.5 \times 10^{13}$ iron atoms per cm^2 or correspondingly 0.04 atoms per silica pore. Two oxide terraces are exposed, both being fully covered by the hexagonal hole pattern that is the characteristic fingerprint for the porous film structure. The uniform film appearance is disrupted by a number of faint,

randomly distributed protrusions which are assigned to the iron species. Occasionally, larger maxima with 1-4 Å height are observed that are related to small iron clusters.
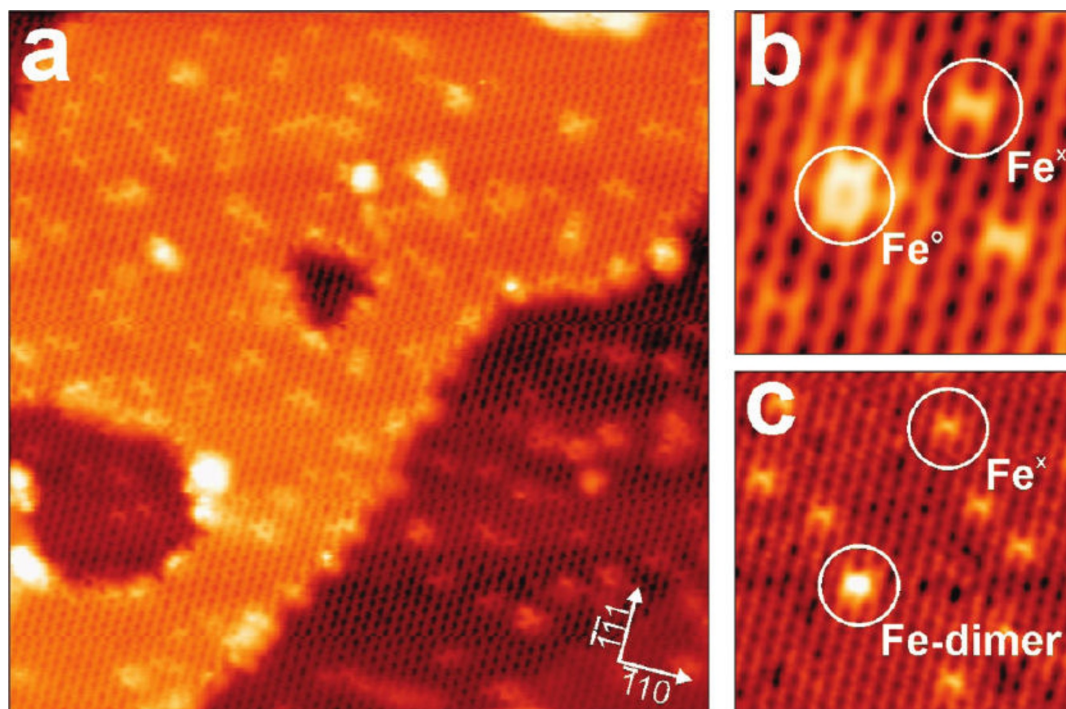

Figure 4.16: (a) STM image of th silica/Mo(112) surface after deposition of 0.04 Fe atoms per silica pore (U_s = 0.6 V, 40 x 40 nm^2). (b) Close-up STM image (U_s = 0.5 V, 5 x 5 nm^2) with subsurface Fe^o and Fe^x species marked by white circles. (c) STM image (U_s = 0.5 V, 10 x 10 nm^2) showing an Fe dimer as well as a few monomeric species.

Upon closer investigation mainly two different species can be distinguished in well resolved STM images such as the ones in figure 4.16 b and c. Most frequently the iron features display an X-like shape which is located at the intersection of two six-membered silica rings and oriented along the Mo[$\bar{1}$10] direction. Those features are referred to as Fe^x. The apparent height of the Fe^x features shows a characteristic bias dependence and increases from 0.3 Å at 0.1 V sample bias to a maximum of 0.8 Å at 2.5 V as shown in figure 4.17.

The second readily observed iron induced species is a ring-like protrusion referred to as Fe^O. In the explored bias window the Fe^O features appear slightly brighter than the Fe^x features. They coincide with the size and shape of a single -Si-O- ring of the silica film. This observation is similar to the two adsorption sites that have been found for lithium atoms as discussed in section 4.3.1 of this thesis. The Fe^O features are roughly ten times less abundant than the Fe^x species. Upon increasing iron exposure, larger adstructures develop on the surface. The smallest of them still has atomic dimensions and occupies the same adsorption sites as the Fe^O species. Its apparent height is two
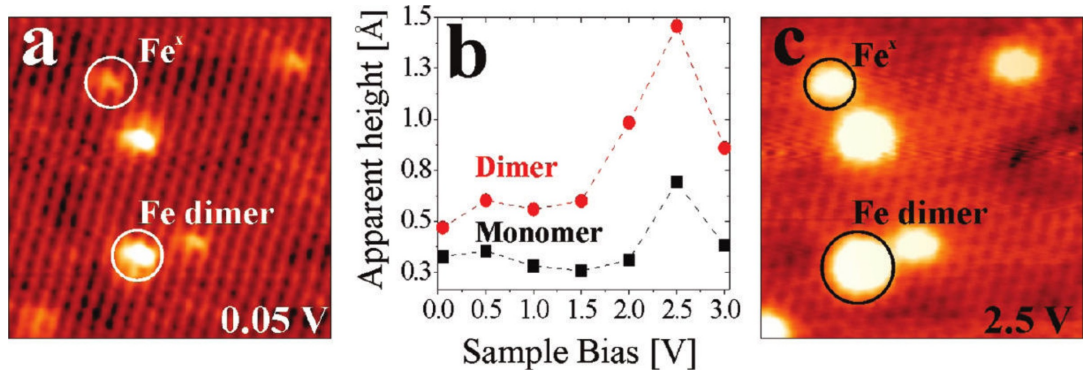
Figure 4.17: (a and c) STM images of the Fe/silica/Mo(112) system taken at two different bias voltages (10 x 10 nm^2). (b) Bias dependence of the apparent height measured for an interfacial Fe^x atom and a dimer.

times larger than that of the original Fe^O features and increases from 0.5 Å at low bias to 1.5 Å at 2.5 V as shown in figures 4.16 c and 4.17 b and c. Furthermore, a few larger iron induced clusters emerge on the surface and quickly grow in size with increasing metal exposure.

Assigning the experimentally observed features to exact atomic configurations proves difficult without the input of theory. With the help of DFT calculations performed in the group of Prof. Pacchioni distinct iron adsorption configurations could be assigned [144]. According to those calculations the iron atoms are expected to enter the silica pores and reach high-energy binding sites at the metal-oxide interface. The calculated penetration barrier amounts to 0.3 eV [143], a value that is easily overcome by the thermal iron atoms arriving with $\approx$ 0.1 eV from the hot rod in the evaporator. This is not surprising since a similar behavior has been found for lithium, silver and palladium as discussed in the previous sections and in [42, 84, 85]. However the nature of the penetration barrier is found to be quite different for the different elements. While lithium ionizes and penetrates as a cation forming bonds with the silica oxygen atoms on its way, iron as well as silver atoms diffuse into the pores as neutral species. In this case, the barrier is related to repulsive interactions between the charge density at the oxide surface and electrons in the valence orbitals of iron and silver.

The iron adsorption positions at the interface with respect to the molybdenum lattice underneath are calculated to be similar to the ones found for lithium adsorption on the same system. Both sites are Mo-Mo bridge positions at the silica/Mo(112) interface. The one that leads to the Fe^O features is located directly in the middle of a silica ring with an associated binding energy of E$_B$ = 3.3 eV. The other adsorption site that leads to the Fe^x features lies directly below a [$\bar{1}$10]-oriented Si-O-Si bridge and has a binding energy of E$_B$ = 3.6 eV. These configurations are depicted in figure 4.18 a and b respectively. In the first configuration, the *4s* orbital of the iron atom hybridizes with the silicon and oxygen atoms of the oxide ring above, resulting in a local increase of the unoccupied

state density (LDOS) at the surface, as shown in figure 4.18 c. This particular silica ring now appears brighter in empty state STM images than neighboring ones, a situation that is perfectly met by the ring-shaped Fe^O species in figure 4.16 b. In the second case, the iron *4s* orbital hybridizes only with the Si-O-Si bridge and the LDOS enhancement is confined to a [$\bar{1}$10]- oriented bar in the silica surface, leading to the X-shaped features described above.

The iron forms strong covalent bonds with the molybdenum support and becomes slightly positively charged for both binding configurations. The calculated Bader charges are $+0.18|e|$ and $+0.03|e|$ for the Fe^O and Fe^x species respectively. However, the binding contribution of the molybdenum does not affect the STM image contrast, as the Mo-Fe hybrid states are localized at the metal-oxide interface and not expected to overlap with the tip wave functions.

The strong bias dependent height of the iron features that can be observed in STM images is due to an intermixing of the iron *4s*orbital with the silica conduction states. The height is larger when tunneling with higher bias as evident in figure 4.17. Indeed, the calculated iron-induced state density has a maximum at around 2.1 eV as shown in figure 4.18 c, which is why the incorporated iron appears brightest in STM images taken at 2.5 V. This can be seen in figure 4.17 b. Again a small discrepancy between the experimental value and the theory occurs which reflects the known deficiency of DFT to reproduce the band gaps of insulators.

Counting many STM images reveals a ten times higher abundance of Fe^x compared to Fe^O species. This may be explained by the 10% higher binding energy of the Fe^x features. The statistic for a large image is shown in figure 4.18 d. The difference in binding energy may be rationalized by the additional Fe^x interaction with the oxygen ion above which does not occur for the Fe^O in the middle of the pore. Interestingly enough, chemically active atoms seem to have a high tendency to occupy both interfacial binding sites, as is the case for iron and lithium, while the more inert species favor adsorption in the ring positions, as observed for silver and palladium. Consequently, both X- and ring shaped features are observed after exposing the silica film to lithium as discussed in the previous sections, while only ring-shaped entities appear after silver and palladium depositon [84, 85].

Dimer formation

Even though most features that are observed in STM images can be assigned to one of the two possible single-atomic iron features, also some larger iron-related protrusions are visible, for example, in figure 4.16 a. Those larger features are assigned to iron adatoms that have attached to a subsurface species acting as surface anchor. This is a mechanism that has been previously observed for the case of palladium [86]. To verify such an anchoring mechanism, the properties of vertical dimers consisting of an interfacial and a surface iron atom have been studied with DFT [144]. While both, the Fe^x and Fe^O species, are able to anchor atoms on the surface, their binding potential differs dramatically. Whereas an Fe^O atom located below a silica ring binds a surface iron atom with 1.47 eV, this value drops to 0.24 eV for an Fe^x atom located below a Si-O-Si bridge.
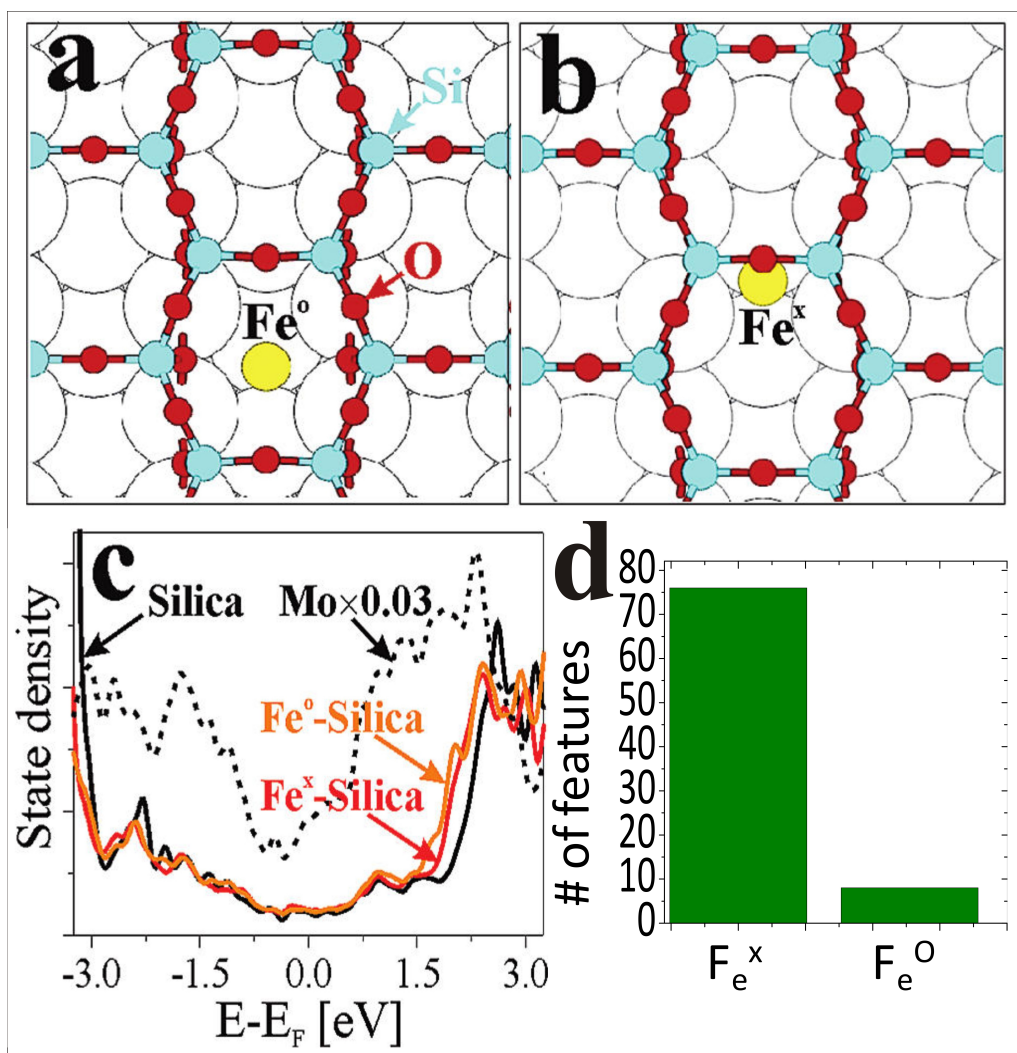
Figure 4.18: Structure model for Fe atoms in two different binding sites at the silica/Mo(112) interface, (a) below a silica ring and (b) below a [$\bar{1}$10]-oriented Si-O-Si bridge. (c) Calculated LDOS of silica/Mo(112) before (black curve) and after Fe incorporation (red and orange curves). The down-scaled Mo LDOS is depicted by the dashed line. (d) Abundance of the two Fe features as counted on several STM images. Partially adapted from [143]

The strong binding to Fe^O species is compatible with a short interatomic distance of 2.14 Å. In contrast, iron surface atoms cannot approach the Fe^x species due to steric repulsion of the silicon and oxygen atoms. A much longer bonding distance of 3.77 Å is the result and the binding remains weak in this case. Therefore it can be concluded that dimer formation is restricted to subsurface species in the Fe^O configuration, while the majority species in the Fe^x configuration remains monomeric even at high coverage.

4.5.2 Higher Fe Exposures

DFT calculations reveal that atom attachment to an existing iron dimer occurs spontaneously and is highly exothermic [143]. Therefore each dimer constitutes the seed for a larger iron aggregate. As discussed in the previous section, dimer formation is only favorable at the minority species Fe^O. Therefore the number of subsurface Fe^O species in ring positions is an upper limit for the number of surface clusters. To verify this correlation, samples with increasing iron content have been prepared and analyzed with the STM. The results can be found in figure 4.19. It turns out that the number of both, interfacial, monomeric iron species (Fe^O and Fe^x together) and surface clusters increases linearly with exposure time. This is indicated in figure 4.19 f, with the black and red lines, belonging to the left scale. Independent of the exposure time in the investigated coverage regime, the ratio between the two different subsurface species Fe^O and Fe^x of roughly 0.1 remains constant as indicated in figure 4.19 f with the green line, belonging to the right scale.

For the investigated coverages this also leads to a constant ratio of 0.1 between the number of subsurface, monomeric iron species and surface clusters of around 0.1, as expressed by the following formula:

$$\frac{N_{Cluster}}{N_{Fe^x} + N_{Fe^0}} \approx 0.1 \tag{4.1}$$

Even upon higher iron coverage there is no saturation effect in the density of incorporated iron monomers, as deduced from the monotonous, positive slope of the black line in figure 4.19 f. This finding suggests that the interplay between incoming atoms and preadsorbed iron species at the interface is negligible in the explored coverage window. There seems to be no diffusion of incoming iron atoms on the oxide surface prior to film penetration, instead the iron penetration occurs exclusively at the moment of impact when the atom has sufficient thermal energy to overcome the barrier. After a finite number of diffusion steps no penetration is possible. Iron atoms that fail to penetrate the silica top layer at the first attempt become trapped in a physisorption potential of 0.14 eV depth and rapidly diffuse on the oxide surface. They are stabilized by attaching either to an Fe^O species forming a dimer or to a preexisting iron cluster. The fact that the ratio between subsurface and surface features is similar to the initial Fe^O to Fe^x ratio corroborates the decisive role of the Fe^O species as surface anchors in the aggregation process. Surface defects, on the other hand, seem to play only a minor role in cluster
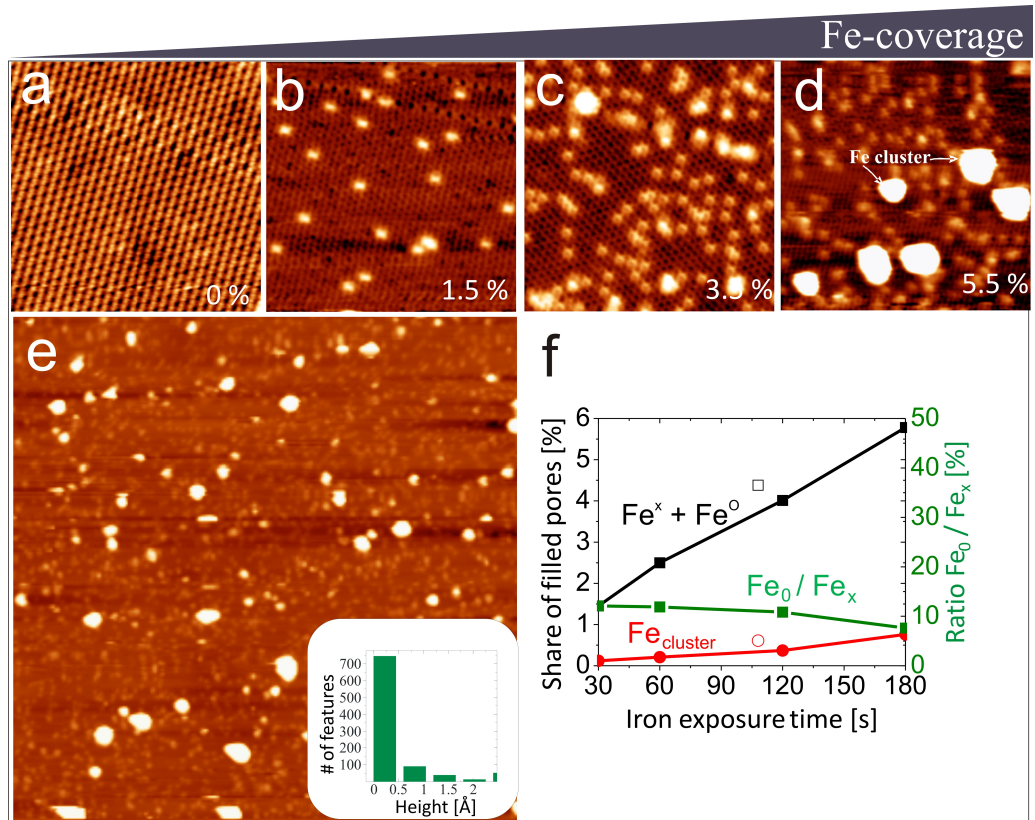
Figure 4.19: STM images of the silica/Mo(112) film after different Fe exposures, upper row : U_B=0.5 V, 18 x 18 nm^2; percentage of pores filled with iron: (a) 0 %, (b) 1.5 %, (c) 3.5 %, (d) 5.5 %. (e) Overview image (U_B=0.5 V, 50 x 50 nm^2) at higher coverage (5.5 %), inset shows the height distribution of features. (f) Density of subsurface, monomeric (black) versus surface clusters (red) as a function of the exposure time and ratio between Fe^x and Fe^O (green line, right scale). Closed and open symbols depict results obtained for Fe deposition at 200 and 300 K, respectively.

formation, reflecting the high structural quality of the oxide film.

After discussing the abundance of the different features, also the number of iron atoms stored in the different positions is of interest. The ratio between subsurface (n^{sub}) and surface (n^{surf}) iron atoms yields additional insight into the penetration behavior of the iron atoms through the oxide film. This ratio should follow an Arrhenius behavior as a function of the penetration barrier:

$$\frac{n^{sub}}{n^{surf}} \propto e^{\frac{-E_{barr}}{kT}} \tag{4.2}$$

This may be exploited to estimate the associated barrier height. Hereby n^{sub} is simply determined by counting the monomeric species Fe^O and Fe^x and the number of clusters on the surface since they require one subsurface anchor each. On the other hand n^{surf} needs to be approximated from the density and height of the iron clusters, assuming a hemispherical cluster shape and a bulk iron lattice constant. Analyzing several STM images with different iron coverages gives a n^{surf} to n^{sub} ratio of approximately 10, manifesting the large number of atoms stored in the surface clusters. Using T = 1100 K for the temperature of evaporated iron atoms, the barrier height calculates to 0.23 eV, which is comparable to the DFT value of 0.3 eV. Apparently, the probability to overcome the barrier is mainly determined by the thermal energy of the iron atoms and not by the substrate temperature. This conclusion is supported by the fact that the ratio between subsurface to surface species could not be modified by changing the sample temperature during iron exposure from 300 K to 200 K which is indicated in figure 4.19 f with the open symbols.

In summary, although most of the features are monomeric subsurface species the majority of iron atoms is stored in the few but large surface clusters. A possible route to reduce the number of large iron clusters could be to anneal the film in between several very small exposures to iron. The energetically less favorable position Fe^O that is responsible for cluster formation is expected to be changed to the more stable Fe^x position. Another possibility would be to remove the clusters directly with mild sputtering or ozone treatment.

4.5.3 Magnetic Properties of Fe-Atoms in the Silica Film

The morphological and energetical properties of the investigated Fe/silica system seem favorable as described in the previous section for several reasons: 1. the iron atoms remain monomers in most cases since clustering is favorable only for about a tenth of all adsorption sites. 2. the iron atoms are strongly bound at the interface and do not diffuse or agglomerate even at temperatures above room temperature and 3. they are protected from unwanted reactions in the inert silica matrix.

Yet it is clear that any potential use of the iron atom ensemble as magnetic device requires the conservation of the iron magnetic moment, therefore the magnetic proper-

ties of the subsurface iron atoms are of great interest. The experimental setup used for this thesis does not permit direct magnetic measurements, since no external magnetic field could be applied. However, the mere existence of an uncompensated iron spin can be concluded from perturbations of the silica/Mo(112) electronic structure. The physics behind this phenomenon has first been described in 1964 by Jun Kondo and is thus called Kondo effect [145]. The Kondo effect describes the scattering of conduction electrons of a metal at a magnetic impurity. This effect was first described for magnetic impurities in a gold sample. For the case of iron in silica/Mo(112) a hybrid state between the localized Fe *3d*-states, that carry the magnetic moment, and the *sp*-state continuum of the molybdenum is formed.
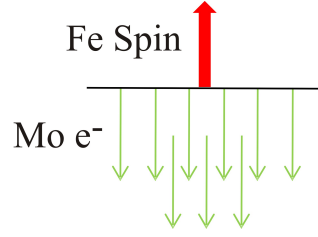

Figure 4.20: Simplified representation of the spin-screening of the iron spin-impurity by the molybdenum electrons. The resulting hybrid state leads to an electronic many-body system called the Kondo resonance.

The resulting many-body state, referred to as Kondo resonance, screens the iron magnetic moment by an antiparallel spin alignment of the Mo conduction electrons. This is schematically depicted in figure 4.20. The Kondo resonance is located at the Fermi level of the diluted magnetic system and gives rise to distinct Fano-type conductance spectra in STS measurements [146, 147].

The Fano shape hereby originates from quantum interference effects between a direct tunneling path between tip and sample and an indirect one that involves the Kondo resonance. From the width of the Fano line the Kondo temperature is determined as the critical temperature below which the formation of the many-body electronic state occurs [141, 148, 149].

Conductance spectra of both Fe^O and Fe^x atoms at the silica/Mo(112) interface exhibit indeed a characteristic zero-bias anomaly that is not observed on the pristine film. The corresponding spectrum is shown in figure 4.21 a. This conductance anomaly is spatially localized at the interfacial iron atoms as demonstrated with differential conductance images taken slightly below the Fermi level which are shown in figure 4.21 c. The observed conductance behavior is compatible with the Kondo effect, although other explanations cannot be excluded, such as an iron-induced change of the single-electron LDOS. Subtraction of the silica background from the iron spectrum yields a strongly asymmetric line that can be fitted to the Fano model [150]:

$$dI/dV \propto (q + \epsilon')^2 / (1 + \epsilon'^2) \quad with \quad \epsilon' = (\epsilon - \alpha)/(kT_K) \tag{4.3}$$
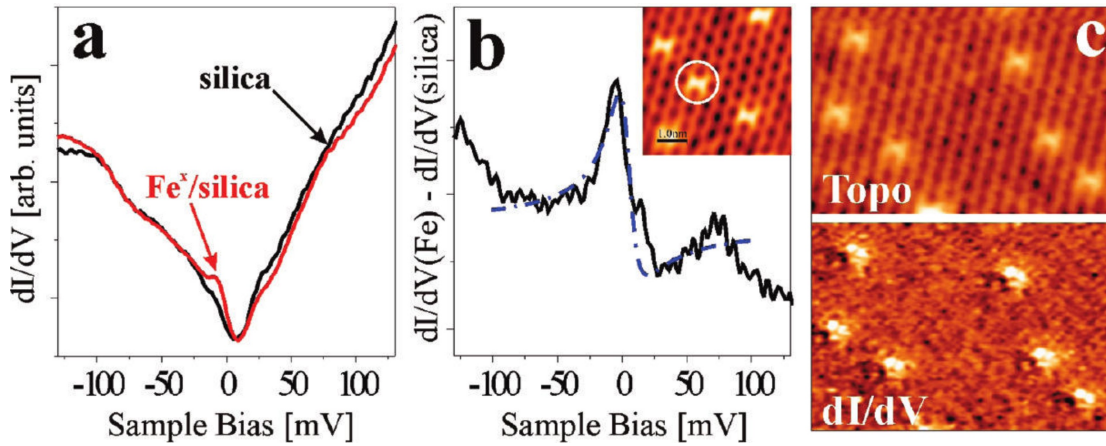
Figure 4.21: (a) Differential conductance spectra of the bare silica/Mo film (black) and a subsurface Fe_x species (red) (bias set point for spectroscopy: 125 mV). The probed atom is marked by a circle in the inset (5 x 5 nm^2). The Fe induces an additional spectral component at the Fermi level. (b) Difference between the Fe^x and the silica/Mo conductance curve. The resulting peak at the Fermi level is fitted with the Fano model (dashed line). (c) Topographic and corresponding conductance image of Fe^x species in the silica/Mo film, taken at a bias position close to the peak maximum in the dI/dV spectrum (U_s = -20 mV, 9 x 6 nm^2). The dI/dV map visualizes the strong localization of the conductance anomaly around the embedded Fe atoms.

Hereby, α corresponds to the energy position of the Kondo resonance and q is the asymmetry parameter that accounts for the coupling between the localized state and the tip wave function.

A satisfactory reproduction of the experimental data is obtained for a Kondo temperature T_K of 122 ± 10 K and a resonance position α of -6 ± 1 mV as indicated in figure 4.21 b with the dashed line. Similar T_K values have been obtained for magnetic adatoms on nonmagnetic substrates, for example, for Co on Ag(111) (92 K, [149]) and Au(111) (70 K, [147]), supporting the Kondo nature of the observed zero-bias anomaly. However, an unambiguous experimental proof cannot be given because this would require conductance measurements performed at different magnetic fields and temperatures. Preliminary results from highly resolved photoemission experiments performed with synchrotron radiation support the idea that the iron atoms indeed retain a magnetic moment and a Kondo impurity may be observed close to the Fermi edge [151]. This possibility will be addressed in the outlook at the end of this thesis.

Beyond the experimental evidence also DFT calculations are in correspondence with the Kondo scenario. A magnetic moment of 1.35 and 2.15 μ_B is calculated for the Fe^x and Fe^O species respectively. Apparently, the magnetic moment of gas phase iron atoms of 4 μ_B is reduced but not completely quenched upon adsorption at the silica/Mo(112) interface. Both, experiment and theory, therefore indicate a magnetic nature of the embedded iron atoms, which is a crucial requirement for using the porous silica film as a template to fabricate single-atom magnetic units.

4.6 Conclusions

This chapter of the thesis represents the experimental side of a joint theoretical and experimental approach to understand possible modifications of the adsorption behavior of oxide films. It could be demonstrated that a monolayer thick, crystalline silica film grown on a Mo(112) single crystal is a suitable system to tailor its chemical and physical properties. Local modification possibilities for this film had been proposed before. It was shown that incorporated palladium or silver atoms act as surface anchors for other species such as gold. This has been proven to be a possibility to locally modify the adsorption properties of this film.

In this thesis, lithium was chosen as a promising candidate to globally modify the film properties because of its special electronic properties and its ability to bind at the silica/Mo(112) interface. The special adsorption properties of lithium at the interface between the silica film and molybdenum are discussed and a distinct stripe pattern was discovered and explained in terms of the screening response of the molybdenum.

Positively charged lithium atoms at the interface between metal and oxide films lead to a strong positive dipole and thus to a reduction of the work function. This renders the modified film reactive in the sense that adsorption and charging of gold atoms and

small particles becomes possible on the previously inert oxide film. In contrast to the previously described changes in the film, this method represents a possibility to globally modify its characteristics, since the work function is a global film property. The ensuing adsorption mechanism is related to a charge transfer from the metal into the gold atoms, which initiates a polaronic distortion of the oxide lattice. The strongly bound Au^- species constitute the seeds for further cluster growth. The stabilization of charged adspecies is of particular interest not only because of the enhanced binding but also because of their particular catalytic and morphological properties. For example, charged adspecies tend to form smaller aggregates on a surface due to their repulsion. This might lead to an enhanced catalytic activity. Furthermore, charged adspecies display different chemical activity than their neutral counterparts making them the desired promoters in some catalytic reactions. With the incorporation of lithium, a general route towards tailor-made adsorption properties of thin oxide films has been demonstrated that might be applied to other systems as well.

Beyond the tailoring of the chemical, i.e. the adsorption properties, it has been shown that the silica/Mo(112) film is also a suitable system to tailor its physical properties by stabilizing monomeric iron species at the metal-oxide interface. The iron atoms are found to penetrate the openings in the silica surface and occupy high-energy binding sites at the metal-oxide interface. In these positions, the iron atoms are stabilized and cannot diffuse or agglomerate even at temperatures above 300 K. They are also well-protected against environmental influences due to the inert nature of the oxide layer above. Yet, the magnetic character of the interfacial iron atoms is preserved. The iron penetration into the silica pores competes with the formation of few but large surface clusters, especially at high iron exposure. The clusters will produce an unwanted signal that interferes with the magnetic response of the monomeric magnetic entities. However, a possible route to reduce this unwanted effect might be to remove metallic iron clusters from the surface by etching, mild sputtering, or ozone treatment. The demonstrated incorporation of iron into the nano-pores of a silica/Mo(112) film is therefore a promising route to stabilize dense ensembles of atom-sized magnetic units that do not require operation at cryogenic temperature.

5 Ceria thin films grown on Ru(0001) - Structural and Electronic Properties

Having dealt with an inert oxide material that can act as a passive support for active metal species in the first part of this thesis, the second part deals with ceria (CeO_2), which is an active support for catalytically active metal particles in heterogeneous catalysis. Ceria is an interesting material for various industrial and scientific applications and has therefore received considerable attention in the scientific community over the last decades. This is shown in figure 5.1 where the number of published scientific articles with the topic ceria is plotted over the years. A growing interest in the scientific community is clearly visible from the almost exponential growth of the number of papers published per year. This is not surprising since ceria displays promising properties for various applications, for example as a buffer layer material to support high-temperature super-conductors [152]. Ceria films also have potential applications as single- and multilayer optical coatings [153], as gate insulator material for metal-oxide-semiconductor transistors [154], in metal-insulator-metal devices [155], in silicon-on-insulator structures and capacitor devices [156], as UV-rejecting films to prevent degradation of polymer materials exposed to strong daylight [157] and as oxygen gas sensors [158, 159]. Furthermore, it has promising potential uses in fuel-cell technology [160].
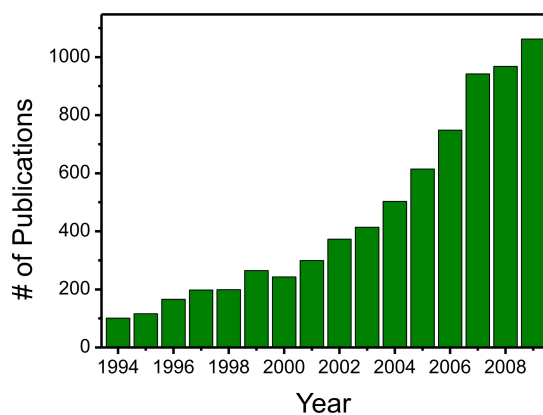

Figure 5.1: The number of scientific articles published on ceria has been growing almost exponentially in the last years. This graphic shows the number of results when looking for papers with the topic "ceria" in ISI Web of Knowledge [161].

Beyond that, ceria is also one of the most common oxide supports in heterogeneous catalysis and used in several commercially relevant processes, e.g. water-gas-shift and NO_x-reduction [162–164]. The outstanding performance of ceria as catalyst support relies to a large extent on its easy reducibility and the resulting ability to release lattice oxygen that in turn promotes oxidation processes [165, 166]. The reduction is accompanied by the formation of two Ce^{3+} defects for each released oxygen atom due to an electron transfer out of the vacancy. The excess electrons become trapped in initially empty Ce $4f$-states that consequently shift below the Fermi-level (E_F) and form a localized $^2F_{5/2,7/2}$ resonance in the band gap. The oxygen vacancies are easily healed again in oxygen-rich conditions, rendering the ceria system perfectly suited to balance the oxygen supply during a chemical reaction. The reversible reduction/re-oxidation of the oxide is possible thanks to the relatively small energy difference between Ce^{4+} and Ce^{3+} ions in the ceria lattice [167, 168].

In this thesis the STM has been used to study different properties of ceria. One of the main focuses is the electron localization upon defect creation which is an intensively discussed topic. But also the morphology and electronic structure of ceria thin films and various defect types are discussed in the following sections.

5.1 Morphological Properties of Ceria Thin Films Grown on Ruthenium (0001)

Cerium is a rare earth metal and belongs to the series of the lanthanides. In the presence of oxygen it is oxidized to Ce_xO_y. Known phases include Ce_2O_3, Ce_3O_4 and CeO_2. Ceria films have been grown on various substrate materials. Amorphous ceria has been grown on Si [169–171], Ge [172], $LaAlO_3$ [173], Au [173], Pd [173, 174], Al_2O_3 [173, 175], Ni [176], $SrTiO_3$ [177] and Pt [178]. For the more demanding case of crystalline ceria films the known substrate materials are Ni(111) and Ru(0001) [179], Rh(0001) [180, 181], Pt(111) [178, 182], Pd(111) [174], Cu(111) [183] and Cu_3Au(111) [184]. While ceria grows in a crystalline way on all those substrates the quality, patch sizes and annealing temperatures are quite different for the films on different substrates. For this thesis a ruthenium single crystal exposing the (0001) surface has been chosen as substrate material for the ceria film growth.

5.1.1 Preparation and Thickness Dependent Morphology of Ceria Thin Films Grown on a Ru(0001) Single Crystal

The original recipe suggested by Mullins *et al*. [179] for a CeO_2 thin film on Ru(0001) was improved by Lu *et al*. by changing some preparation parameters [185]. Still, it turns out that the film does not grow in a perfect manner. Only small to medium sized patches below 100 x 100 nm^2 of ceria are observed in the STM images. This is at least in part due to the rather large lattice mismatch between bulk ceria (lattice constant a

= 3.9 Å) and the Ru(0001) surface (a = 2.7 Å) of 44%. This lattice mismatch leads to a minimization of the interface area between the ruthenium support and the ceria film at high temperatures and thus to Volmer-Weber like growth of three-dimensional particles [186]. Another consequence of the lattice mismatch is the appearance of a Moiré pattern. This phenomenon is discussed in more detail in section 5.1.2.
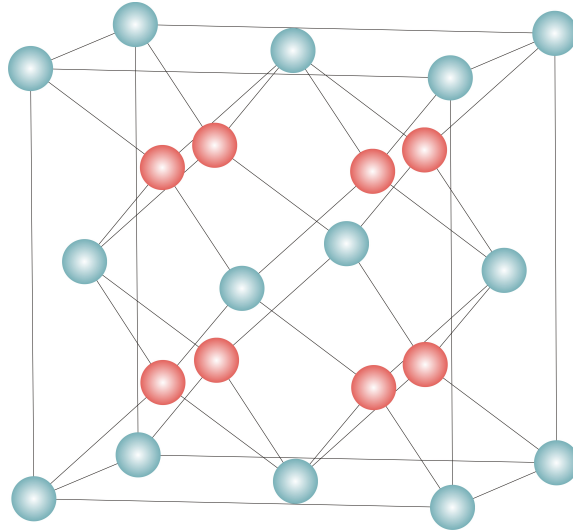

Figure 5.2: Model of the fluorite crystal structure of ceria. The red and blue balls depict the positions of oxygen and cerium atoms respectively.

Ceria (CeO_2) that has been investigated in this thesis forms a fluorite crystalline structure like CaF_2 as shown in figure 5.2 and [162]. The stability of the low index surfaces of CeO_2 decreases in the order (111) > (110) > (100) [187, 188]. In this thesis the most stable surface, the (111)-surface has been investigated. A ball model of the hexagonal (111)-surface is given in figure 5.3. Ceria is easily reduced at high temperatures or in a reducing gas environment. This reduction leads to the creation of oxygen vacancies, yet the crystal structure is hardly affected. The formal oxidation state of cerium and oxygen ions in stoichiometric ceria is 4^+ and 2^- respectively. In the vicinity of an oxygen vacancy two cerium ions change their oxidation state to 3^+ in order to accommodate the two electrons left behind by removing one neutral oxygen atom. The electronic structure of the ceria film and its defects are addressed in section 5.2 later in this thesis.

The Ru(0001) substrate for the film growth was cleaned by repeated cycles of argon sputtering with an ion energy of 1 keV, oxygen exposure of $\approx$ 1000 L at elevated temperatures (700 K) and UHV annealing to 1500 K. Preoxidation of the ruthenium sample was done at 700 K with an oxygen pressure of 5 x 10^{-7} mbar for 5 minutes. The oxide film was prepared by depositing cerium onto the preoxidized Ru(0001) single crystal surface in 5 x 10^{-7} mbar O_2, whereby 50% of the material was dosed at 150 K and 50%
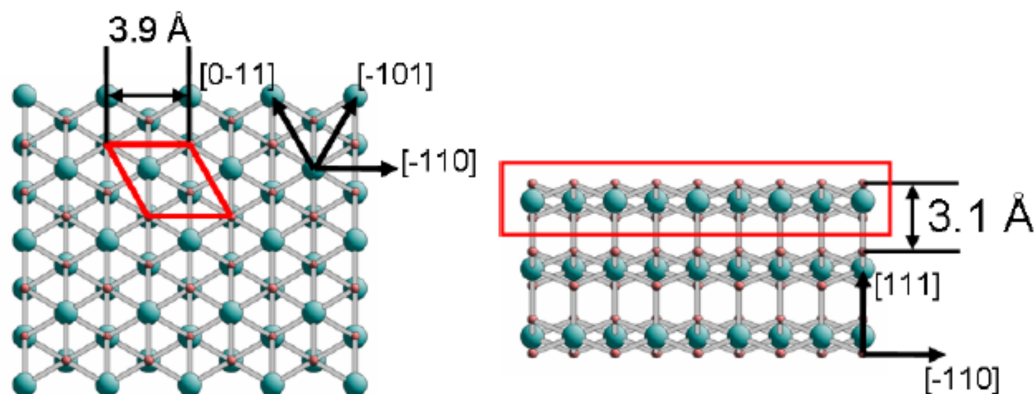
Figure 5.3: Model of the (111) surface of ceria. The red and turquoise balls depict the positions of oxygen and cerium atoms respectively. The unit cell is shown in red on the left side and the O-Ce-O trilayer structure on the right side. Adapted from [184].

at 700 K. Subsequent annealing of the sample to 1100 K led to the ordering of the film, as evident from the sharp hexagonal ($\sqrt{2}$ x $\sqrt{2}$) LEED super structure with respect to the ruthenium (1 x 1) LEED pattern. This is shown in figure 5.5. This superstructure is compatible with a (111) orientation of the CeO_2 lattice [185] and the position of the ceria induced spots corresponds to the expected lattice mismatch of 44% with respect to the ruthenium substrate. The film thickness was varied between one and more than eight O-Ce-O trilayers with each trilayer being 3.1 Å high. An atomistic model of the trilayer structure is given in figure 5.3. For a thickness of up to roughly 5 trilayers the spots of the ruthenium substrate remain visible in the LEED, as shown in figure 5.5 a and b. This is due to the fact that even for preparations of nominally five trilayers thickness there are areas on the sample with a considerably lower coverage. For very thin films (up to 3 trilayers) even the 2 x 2 spots induced by the oxygen superstructure on the ruthenium substrate are visible. This observation is in accordance with STM images that show areas on the sample that are not covered by ceria but only by the oxygen superstructure as shown in figure 5.4 c. For thicker films with nominal coverages above five trilayers only the $\sqrt{2}$ x $\sqrt{2}$ spots of the ceria are visible in LEED, as shown in figure 5.5 c and d. This is also in accordance with STM images that do not show any areas without ceria (see for example figures 5.7 c and 5.12 a). Auger Electron Spectroscopy measurements taken on such samples do not show any ruthenium, which also confirms the absence of uncovered areas on the sample. Such an Auger spectrum is shown in figure 5.6.

Flat, hexagonal oxide patches of 10-50 nm in diameter were observed in the STM images of thin ceria films of up to five trilayers thickness. Examples are shown in the figures 5.4 a and 5.7 a. Atomic resolution was mainly obtained at positive sample bias, which means that electrons from the tip tunnel into unoccupied states of the sample surface. For the case of ceria the empty LDOS mainly consists of cerium-like states,
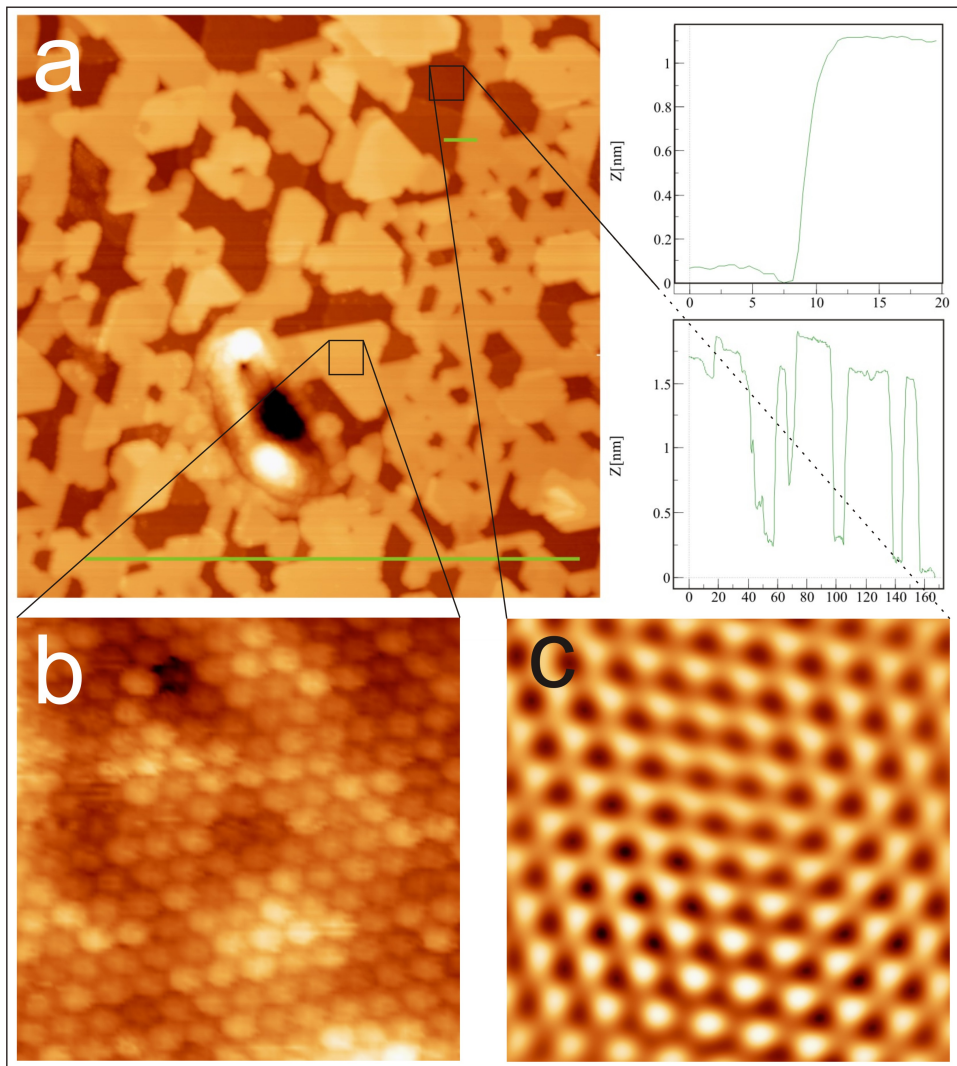
Figure 5.4: (a) STM image of a thin ceria film grown on Ru(0001). The tunneling conditions are U_B = 5.4 V, 170 pA; 200 x 200 nm^2. The height profiles taken across different patches show a height difference between the ceria and the Ru substrate of around 12 Å, which corresponds to a film thickness of four trilayers. The hole in the lower part of the image shows a typical tip crash site. (b) Atomically resolved image of a ceria patch (U_B = 1.2 V, 5 x 5 nm^2). (c) Oxygen 2 x 2 superstructure on the Ru substrate which is clearly observed between the patches (U_B = 0.35 V, 5 x 5 nm^2, this image has been FFT filtered for clarity).
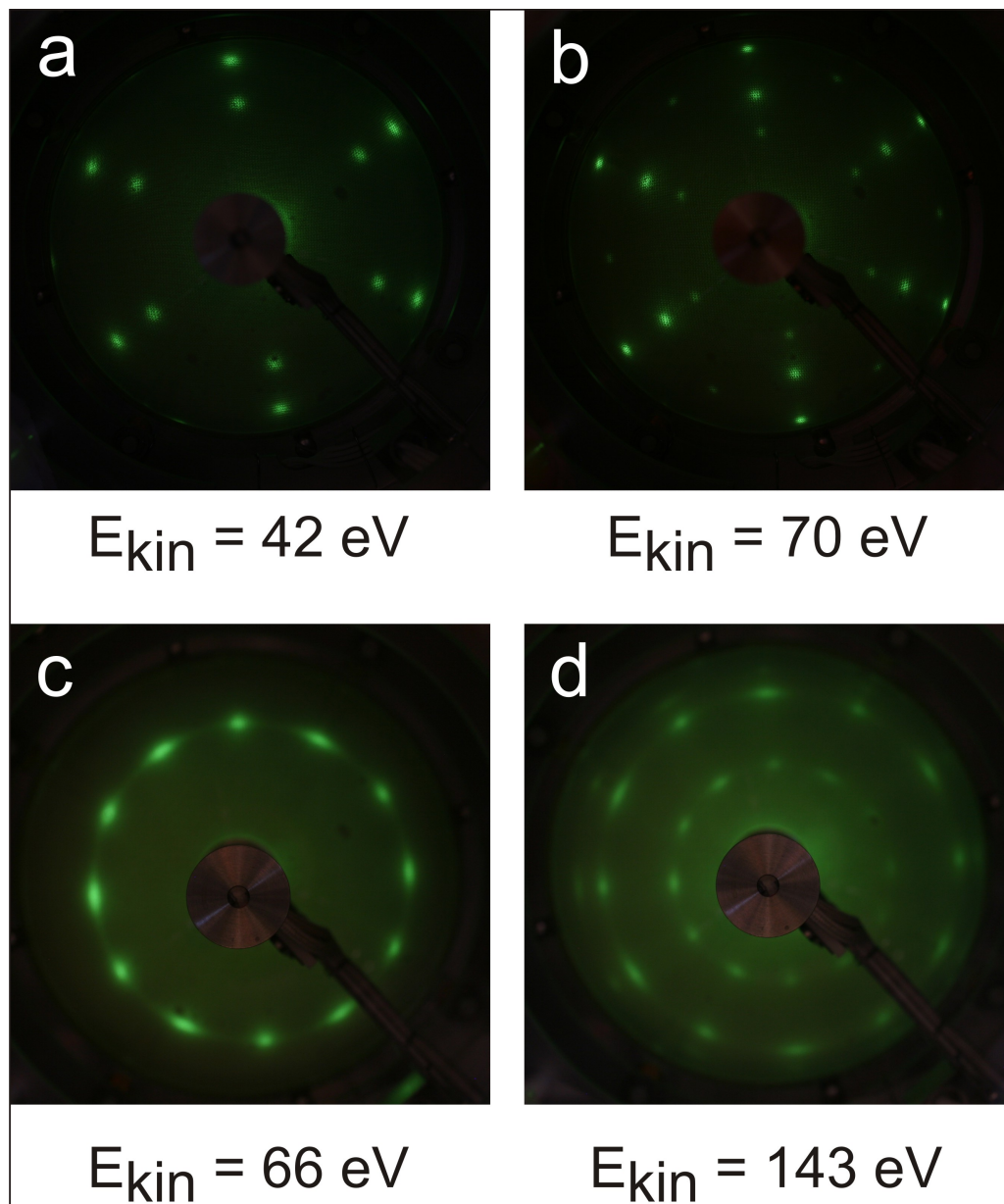
Figure 5.5: LEED pattern of a thin (a-b) and a thick (c-d) ceria film recorded at different electron energies. The ceria spots are clearly visible. For the thin film also the spots of the Ru substrate and the oxygen 2 x 2 superstructure are visible. For the thick film only the spots originating from the ceria film are observed. At this thickness two rotational domains tilted by 30° are visible.
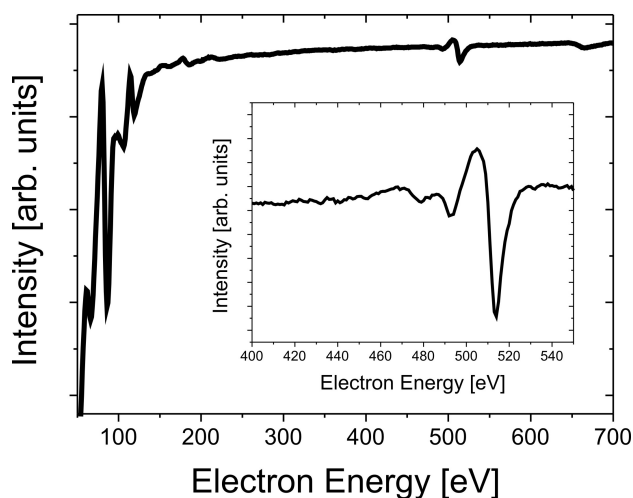
Figure 5.6: Auger spectrum taken from the thick ceria-film. Whereas the peaks for cerium (82 eV) and oxygen (507 eV) are clearly visible, there is no signal from the ruthenium (273 eV) substrate.

therefore the cerium sub-lattice is responsible for the contrast. Accordingly, the lattice visible in figure 5.7 b and d is assigned to the cerium lattice. At negative bias, where electrons from the sample tunnel into the tip, the filled O *2p* orbitals are expected to dominate the image contrast. In both cases, the measured atomic periodicity of 3.9 Å corresponds to the bulk CeO_2 lattice constant. The as-prepared films exhibit only a negligible concentration of point defects.

The thicker ceria films completely cover the ruthenium substrate and larger patches of the oxide-film with a diameter of 20-100 nm are observed. Screw dislocations and anti-phase domain boundaries are clearly visible in the STM images. LEED as well as atomically resolved STM measurements reveal the existence of a second phase of the oxide layer which is rotated by 30° with respect to the ruthenium lattice and the lattice direction of the ultra thin ceria-film. An example is shown in figure 5.12 a-c. This has already been observed for this system by Lu et *al.* [185]. In this work also atomic resolution across the domain boundary is presented. The existence of two phases of the oxide film turned by 30° can be explained by two different rotational domains.

5.1.2 Moiré Pattern of Ultra Thin Ceria Films Grown on Ru(0001)

To analyze the influence of the ruthenium substrate on the ceria film, very thin films (below three trilayers of ceria) have been prepared. Due to the small thickness the coupling to the metal support can be probed even with a surface sensitive method as the STM. Unlike for the case of thicker films the influence of the support is visible at certain tunneling conditions. Figure 5.4 shows such a thin ceria film imaged at high
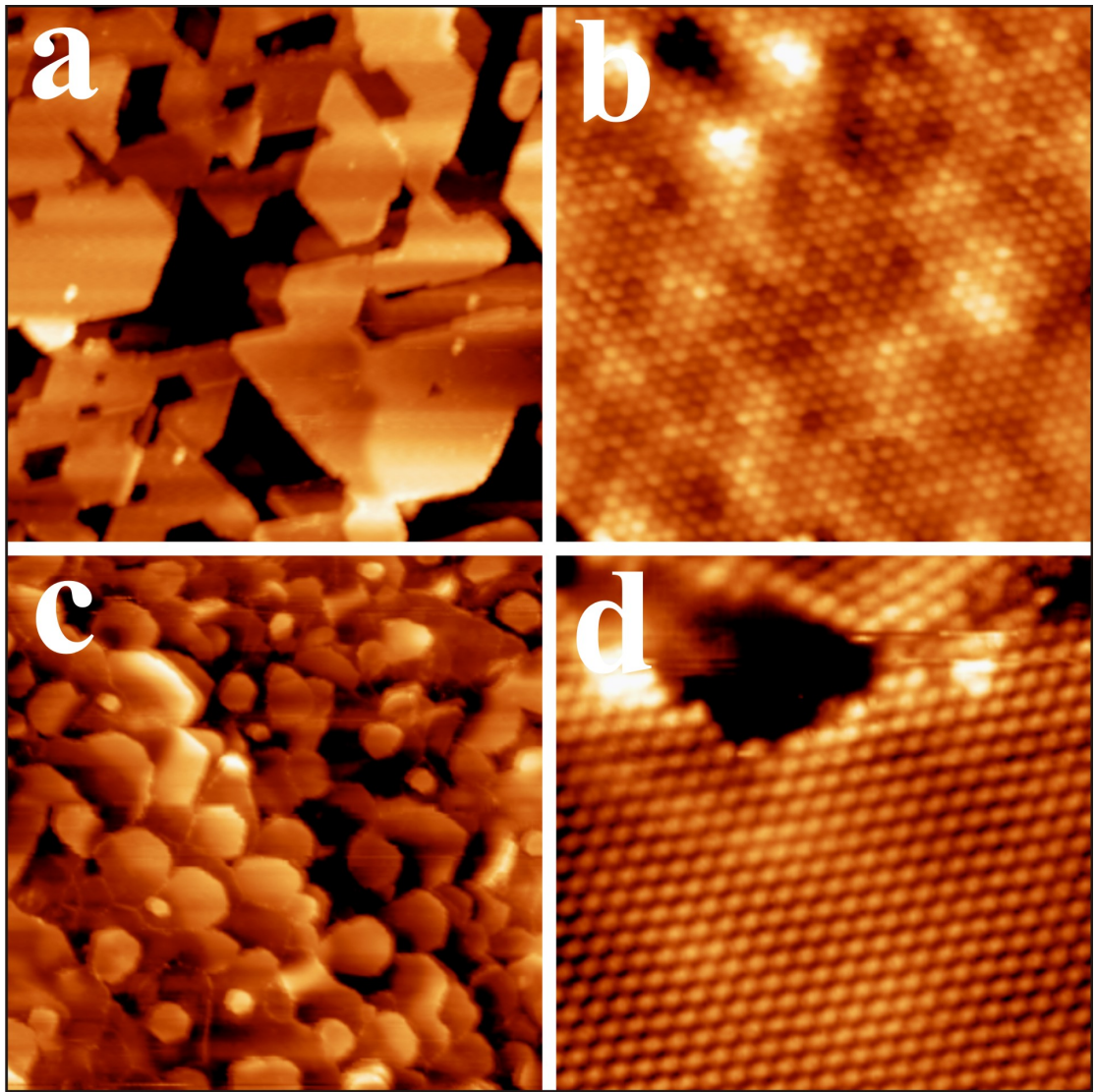
Figure 5.7: STM topographic images of two different CeO$_2$ films grown on Ru(0001). (a) Three to four trilayer-thick film (3.1 V, 100 x 100 nm^2). (b) Atomically-resolved image showing the Ce sublattice of (a) (1.2 V, 12 x 12 nm^2). The paired protrusions in the upper part of the image are assigned to oxygen vacancies. (c) Five to seven trilayer-thick film (4.0 V, 200 x 200 nm^2). (d) Atomically-resolved image showing the Ce sublattice of (c) (1.9 V, 9 x 9 nm^2)

positive bias (5.4 V). The ruthenium substrate is still visible between the patches of ceria.

Due to the lattice mismatch between the ceria-film and the Ru(0001) substrate a characteristic Moiré pattern may be observed [189, 190]. The term Moiré pattern describes an interference pattern that arises when two grids with slightly different lattice constant or angle are superimposed. Moiré patterns have been observed in different ares of physics and technical applications, see among many others for example [191]. Also in STM studies Moiré patterns are a well known phenomenon [130, 192].

On images of the ceria film taken at bias voltages below 2 V, a regular structure of bright and dark triangles becomes visible. The apparent height difference between the higher and lower triangles is only about 50 pm yet it is clearly resolved in the STM images. All the bright triangles are oriented in the same direction and all the dark ones in the opposite direction. As seen in figure 5.8, all those triangles consist of four atoms along each side. A fifth one is not resolved in the image but could be localized just in between two adjacent triangles. Since the images are taken at positive sample bias the electrons flow from the tip into the empty states of the ceria film. These empty states are formed mainly by Ce f,d-states coupled to the empty metal states. Therefore it is assumed that the bright protrusions in the STM images correspond to the cerium lattice positions whereas the dark spots correspond to the oxygen positions. Considering the fact that each ceria trilayer is oxygen terminated, this means that the STM is not imaging the outmost atomic layer but the cerium layer in the middle of the trilayer structure. This assumption is also supported by DFT-calculations performed for ceria grown on a rhodium (111) single crystal surface [193] and for STM images of a ceria single crystal taken at elevated temperatures [194].

Considering the lattice mismatch of 44% between the Ru(0001) lattice (a = 2.7 Å) and the bulk ceria lattice (a = 3.9 Å), a periodic superstructure of 7 ruthenium atoms coinciding with 5 cerium atoms could be assigned to the observed Moiré structure. The according model is presented in figure 5.9. It was first proposed by Castellarin-Cudia *et al.* for ceria on rhodium [193] and by Lu *et al.* for ceria on ruthenium [185]. In this work atomic resolution and an atomic model of the Moiré structure is reported giving further insight into the surface structure.

The 7_{Ru} x 5_{Ce} superstructure yields a periodicity of 19 ± 1 Å which is in good agreement with the experimentally observed value as shown in figure 5.8 and the previously reported results [185]. Figure 5.9 shows the proposed structure with the blue and red balls representing the cerium and ruthenium atoms respectively. For clarity the oxygen atoms have been omitted and the bright and dark triangles marked with black and green triangles respectively in figure 5.9. Without any lattice distortion or turning, which would be in contradiction to the LEED measurements, the observed triangle structure can be reproduced. It turns out that indeed for the bright triangles the cerium atoms mostly sit on top or very close to substrate ruthenium atoms whereas for the dark triangles the cerium atoms mostly sit in bridge or hollow sites. Even the fact that in the STM images every bright triangle displays a darker atom in the center, may be explained in the framework of the proposed model: in the middle of each bright triangle one cerium atom is placed in, or very close to, a ruthenium hollow position, which
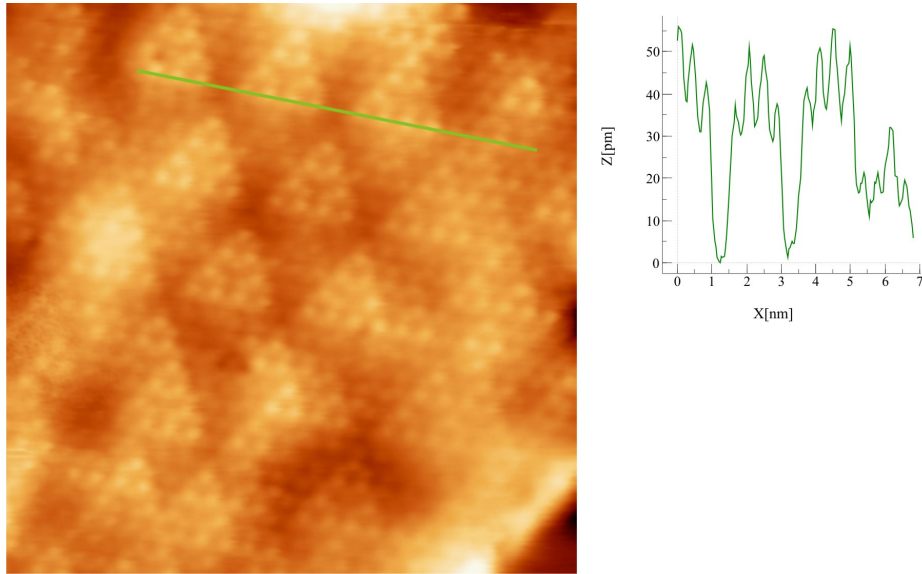
Figure 5.8: 10 x 10 nm^2 STM image of a thin ceria film taken at U_B = 1.2 V. The image clearly shows a Moiré pattern. The height profile reveals the small apparent corrugation of only about 50 pm. The triangles consist of 4 cerium atoms along each side.

triggers a lower contrast.

In principle Moiré super structures can have both, a topographic or an electronic origin. In this sense the STM can not easily distinguish if the bright atoms really stick out of the surface or if they are associated with a higher local density of states at the probed bias. Even the fact that the Moiré pattern has been observed at different tunneling voltages does not yield a final answer because an enhanced overlap with the continuous metal DOS of the substrate would make the cerium atoms appear brighter at different energies. However, it is assumed that the cerium atoms sitting on top of a surface ruthenium atom appear brighter in the STM images whereas the cerium atoms closer to bridge or hollow sites display a weaker contrast in STM. This assumption seems reasonable because Ru-Ce mixed states could provide effective pathways for the electrons tunneling from the tip to the sample. This explanation remains plausible even though the cerium atoms are in the middle of the trilayer structure of the ceria. This means that they are neither directly above the surface ruthenium atoms nor at the surface where the tip is probing the structure. It should be noted that the proposed model would also work if the opposite were true and the enhanced contrast appears for oxygen atoms sitting on ruthenium top sites. However, in this case best contrast would be expected at negative sample bias due to the filled character of O-Ru mixed states. The Moiré pattern has not been observed for negative tunneling bias. In principle also a second, topographically driven, scenario is possible where cerium atoms appear brighter whenever three neighboring oxygen atoms in the layer below sit in ruthenium top sites. This
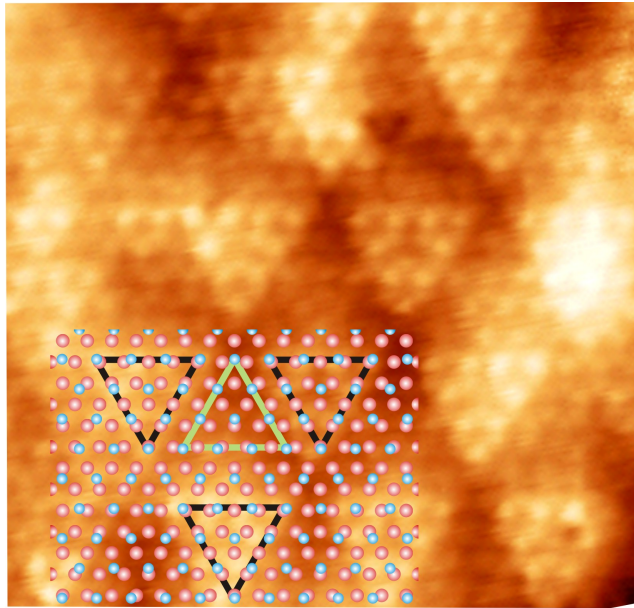
Figure 5.9: Atomistic model of the Moiré pattern formed by the superposition of the Ru(0001) and the ceria(111) lattice put on top of a STM image. The blue and red balls depict the Ce and Ru atoms respectively. For the brighter triangles (marked in black) the Ce atoms mostly sit on top or very close to ruthenium atoms. One atom in the middle of each bright triangle appears dark and is indeed found to sit in a hollow position. For darker triangles (marked in green) most Ce atoms occupy bridge or hollow sites. The underlying STM image has a size of 8 x 8 nm^2 and was taken with U_B = 1.5 V.

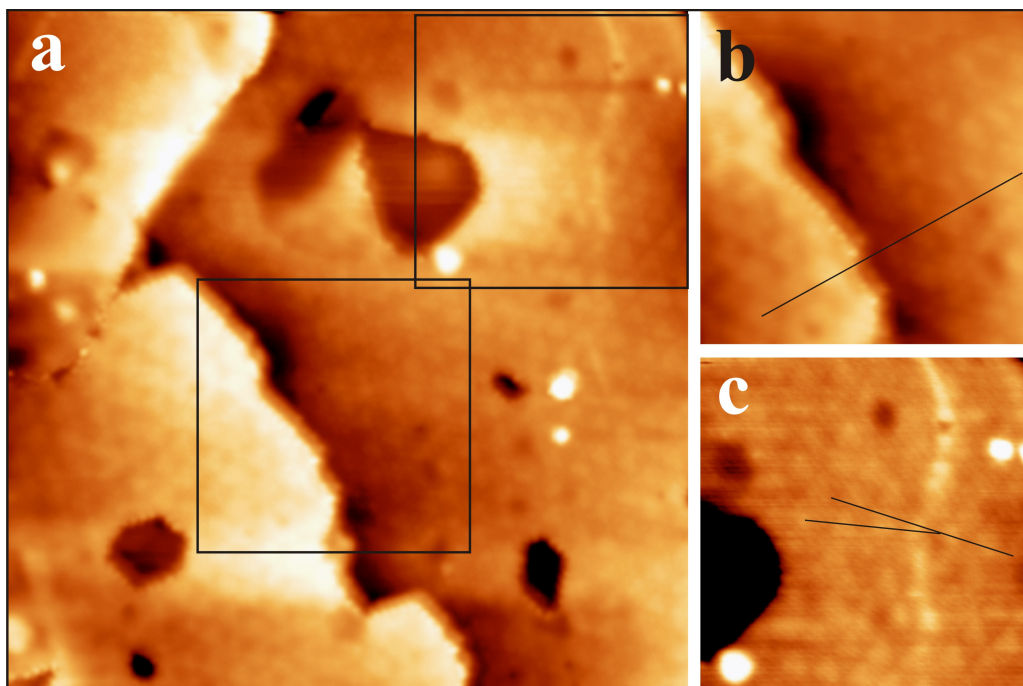would lead to an uplifting of the cerium atoms by the oxygen ligands.

Figure 5.10: The Moiré pattern can be observed across step edges and anti phase domain boundaries. The observations support the assumption that the cerium lattice is imaged at positive sample bias. (a) overview image showing the pattern across both defect types (50 x 50 nm^2; U_B = 3.0 V). (b) Zoom-in showing the pattern across a step edge (20 x 20 nm^2; U_B = 3.0 V). (c) Zoom-in showing the pattern across a APDB (20 x 20 nm^2; U_B = 3.0 V).

On larger images the Moiré pattern has also been observed across step edges and rotational domain boundaries, as shown in figure 5.10. This is not surprising because the Moiré super structure is a property of the thin film and expected for all different domains.

The Moiré pattern continues without tilt or phase shift across step edges, as shown in the zoom-in image 5.10 b. This fits to the fact that the two terraces are of the same orientation and registry, and only differ in their height by one step of the ruthenium surface. When going across a rotational domain boundary, the Moiré pattern seems to follow the 30° tilt of the ceria lattice, as derived from image 5.10 c.

5.1.3 Morphology of Point and Line Defects

As mentioned in the introduction, the properties of defects in the ceria system are of special interest because of their suspected crucial role in catalysis. Therefore special attention has been devoted to defects in this thesis. First an overview over the morpho-

logical properties of different defect types is given before their electronic properties are addressed in section 5.2.

Point Defects

It is well established that the ceria film may easily be reduced and reoxidized, as described in [195] and many other studies. There are several different ways to globally reduce the ceria film. It is well known that irradiation with high energy photons, for example in a synchrotron experiment, leads to a reduction of the film [196]. Other possibilities include bombardment with Ar^+ ions [165], exposure to a reducing H_2 atmosphere [165], vacuum annealing [197] and electron bombardment [198]. For the creation of single surface defects electron bombardment is a well adjustable and therefore suitable method.
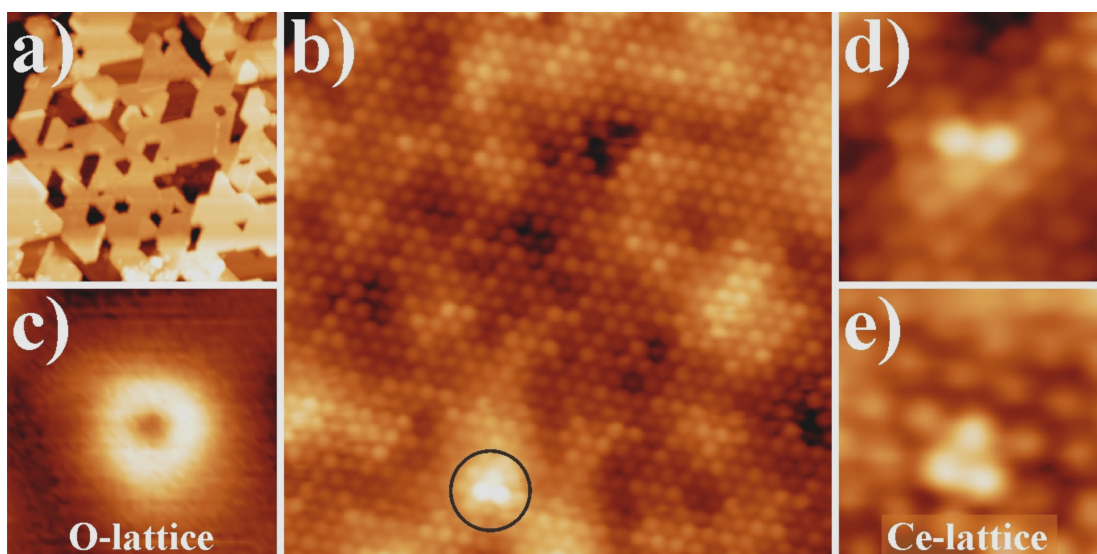

Figure 5.11: (a) STM image of a five trilayer thick CeO_2 film grown on Ru(0001) (3.1 V, 100 x 100 nm^2). (b) Atomically-resolved image showing the Ce sublattice (1.2 V, 12 x 12 nm^2). The protrusion in the lower part is assigned to a single oxygen vacancy. Similar defects imaged with a tip configuration that is sensitive to (c) the O lattice (-1.2 V) and (d, e) to the Ce lattice (2.4 x 2.4 nm^2). While two protrusions are observed at the defect site in (d), three emerge in (e).

The films that are prepared according to the recipe given in section 5.1.1 show a very low defect concentration in STM images. In order to get a measurable concentration of point defects the sample is bombarded with electrons at an energy of 50 eV and a dosage of 10 mC. Electrons at this energy are expected to mainly create surface defects in the top most oxygen layer. In subsequently recorded atomically resolved STM images oxygen vacancies show up as two or three protruding cerium atoms with a height of around 0.6 Å . As discussed later, in section 5.2.2 those protrusions can be interpreted

as Ce 4^+ ions sitting in positions next to the defect. At negative bias, a faint depression surrounded by a ring was observed, reflecting the missing oxygen atom and the relaxation of the neighboring oxygen ions. Those observations are summarized in figure 5.11. Both STM contrast regimes have been observed in an earlier high-temperature study of a CeO_2 (111) single crystal, and assigned to surface oxygen-vacancies with the help of theoretical calculations [194]. In contrast to the results presented here, atomic resolution was obtained at negative tunneling bias and thus the oxygen sub-lattice was resolved in that study. It should be noted that details of the imaging mode strongly depend on the tip state and the possible tunneling channels, which may differ significantly at cryogenic and elevated temperatures. Besides surface oxygen vacancies, no other point defects were observed in the films prepared for this thesis and in particular subsurface defects were not detected, even though they are readily observed in bulk ceria samples [194, 199].

Line Defects

On atomically flat ceria films grown on Ru(0001) step edges and line defects are readily observed. In order to understand the global properties of this system, especially with respect to its catalytic behavior, a detailed understanding of the morphological and electronic properties of those defects is paramount. It is reasonable to assume that step edges and line defects contribute a significant part to the catalytic properties of the ceria system when used in real catalytic applications.

In this section the morphological properties of steps and line defects are presented, whereas the electronic properties shall be addressed later, in section 5.2.5. Figure 5.12 a is an overview image of a typical thick ceria film grown on Ru(0001). Unlike for the case of the thin film no substrate surface is exposed. Two rotational domains separated by rotational domain boundaries (RDB) can be resolved in thicker films. Some RDB are marked with green squares in figure 5.12 a. LEED images confirm both, the presence of two rotational domains and the absence of the ruthenium lattice at the surface. Figure 5.12 b shows such a LEED image where the 12 spots of the two hexagonal domains rotated by 30° are clearly visible, whereas no spots from the ruthenium substrate appear.

Previous studies already showed that the ceria film exposes two rotational domains tilted by 30°. This might be explained by the Volmer-Weber type growth mode of ceria on Ru(0001) where three-dimensional ceria islands are weakly coupled to the metal substrate and can therefore grow rather independently [185, 186, 189]. At the position where the two domains intersect an irregularly shaped protruding line is observed in STM images. The nature of these lines can be understood as the intersection of two stacking domains, which are electronically identical but form a defect line at their interface. Atomic resolution across such a boundary line is shown in figure 5.12 c.

Another type of defect that is observed for some thicker ceria films are screw dis-

locations, as shown in figure 5.13 a, where some are marked with blue circles. Screw dislocations also constitute a well known means for oxide films to release lateral strain that originates from the coalescence of adjacent oxide islands during growth [200].

The step edges that separate large ceria terraces all display a rather round shape which might be assigned to a higher defect concentration at those edges and a limited surface diffusion at the preparation temperatures. Details of step edge orientation are addressed in the next section.
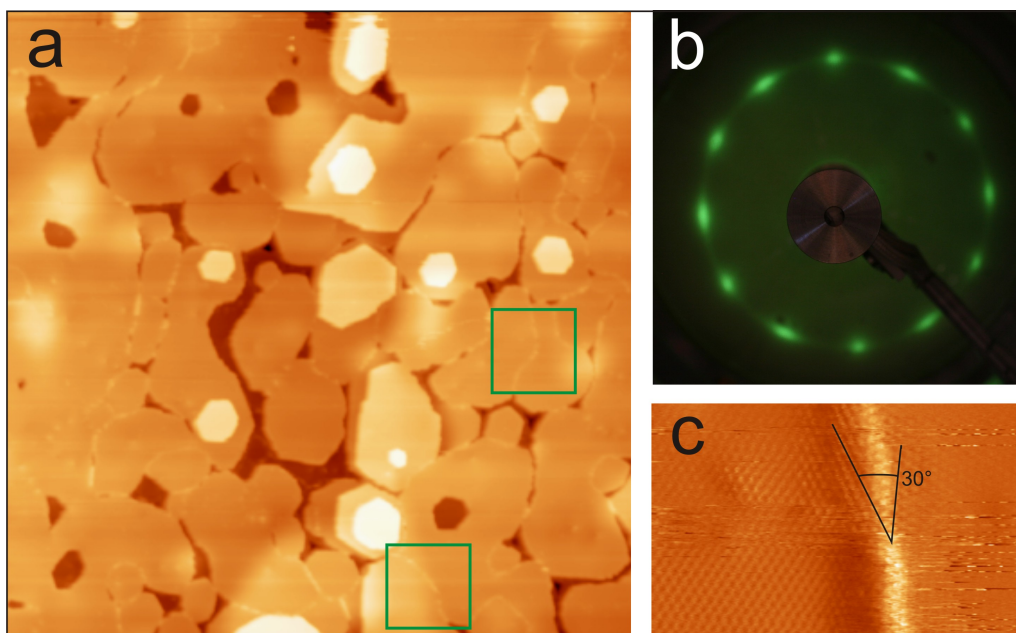

Figure 5.12: Thick ceria film: (a) STM overview image (U_B = 3.5 V, 250 x 250 nm^2), (b) corresponding LEED image (energy is 66 eV) and (c) atomically resolved domain boundary structure.

5.1.4 Islands on the Ceria Film

Typical images of the ceria film display large, flat terraces but in most cases also feature a significant number of hexagonal, crystalline ceria islands grown on top of the film, as shown in figure 5.13 a. These islands display a height of roughly 3 Å which corresponds to one O-Ce-O trilayer of ceria. This is a hint that the film exposes only the oxygen termination since the removal of single planes in the trilayer should lead to a measurable height difference in the STM images. In all images only height differences of multiples of a complete trilayer are observed.

In most cases the islands have a hexagonal shape but display three longer and three shorter edges, however the length ratio of the six island edges might differ depending on the preparation conditions. Analyzing several dozens preparations of the ceria film
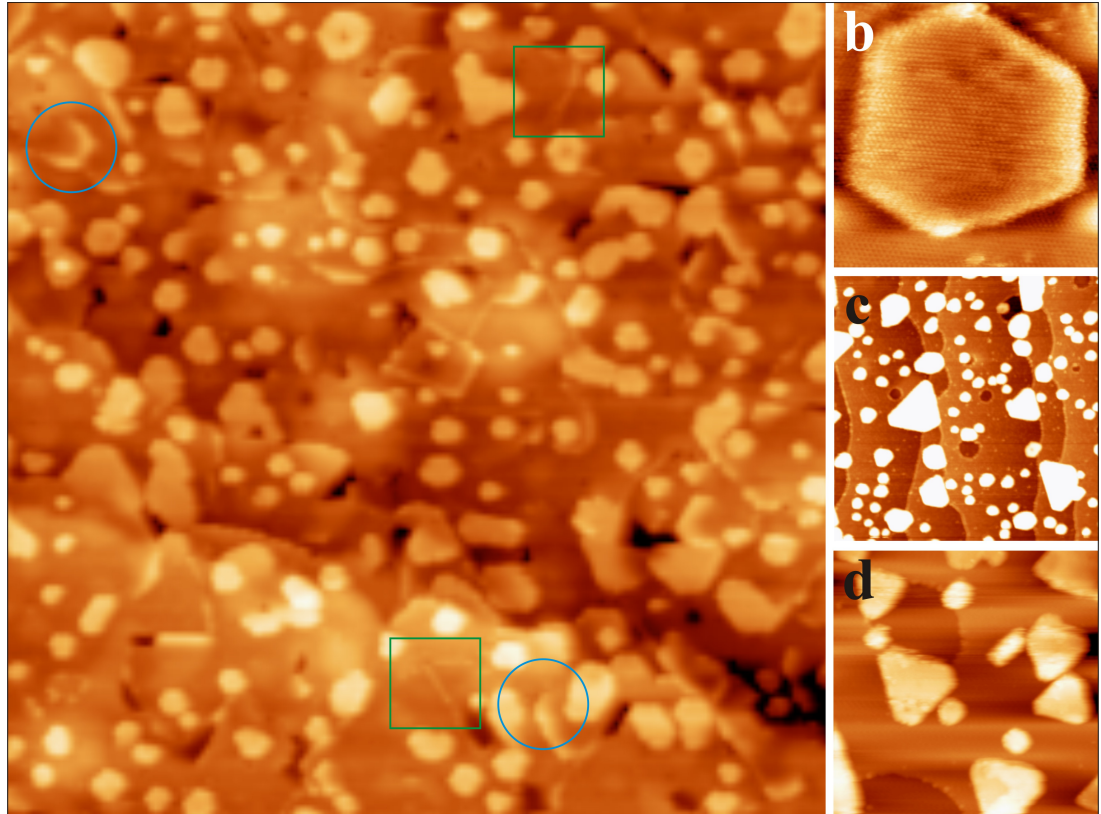
Figure 5.13: (a) Typical large scale overview image of the ceria film (120 x 120 nm^2; U_B = 2.6 V). Several types of line defects and many ceria islands grown on top of the film are visible. Some screw dislocations and rotational boundaries are marked with blue circles and green squares respectively. (b) Atomically resolved image of a ceria island grown on top of the ceria film (20 x 20 nm^2; U_B = 3.0 V). (c) Overview image of triangular shaped ceria islands from a different preparation (200 x 200 nm^2; U_B = 5.0 V). (d) Zoom-in of triangular shaped ceria islands grown on the ceria film (50 x 50 nm^2; U_B = 3.5 V).

reveals that samples that have been annealed to higher temperature (e.g. above 650 °C) tend to display almost evenly hexagonal shaped islands with edges exposing [211] nano facets. An example is shown in figure 5.13 b. Films that have been annealed to lower temperatures display more triangular shaped islands with edges running along the (-101), (0-11) and (01-1) directions. Those steps can be considered as three-layer high nano facets exposing either [110] or [100] nano facets. This is visible in figure 5.13 c and d.

The latter type of islands has been observed before and is known to mirror its orientation going from an ad-island to a pit on the same terrace [184]. This is compatible with the ABC stacking of the oxygen layers known from the ceria single crystal. This implies a reversing of the trilayer orientation when going from one layer to the next.

Analyzing the shape of more triangular ad-islands and pits, the ratio between the long [110] and short [100] related edges has been determined to 1.8 ± 0.1. This length ratio indicates different formation energies of the associated nano facets. According to DFT calculations [187, 188], the formation energy of extended CeO_2 surfaces increases when going from the (111) to the (110) and (100) facet. This sequence is in good agreement with the experimental observation. The film clearly exposes the low-energy (111) facet as surface plane, while edges are formed by long [110] and short [100] nano facets in a two-to-one length ratio. The good structural order of the CeO_2 (111) films shown here demonstrates a preparation close to thermodynamic equilibrium conditions, as expected from the high annealing temperature. The situation described for the thin films differs however from the situation observed for single crystals [201], where ad-islands and pits display a more symmetrical, hexagonal shape with the [110] and the [100] facets being of almost similar length. The difference could be due to kinetic limitations during the surface formation of the ceria single crystal. The edges of this island type also display special electronic properties that are addressed in section 5.2.5 of this thesis.

5.2 Electronic structure of Ceria thin films grown on Ru(0001)

After discussing the morphological properties of ceria films grown on Ru(0001) especially the electronic properties are of great interest in order to shed light on the unique properties of this system. Even though the system has been extensively studied with various spectroscopic methods many questions remain unsolved. Since most spectroscopies average over macroscopic areas of the sample surface especially the local properties require further attention. The STM is a powerful tool for the local analysis of electronic properties of oxide surfaces [5].

Ceria is a wide gap insulator with a bulk band gap of 6.0 eV forming between the occupied oxygen $2p$ states and the empty cerium $5d$ states [202]. However,the band gap of ceria is not featureless. It hosts the strongly localized cerium $4f$ states [198, 203, 204]. The issue of localized cerium $4f$ states in the ceria band gap versus mixed valence states has been a controversial issue for quite some time. One explanation proposed a mixture

of Ce $4f^0$ and $4f^1$ and O $2p$-hole states [205–207] thus claiming the existence of a $4f$ electron even in the ceria ground-state. On the other hand the system can be described with a fully occupied O $2p$ and **empty** Ce $4f$-states in the ground state of ceria with fully coordinated Ce-ions and no reduction [198, 203, 208–211].

The simple application of the octet rule leads one to suspect that cerium is tetravalent and thus CeO_2 an insulator with empty, localized $4f$ states in the band gap as supposed by the second model. This is corroborated by optical reflectivity measurements showing that the occupancy of the Ce $4f$-states is less than 5% for stoichiometric ceria [211]. These empty cerium $4f$-states are found to be located 1.5 eV above the Fermi-level [198].

Still, in the beginnings of the 1980s a big discussion emerged about a possible intermediate valence state of CeO_2 [205, 212–214] and people were supporting the former model because of experimental results from high energy spectroscopies like X-ray photoemission spectroscopy (XPS). XPS measures final f-state configurations and identifies these configurations by their multiplets.

For ceria, a multiple peak structure in XPS experiments due to $4f^0$, $4f^1$ and $4f^2$ derived states in the final configuration is found. This observation led people to claim that also the initial state must have an intermediate valent character. It must be noted that in those experiments the creation of a core hole in an XPS process locally changes the potential of the ion that absorbs the photon and the lesser screened positive core charge is pulling in and lowers the energy of the outer levels. This is especially the case for an empty $4f$ level, the energy of which is lowered towards the Fermi-level and is thus getting partially occupied. Therefore the final states in core level spectroscopies, and only these are measured in a XPS process, will reflect a different situation than in the initial configuration. As a consequence the experimental results can be interpreted as being due to $4f^0$, $4f^1$ and $4f^2$ derived states from which an intermediate valent character has been inferred.

However, Wuilloud *et al.* could show in a bremsstrahlung isochromat spectroscopy (BIS) experiment, i.e. in a non-core level inverse photo electron technique, that the empty $4f^0$ state is about 1.5 eV above E_F [198]. This result is compatible with an empty cerium $4f$-band. cerium .

Thus it could be concluded that stoichiometric ceria is an insulator with empty $4f$ states above E_F lying inside the large band gap of 6 eV between the filled $2p^6$ anion derived valence band and empty $5d$ conduction states.

The situation changes upon reduction of the ceria film. As discussed before, the ceria film can easily be reduced and re-oxidized which explains its outstanding catalytical properties. In the stoichiometric ceria film the cerium and oxygen ions are in a 4^+ and 2^- oxidation state respectively. Upon removal of an oxygen atom two electrons are left which have been found to localize in previously empty cerium $4f$-states. This has been described by Skorodumova *et al.* [168] and is schematically shown in figure 5.14. The exact localization of the electrons is subject to intense theoretical debate. This issue is addressed in section 5.2.2 of this thesis and substantial experimental evidence for the exact whereabouts of the electrons is presented there.

Beyond that, also the special electronic properties at structural defects and the issue
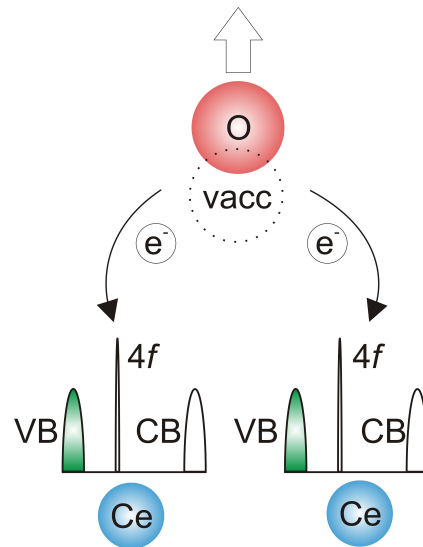
Figure 5.14: Creation of an oxygen vacancy leads to the localization of two electrons in two cerium $4f$ states in the ceria band gap. Those two cerium ions consequently change their charge state from 4^+ to 3^+. Adapted from [168].

of reduced cerium ions at those sites is addressed in subsection 5.2.3. The properties of the globally reduced ceria film are addressed in 5.2.4 while the electronic implications of the different islands forming on the ceria film are discussed in 5.2.5.

5.2.1 Local Electronic Properties of Stoichiometric Ceria Films Grown on Ru(0001)

The large band gap renders the tunneling on this system quite difficult. In order to achieve stable tunneling conditions one has to use high bias voltages, i.e. above +3.0 V or below -3.0 V. Only in special cases with a very good tip a coupling to the f-like states in the band gap is possible and atomically resolved tunneling at lower biases becomes possible. The band gap of the system can to some extend be determined by dI/dV spectroscopy, even though it can not be directly measured [215]. As described in the previous section 5.2 the band gap of stoichiometric ceria is not featureless. It hosts the strongly localized, empty cerium $4f$ states. Tunneling at low, positive bias, well within the known band gap of the film of 6 eV, yields atomic resolution of the oxide film as shown for example in figure 5.7. The contrast is assigned to the lattice of cerium 4^+ ions. Differential conductance spectroscopy measurements reveal indeed empty state density within the band gap. For the flat film the maximum of this density of states is detected at around 2.3 eV above the Fermi-level and at around 2.8 eV when positioning the tip on top of a ceria ad-island. Those empty states are assigned to the unoccupied cerium $4f$-states. In most STM experiments strongly localized d- or f-states do not overlap with the wave function of the tip and thus do not contribute to the

tunneling signal. Only in special cases however, where very localized states lie in the band gap of an insulator, e.g. an oxide, experiments have been reported where those states become accessible to the STM [216] and dominate the contrast in STM images in a certain bias range.

Also in the ceria example reported here the detection of highly localized f-states seems probable for several reasons. First of all, detection of those states is only possible with very small tip-sample distances as is expected for the spatially confined f-states. This is ensured by stabilizing the tip at energies well within the band gap. Furthermore the energy position of the $\frac{dI}{dV}$ peaks fits well to the f-band center measured with EELS and PES [165, 198]. Beyond that, also negative differential resistance (NDR) is observed. This is shown in figure 5.15, where the tip is placed at different positions on the oxide surface. For higher tunneling current NDR is observed (spectrum 1*). For higher setpoints, I $\geq 50pA$, the $\frac{dI}{dV}$ signal becomes negative because the sudden closure of the f-band mediated tunneling path cannot be compensated by the reduced tunneling barrier. Therefore the NDR is observed between the onset of the conduction band and the energy position of the Ce $4f$-states. NDR has been observed before in tunneling spectra of single atoms and molecules when electron transport is limited to spatially and energetically confined orbitals [217, 218].

When taking spectra on top of a ceria ad-island a shift in the energy positions of the f-state induced peak and a broadening of the $\frac{dI}{dV}$ signal is observed. The broadening can be understood in terms of the chemical environment of the involved Ce ions and band bending effects due to the electric field between the tip and the sample surface. While the Ce 4^+ ions in the ultrathin film all occupy similar positions, the situation changes when going to thicker film or to ad-islands where some Ce ions are placed in a bulk-like chemical environment. The convolution of contributions from the different species can lead to a broadening of the observed tunneling spectra. The slight change in energy position might be related to the different influence of band bending when going from a thin to a thicker ceria environment. The percentage of the field-strength that drops in the film rises with increasing film thickness and thus causes a shift of the energetic band positions.

As expected for stoichiometric ceria, $\frac{dI}{dV}$ measurements show no features in the band gap below the Fermi-level. This indicates that no filled cerium f-states can be detected in this case. This situation changes however as the film is locally reduced. The results of $\frac{dI}{dV}$ spectroscopy performed on point defects are discussed in section 5.2.2.

5.2.2 Local Electronic Properties of Single Point Defects in Ceria Grown on Ru(0001)

As described before in section 5.2.1 empty Ce $4f$-states could be detected using $\frac{dI}{dV}$ spectroscopy on the pristine ceria film. Upon oxygen vacancy creation the Ce $4f$-states are expected to partially shift below the Fermi-level and thus become partially filled. This is schematically shown in figure 5.14.

On removing one oxygen atom from the oxide lattice, two electrons are left behind that form two reduced Ce^{3+} species [168]. These electrons occupy split-off states of the
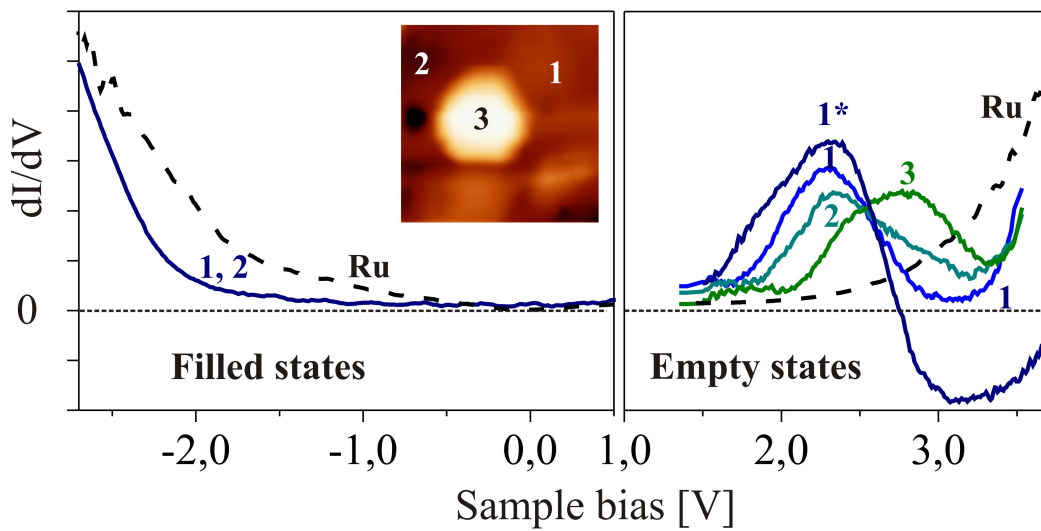
Figure 5.15: Differential conductance spectroscopy on stoichiometric ceria shows empty states in the band gap. The tip positions of the different spectra are marked in the inset (2.0 V, 15 x 15 nm^2). The maximum shifts from 2.3 eV to 2.8 eV when going from the flat film to a ceria island. Spectrum 1* is taken at higher tunneling current and shows negative differential resistance. No filled states are observed in the band gap. Spectra taken on ruthenium are shown for comparison, as expected no band gap is observed for the metal.

originally empty Ce *4f*-band, which lie inside the O2*p*-Ce5*d* band gap of ceria and are highly localized in space.

Since most spectroscopies that have been used to analyze the reduction process of ceria provide only spatially averaged information, the fact that Ce^{3+} ions form is well understood but the spatial localization of this ion pair with respect to the oxygen vacancy is still under debate. A lot of theoretical effort has been made over the last decade in order to grasp the Ce^{3+} positions. While earlier DFT studies concluded that an electron localization in sites adjacent to the vacancy is more favorable [187, 194, 219], more recent DFT results show that the occupation of more distant sites is energetically favored [220–222]. Studies for ceria nanoclusters even found that low-coordinated edge sites are the preferential sites for Ce^{3+} formation, also if the corresponding oxygen vacancy is far away, indicating that the electrons do not necessarily locate in the direct vicinity of the defect [223, 224]. Those DFT results already show the complexity and sensitivity to the claculatory details of this topic.

From the experimental side, STM and AFM have successfully been used to identify surface and subsurface oxygen vacancies in ceria, however no electronic information is reported and thus the electron localization remains unclear [194, 199, 225].

The experiments performed in the framework of this thesis provide clear spectroscopic signatures of filled Ce *4f*-states that could be allocated to nearby oxygen vacancies identified in STM images. With the help of DFT calculations, performed in the group of Prof. Sauer in Berlin, it could be concluded that electrons left behind upon vacancy formation may occupy cerium sites that are not in next neighbor position to the corresponding defect. The possibility to investigate electron localization in reduced ceria opens a unique way to monitor oxidation and reduction processes in this chemically important system [226].

As described in section 5.2.1 the presence of empty Ce *4f*-states in the stoichiometric ceria film could be probed with STS under certain conditions. The detection of the partially filled Ce *4f*-orbitals at the Ce^{3+} ion sites proved to be even more challenging. For normal tunneling conditions the tip is too far away from the spatially confined *f*-states and cannot overlap with them. An overlap of the tip wave functions and the filled gap-states could only be achieved when stabilizing the tip inside the empty *f*-band and then ramping the bias to negative values. As reported in section 5.2.1 the stoichiometric ceria film shows no filled states above the valence band, which is shown in figure 5.15. In contrast $\frac{dI}{dV}$ spectra taken in the vicinity of surface oxygen defects exhibit a new peak at around -1.5 eV. This is shown in figure 5.16. The appearance of this additional peak depends very critically on the tip positioning and already a very small displacement leads to its complete disappearance. Due to its energy position and its strong spatial confinement this peak is assigned to filled Ce *4f*-states localized at Ce^{3+} ions. These filled states have been detected with other, spatially averaging, spectroscopies such as PES and EELS before [165, 198, 227]. The energy position of the observed peaks in STS fits very well to the reported energy positions of the filled Ce *4f*-states.
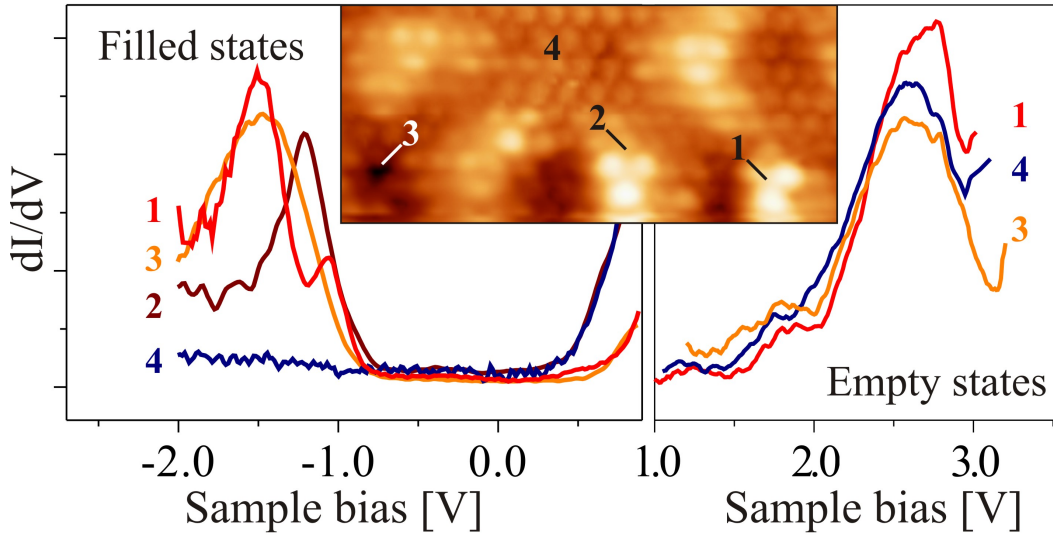
Figure 5.16: Differential conductance spectra taken in the vicinity of surface oxygen vacancies in the ceria film. Spectra taken at negative bias reveal additional filled states close to the defect sites which are absent on the stoichiometric film. The tip positions are marked in the inset (1.2 V, 8 x 4 nm^2). While the $\frac{dI}{dV}$ maximum at around 2.3 V reflects the empty f-band of ceria, the peaks at -1.1 and -1.5 V are assigned to filled f-like gap states.

Careful inspection of the data obtained with various tips on various film preparations reveals a relation between the topographic appearance of a defect and the structure of the corresponding $\frac{dI}{dV}$ signal. Spectra taken in the vicinity of paired protrusions display a double peak structure with $\frac{dI}{dV}$ maxima at -1.5 eV and -1.1 eV (see figure 5.16, spectra 1) whereas spectra taken close to triple protrusions only show a single peak at around -1.2 eV (see figure 5.16, spectra 2). Other structural defects, such as holes in the ceria film or step edges also display single filled gap states at an energy of around -1.5 eV (see figure 5.16, spectra 3). The detailed properties of line defects and step edges are addressed in section 5.2.3 of this thesis. It is also noteworthy that all different defect types display empty-state spectra similar to the one of the stoichiometric ceria film, as can be seen in figure 5.16 on the left side. This appears surprising because the empty Ce *4f*-states are expected to shift up in energy for the Ce^{3+} ions and become indistinguishable from the conduction band onset in tunneling spectra [228]. However, due to the fact that the tunneling spectra always average over a small surface area also contributions from the neighboring ions are expected.

The different energy positions and even the splitting of the peak for a certain configuration can be qualitatively understood in terms of different positions of the two extra

electrons with respect to the vacancy position. For a symmetric distribution of the extra electrons with respect to the vacancy, e.g. two nearest neighbor positions, one would expect only a single peak, since the positions should be energetically undistinguishable. If however an asymmetry is introduced, e.g. by one electron sitting in a next neighbor position and the other further away from the vacancy, one could expect two different energy levels for the two electrons and thus a splitting of the peak in the $\frac{dI}{dV}$ spectra. This explanation only holds if the spectra average over a certain area underneath the tip. This area must be very small because moving the tip by more than 1 nm away from the vacancy leads to a complete vanishing of the feature. On the other hand, the area must be large enough to include spectroscopic information from both Ce^{3+} ions because a double peak structure is observed. This is another hint for a limited averaging in STS comparable to the observation of empty Ce *4f*-states at the defect sites as discussed above. This averaging is usually accounted for by assuming an effective area for tunneling underneath the tip with a typical size of 5-10 $Å^2$ depending on the bias voltage [229, 230].

However, with only the experimental evidence those explanations must be considered as nothing more than mere speculations on the true nature of the observed spectra.

Therefore DFT calculations have been performed by the group of Prof. Sauer in Berlin [226] in order to gain further insights into the charge localization and energy positions. Those calculations have been performed at the PBE+U level (U = 4.5 eV) using the VASP code with a 400 eV cutoff for the plane-wave basis set [231, 232]. Atomic cores are described by the projected augmented wave method. Whereas the oxygen vacancy is kept fixed at the CeO_2(111) surface, all cationic sites in the different layers of the (3x3) supercell are allowed for the Ce^{3+} ions. The electronic structure is obtained from a (2x2x1) *k*-point sampling of the Brillouin zone, then the formation energy of the oxygen vacancy is computed with respect to $\frac{1}{2} O_2$ in the gas phase. Six different configurations of the two Ce^{3+} ions with defect-formation energies below 2.6 eV are found. An overview over the different configurations is given in table 5.1. The Ce^{3+} positions are hereby labeled according to a n_m scheme, with *n* denoting the cation shells surrounding the vacancy and *m* being the cationic layer counted from the surface. For example, 3_1 describes a position in the surface cerium layer that is third neighbor to the defect. The properties of the Ce^{3+} ions are determined by their coordination number, which is the number of surrounding oxygen ions. A Ce^{3+} in the top-most trilayer has seven O^{2-} neighbors if it sits in a second-neighbor position to the defect (a 2_1 site), but only six if it sits in a first-neighbor position of the same layer, which would correspond to a 1_1 site. For a Ce^{3+} in the bulk with no adjacent defect, the coordination number increases to eight. There are two configurations in table 5.1 with equal coordination number for the Ce^{3+} ion pair. Those are the 2_1-2_1 and 1_1-1_1 configurations. Both ions have filled *f*-orbitals with the same energy, as they experience the same chemical environment. For Ce^{3+} pairs with different coordination numbers, an energetic splitting of the *f*-orbitals is induced by their unequal distances from the oxygen defect. The splitting is of the order of 0.1 eV if the coordination number differs by one (as in the 1_1-2_1 and 1_1-3_1 configurations), but increases to 0.5 V for a coordination number difference of two. The 1_1-4_2 pair is an example for the latter, as it consists of a six-fold and an eight-fold co-

ordinated Ce^{3+} ion in the surface and sub-surface layer, respectively. The calculated partial density of states for this configuration is shown in figure 5.17.

Ce^{3+} config.	Ce^{3+}-Ce^{3+} distance [pm]	Ce^{3+} - defect distance [pm]	Coord. numbers of Ce^{3+}	$E_{def}(\frac{1}{2}O_2)$ [eV]	f-state splitting [eV]
2_1-2_1	391	452;452	7;7	2.06	0.00
1_1-2_1	390	254;453	6;7	2.16	0.05
1_1-1_1	417	254;254	6;6	2.22	0.00
1_1-3_1	374	251;595	6;7	2.28	0.10
1_1-4_2	543	251;708	6;8	2.45	0.47
2_2-4_2	390	447;708	8;8	2.59	0.06

Table 5.1: Calculated geometric structures, Ce^{3+} coordination numbers, vacancy formation energies (E_{Def}) compared to $\frac{1}{2}$ O_2 and expected splitting of occupied f-states. Adapted from [226].

These theoretical results reveal why the experimental spectra sometimes show a single and sometimes a double-peak structure. Spectrum 1 in figure 5.16 is taken close to a defect with asymmetric electron distribution, e.g. the two resulting Ce^{3+} ions have different coordination numbers while the ion pair belonging to spectra 2 and 3 have similar coordination numbers. This assignment is another indication that the measured spectra are indeed correlated to the filled Ce $4f$-states. Yet those informations still do not allow to determine the exact position of the two Ce^{3+} ions with respect to the oxygen vacancy because the spectra are only sensitive to the local chemical environment.

However, the spatial correlation between the oxygen vacancy and the associated Ce^{3+} ion pair is indirectly contained in the atomically resolved STM images since they also include information on the local electronic structure. In order to demonstrate this, empty-state images have been simulated at a bias voltage of 2.0 V that enables electron tunneling into the empty Ce $4f$ states. Some results are shown in figure 5.18 a, c and d. As expected, the Ce^{4+} lattice dominates the images when sampling the empty DOS between 0 and 2 eV. The Ce^{3+} ions (indicated by large blue dots in figure 5.18 a, c and d) are not visible, because their $4f$-states shift to higher energies due to a better screening of the core potential in the electron-rich ion. This is also evident from figure 5.17. In contrast, the Ce^{4+} ions adjacent to an oxygen defect are particularly bright, reflecting their better accessible state density in the $4f$-region (0.6-1.6 eV) compared to regular Ce^{4+} surface ions. The reason is that those $4f$-states spill out towards the vacuum as the repulsive potential of one O^{2-} ion above is missing. As shown in figure 5.18 b they extend towards the empty space and partially delocalize. Therefore the Ce f-band broadens and a delocalized state splits off. The tunneling into these modified states is facilitated and hence the contrast for those Ce^{4+} ions next to an oxygen defect becomes larger.
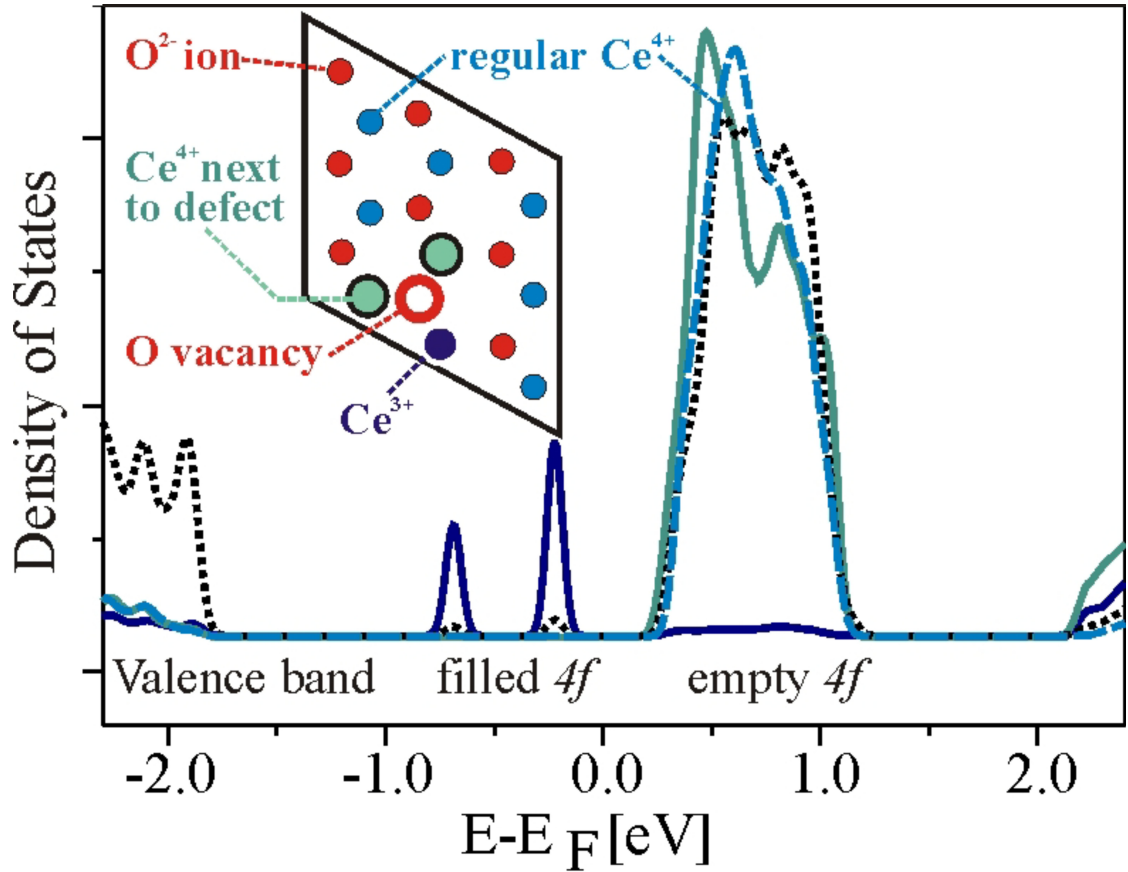
Figure 5.17: Calculated total and atom projected DOS for the 1_1-4_2 configuration of a Ce^{3+} ion pair. The dark solid line represents the DOS of the Ce^{3+}, the bright solid line the DOS of Ce^{4+} next to the vacancy. The light blue, dashed line represents the DOS of other surface Ce^{4+} and the dotted line the total DOS. All spectra are normalized for the number of cerium atoms in the unit cell. The inset shows the calculated unit cell, where one Ce^{3+} is next to the vacancy, which is marked by the ring. The second Ce^{3+} is in the layer below for this configuration and therefore not shown. Adapted from [226].

Combining these results with the experimental data, it is possible to pinpoint the position of the excess electrons with respect to the oxygen defect. For the case that the vacancy is surrounded only by Ce^{4+} ions and the Ce^{3+} ions occupy more distant positions, a symmetric triple protrusion is visible in the STM images. This configuration is displayed in the calculated STM image 5.18 a and also found experimentally in figure 5.11 e. It must be noted that although this triple signature is observed in the experiment, its abundance on the surface is rather small. The most frequently observed defect type is a paired protrusion, which can now be identified as two Ce^{4+} ions localized next to an oxygen vacancy with the third faint species next to the defect marking one Ce^{3+} ion. The position of the other reduced cerium ion cannot be determined from the image. This situation is shown in figure 5.18 c for the simulated and in figure 5.11 d for the experimental case. The last possible configuration is a single maximum, arising from an oxygen vacancy surrounded by two dark Ce^{3+} and one protruding Ce^{4+} ions. This is shown in figure 5.18 d. However, this configuration has not been observed experimentally, which might be understood in terms of its higher formation energy with respect to the 2_1-2_1 and the 1_1-2_1 configurations as listed in table 5.1.

This case study of oxygen vacancies in ceria shows that the combination of STM imaging and spectroscopy with DFT calculations provides a powerful tool to understand local oxide properties. In this section a unique insight into the localization of the two excess electrons that remain in the $CeO_2(111)$ surface upon oxygen vacancy formation is presented. The two associated Ce^{3+} ions are always allocated in different coordination spheres around the defect, which is in agreement with earlier theoretical results [220]. The driving force for adopting such open configurations is the better ability of the system to relax lattice strain induced by the more spacious Ce^{3+} ion compared to its Ce^{4+} counterpart.

5.2.3 Reduced Cerium Ions at Structural Defects of the Ceria Film

On atomically flat ceria films grown on ruthenium single crystals line defects and step edges are the most abundant defect sites. Therefore the understanding of the electronic properties of those defects is crucial in order to grasp the overall characteristics of the ceria system. It can be assumed that step edges and line defects contribute a significant part to the catalytic properties of the ceria system when used in catalytic applications. A lot of work has been done by various groups in order to shed light on the properties of line defects of ceria [185, 201, 233].

The formation of reduced Ce^{3+} ions with partially filled *4f*-bands in the ceria gap does not only occur in the vicinity of single oxygen vacancies as described in section 5.2.2 but also at under- coordinated sites at step edges, pits or line defects.
This is not surprising since under-coordinated cerium ions at low symmetry sites are not expected to be in a formal 4^+ oxidation state. Even though oxygen vacancies have only been observed on ceria terraces, it can be assumed that they also exist at step edges
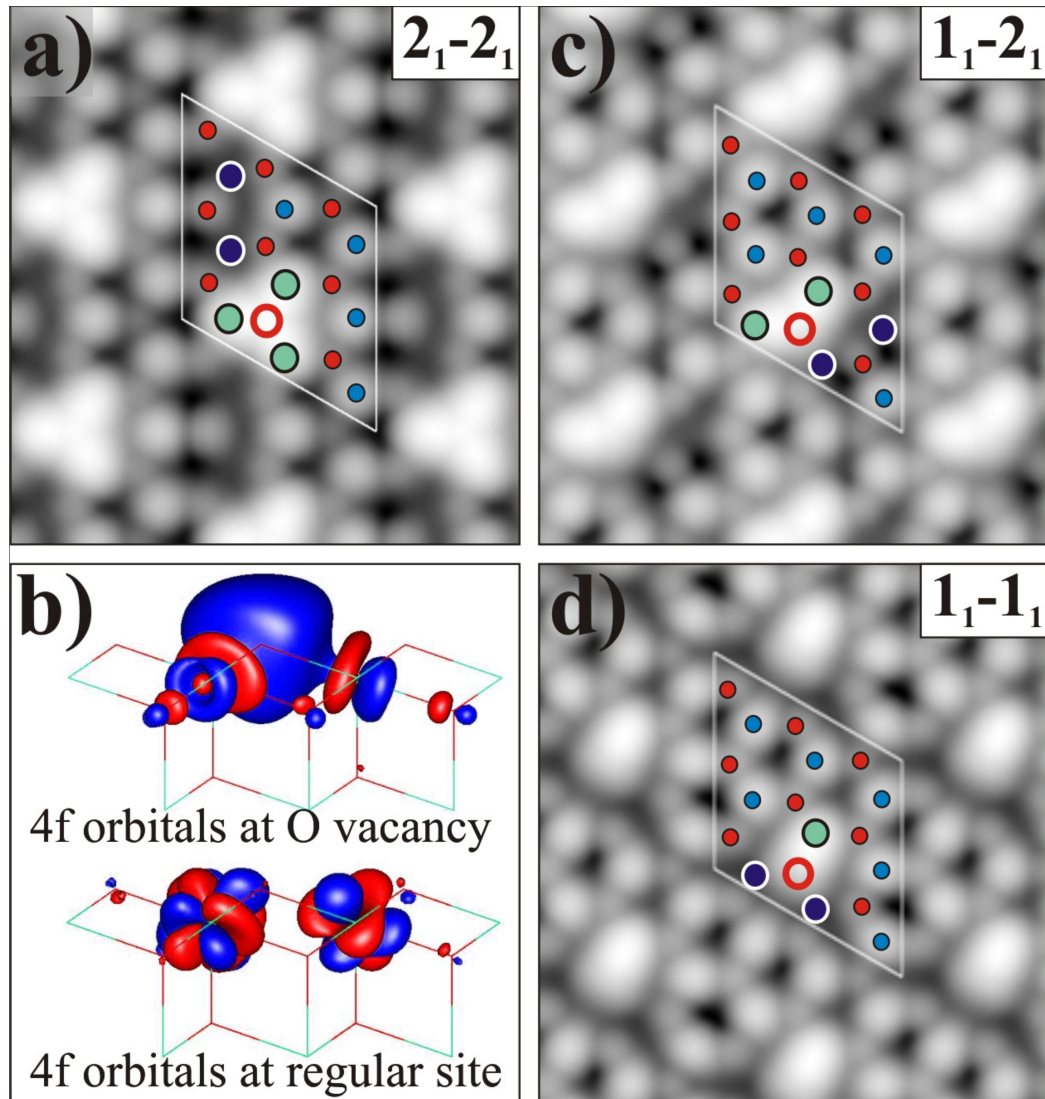
Figure 5.18: DFT simulations of empty-state STM images based on integrated empty LDOS between 0 and 2 eV performed by the group of Prof. Sauer. Small blue dots denote the Ce lattice, red dots the O positions and the red circle the O defect. Whereas Ce^{3+} ions are nearly invisible (large blue circles), Ce^{4+} ions adjacent to an O defect site appear brighter. This results in differently shaped features depending on the number of Ce^{4+} ions in first-neighbor positions to the defect: (a) three Ce^{4+} (2_1-2_1 configuration), (c) two Ce^{4+} (1_1-2_1 configuration) and (d) one Ce^{4+} (1_1-1_1 configuration), (b)The enhanced contrast originates from the greater spatial extension of the Ce^{4+} empty *4f*-orbitals in presence of the vacancy. Adapted from [226].
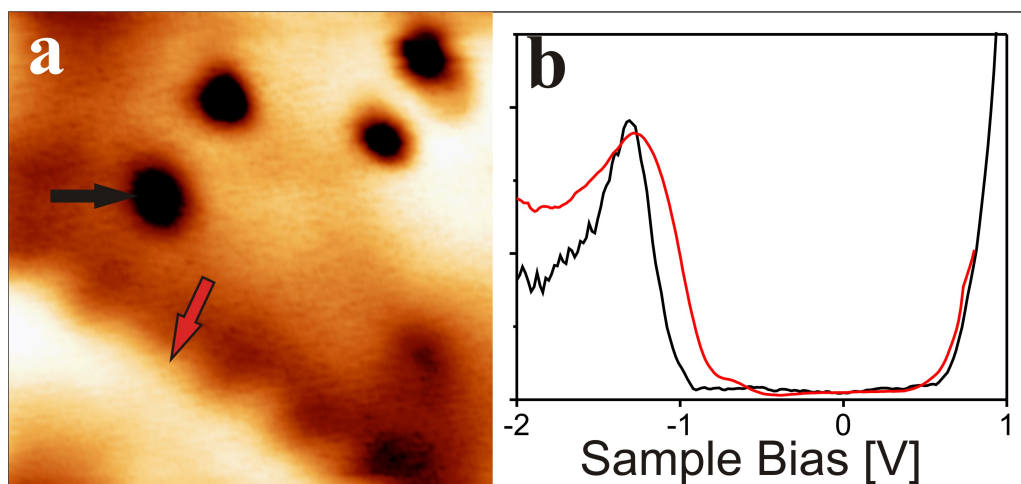
Figure 5.19: Reduced cerium ions can also be identified on structural defects such as step edges and holes in the film. (a) Ceria film with structural defects. (b) Spectra taken on positions marked with arrows in (a) clearly reveal the presence of filled Ce *f*-states. The red spectrum is taken at the edge, the black one on the hole.

and other low symmetry sites. This is corroborated by the fact that metal adsorbates preferentially nucleate at those sites [185, 234]. The fact that those defects have not been resolved in scanning probe studies is understandable because of the large corrugation of the edges compared to the small corrugation of the defects. However, just like for single oxygen vacancies the filled Ce *4f*-states can be detected at those structural defect sites with differential conductance spectroscopy. In this way the defect sites can be directly probed even if no clear signature in topographic images is revealed. Figure 5.19 shows STS spectra taken on a step edge (red spectrum) and on the edge of a hole in the ceria film (black spectrum). Both spectra clearly reveal accessible density of states below the Fermi-level but well within the band gap. As in the case of single oxygen vacancies this peak is assigned to filled Ce *4f*-states. The spectra show only one peak at an energy of roughly 1.5 eV which is expected since the multi-peak structure observed for some single vacancy configurations could be assigned to an asymmetry in the electron distribution with respect to the vacancy. Such an asymmetry is not expected for larger defects that involve many extra electrons and no clear center of symmetry.

The presence of reduced cerium-ions with partially filled *f*-states at low-coordinated sites is also deduced from line spectra taken across a hole in the ceria film. This is shown in figure 5.20 on the left side. For those line spectra the tip is moved along the line defined in the topographic image in figure 5.20 in the middle. A set of four spectra is taken at every point along the indicated line. The averages of those four spectra are shown for every point. It is clearly visible that the characteristic peak for the filled *f*-
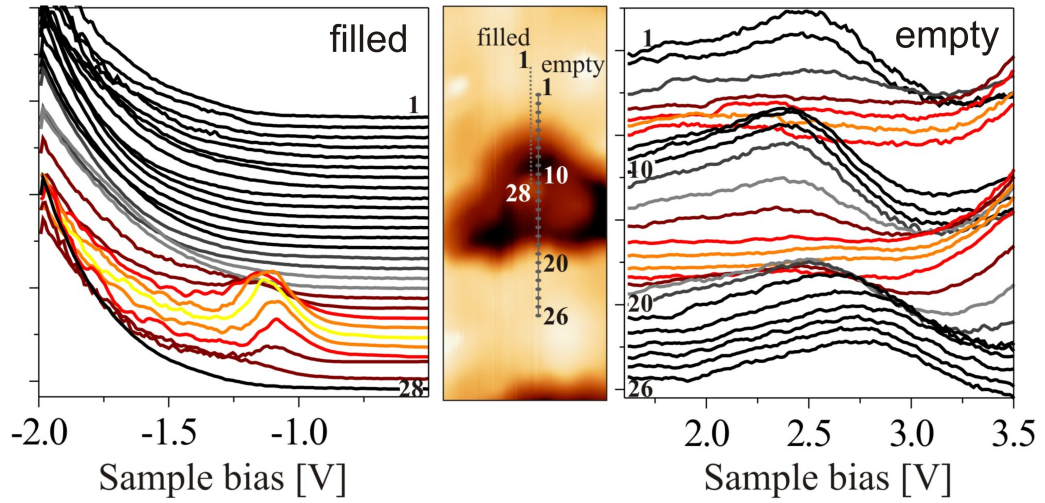
Figure 5.20: Spectral series taken across a trilayer-deep hole in the CeO_2/Ru(0001) film. In the step region, filled f-states emerge in the spectra while the empty f band looses intensity on the expense of the conduction band edge at 3.5 V. The spectral positions are marked in the central STM image (2.25 V, 22 x 9 nm^2).

states only occurs when the tip is close to the edge of the hole. In this case a maximum at around -1.2 V appears and thus at a slightly lower energy than observed for the step edge and pit in 5.19. Similar to the energy shift observed for empty $4f$-state spectra on different films described in section 5.2.1, this shift might also be understood in terms of different band bending due to a different film thickness. Furthermore, the sensitivity of the f-state energy on the local chemical environment, as pointed out in the last section, also applies in this case. However, the peak still indicates the presence of filled Ce $4f$-states. As expected spectra taken on flat parts of the film show no density of states in the band gap and provide no indication for filled f-states.

Similar spectral series have also been taken for positive bias, thus giving the local density of empty states. For the flat, stoichiometric film the empty cerium $4f$-states appear again as a peak at around 2.7 V. For spectra taken with the tip on top of the edge of a hole this peak vanishes as can bee seen in figure 5.20 on the right side. On first glance this observation is in contradiction with the results obtained on single oxygen vacancies in section 5.2.2, where the empty f-states could also be observed for defect sites. However,the contradiction is solved when considering the fact that the high concentration of defects leads to a redshift of the conduction band. This is explained by a positive dipole induced by the comparably high defect concentration. In the section 5.2.4 of this thesis it is shown that a similar behavior is observed on the flat terraces of the film if the ceria has been globally reduced.

Due to this redshift the conduction band onset is already visible in the spectra of 5.2.2

at the edge positions. Therefore, the stabilization set point of the tip is not in the band gap any more and the tip-sample distance becomes too large for the tip wave functions to overlap with the very localized Ce *4f*-orbitals. These observations constitute direct and local prove that low symmetry sites also host reduced Ce^{3+} ions in the ceria film.

5.2.4 Electronic Properties of Globally Reduced Ceria Films on Ru(0001)

As discussed in the previous sections the ceria film has different structural defects such as step edges or occasional pits on flat terraces. Beyond that single surface oxygen vacancies can be introduced by mild electron bombardment. Those isolated defects are ideal to study the local reduction of the film and the localization of the extra electrons as demonstrated in section 5.2.2. However, the situation changes if the ceria film is reduced on a global scale. In this case it is no longer possible to differentiate between single defects or even defect lines or clusters but the film changes its appearance and properties as a whole.

As described in section 5.1.3 there are several different ways to globally reduce the ceria film. Well established methods are: irradiation with high energy photons [196], bombardment with Ar^+ ions [165], exposure to a reducing H_2 atmosphere [165], vacuum annealing [197] and electron bombardment [198].

The two methods that have been employed for this thesis are vacuum annealing and electron bombardment either from an electron gun or the STM tip.

In the first example, a stoichiometric ceria film, that has been characterized with the STM before, as shown in figure 5.21 a, is subjected to vacuum annealing up to 1100 K. The stoichiometric, atomically flat film shows the known step edges and islands. After vacuum annealing the same structural elements of the film are still visible but a new blurry pattern appears everywhere on the surface as evident from figure 5.21 c and d. This blurry structure is always present in STM images but not exactly reproducible in the sense that the exact shape and orientation of the blurry structure is rather random and not fixed when scanning the same area several times with the same tunneling parameters. This is a hint that the blurriness is not a sign of a real topographic change of the surface but rather a sign of an instability in the tunneling junction. The possible physical origin of this instability is addressed later in this section.

Not only the contrast in topographic STM images changes. Differential conductance spectra taken across the band gap of a stoichiometric and a reduced film reveal a red-shift of the conduction and valence band onsets after reduction. This is shown in figure 5.21 b, where the red and black curves show spectra taken on the stoichiometric and the reduced film respectively. This corresponds to the findings on the conduction band red-shift at line defects reported in section 5.2.3 of this thesis. When probing the band gap with STM conductance spectroscopy one has to be aware of several parasitic effects, e.g. convolution between transmission probability and actual state density, the set point dependence and tip-induced band-bending effects. Therefore it is not possible to extract absolute values for the band gap from the performed spectroscopy. However, the exis-
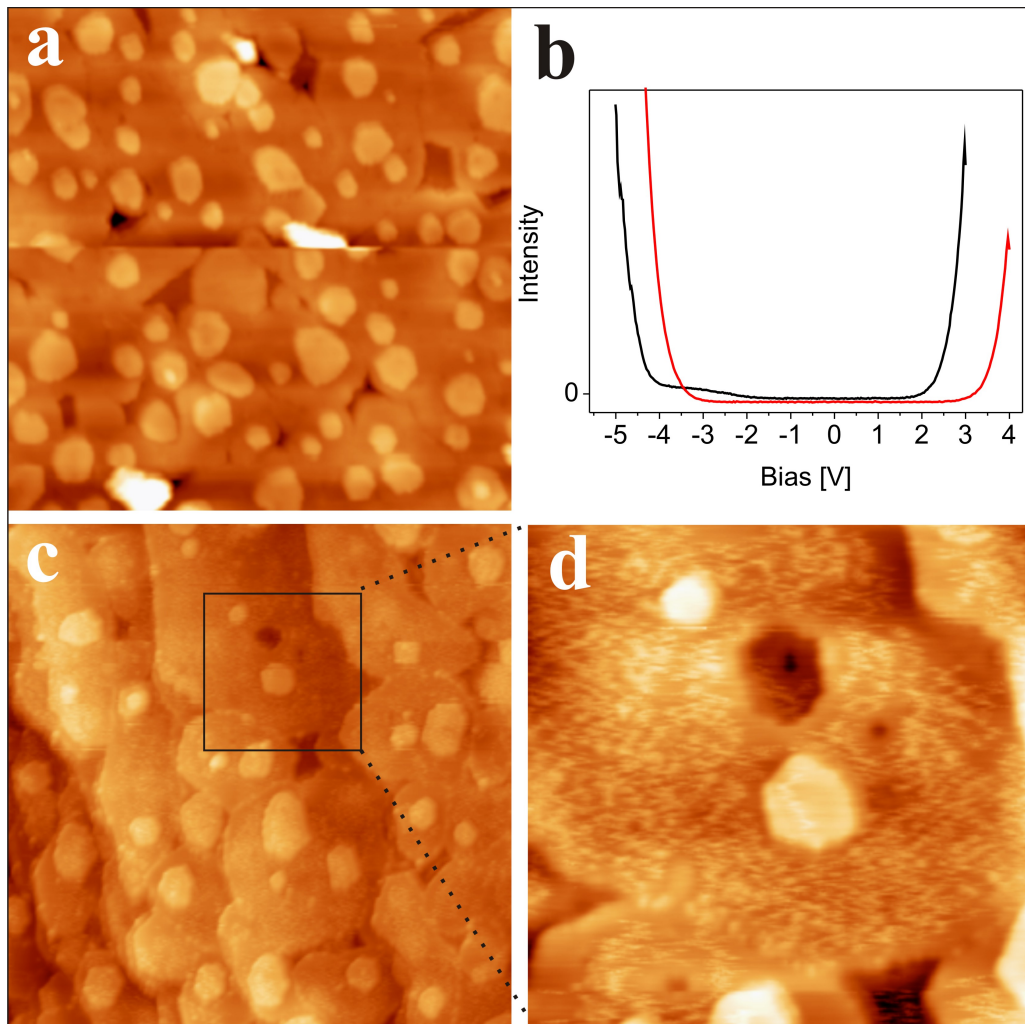
Figure 5.21: (a) Stoichiometric ceria film before thermal reduction. Note that the tip change in the middle of the image does not change the contrast ($U_B = 4.0$ V; 150 x 150 nm^2). (b) Red and black spectra taken on the stoichiometric and the reduced film respectively. A redshift of the conduction band onset for the reduced film is revealed while the overall gap size remains constant. (c) Overview image of the reduced film ($U_B = 4.0$ V; 150 x 150 nm^2). (d) Zoom-in of (c) displaying the blurry structure as sign of the reduced film.

tence and the rough extension and position of the band gap can be deduced from the spectra of the reduced and the stoichiometric film. While the band gap in the stoichiometric case stretches rather symmetrically around the Fermi-level from +3.0 V to -3.0 V, the gap for the reduced film is shifted by around -1 eV with respect to the Fermi-level. Therefore the band gap becomes asymmetric with respect to the Fermi-level with the conduction band moving closer to E_F, which is an indication for n-doping. This can be understood in terms of band bending. As in the case of positive lithium ions in silica that create a surface dipole described in chapter 4, the oxygen vacancies in the ceria surface introduce a dipole that leads to a redshift of the conduction band with respect to the Fermi-level. Furthermore, the presence of filled Ce *4f*-states may alter the alignment of the ceria bands with respect to the ruthenium Fermi-level.

It has to be noted that a very strong reduction of the CeO_2 (111) surface leads to the formation of Ce_2O_3 [197]. When going from CeO_2 to Ce_2O_3 the symmetry is expected to remain hexagonal in both cases which makes a differentiation with LEED or STM measurements difficult. However, the electronic structure is expected to alter dramatically. Ce_2O_3 is not a wide band gap insulator anymore and will not show a band gap in $\frac{dI}{dV}$ spectroscopy as the one in 5.21 b. It is therefore concluded that the film is reduced especially at its surface but still in an CeO_{2-x} state with $x < 0.5$.

As mentioned above, the reduction of the ceria film can also be achieved by electron bombardment. In order to make use of this possibility the film was bombarded with electrons from the electron gun of the LEED setup with an energy of 60 eV for several minutes. Due to the rather low number of electrons which is in the order of mC, only low defect concentrations were achieved with this method. However, the approach proved useful in order to create the low defect concentrations required to study single oxygen defects, as discussed in section 5.2.2.

The second possibility for electron injection into the film makes use of the STM tip. Even though the number of electrons is much lower than for the first method, the current density is several orders of magnitude higher due to the very local nature of this method. Only electrons above a certain energy threshold are able to induce a reduction of the film. This threshold has been found to be around 6.0 eV. Tunneling at softer conditions does not effectuate any visible changes in the film. However, if the film is subjected to electrons from the STM tip at biases above 6 V the film starts to change its appearance. Eventually the same signatures that were observed for thermally reduced films start to appear locally where the tip has been scanning. This is illustrated in figure 5.22. The pristine oxide film is shown in figure 5.22 a. Subsequently the area indicated by the square in figure 5.22 has been scanned several times with higher bias (6 V between a and b, 7 V between b and c and 8 V between c and d). The increasing reduction is clearly observed in the area subjected to high bias scans, while the rest of the surface remains unchanged. Areas that have been reduced by electron injection from the tip show the same blurry appearance as films that were thermally reduced. It is therefore concluded that both methods have the same effect, even though annealing is a global method that changes the whole film, while electron bombardment from the
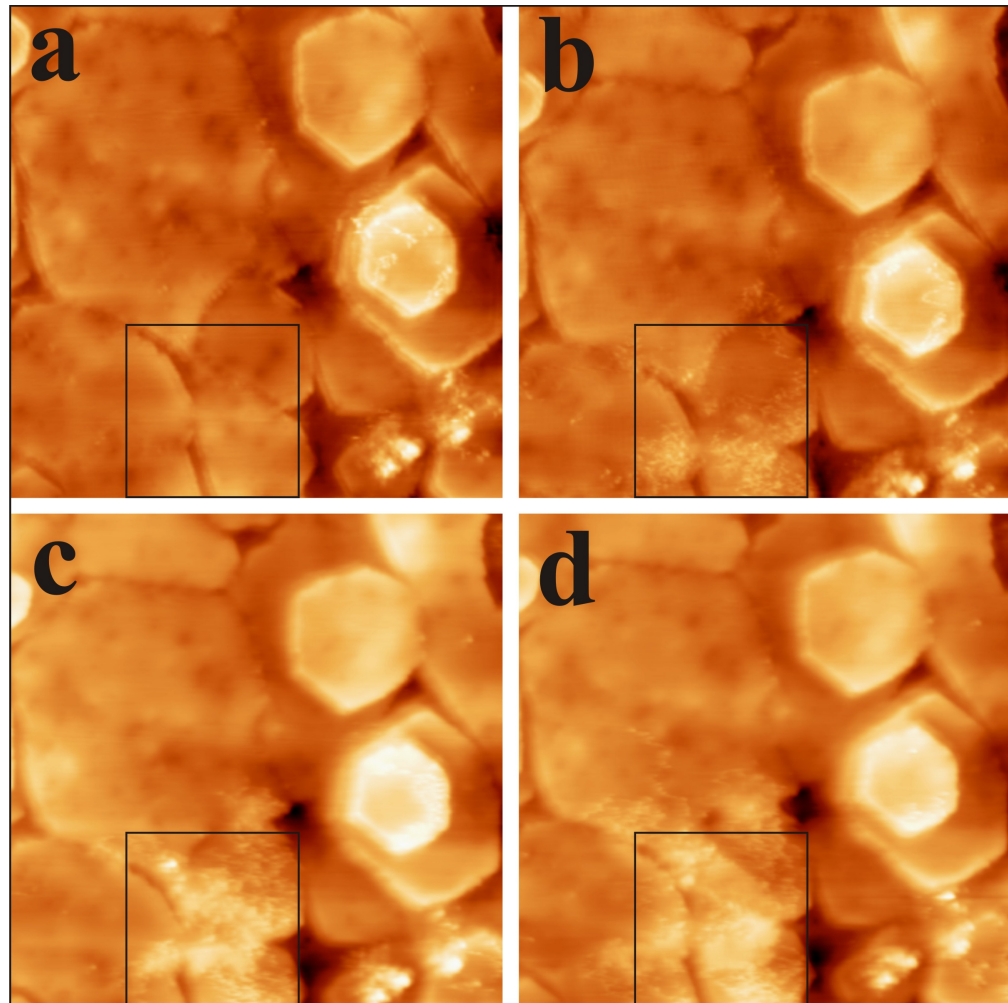
Figure 5.22: The reduction of the ceria film can also be induced by energetic electrons from the STM tip. All images have a size of 100 x 100 nm^2 and are taken at a bias of U_B = 4.0 V. (a) shows the as prepared, stoichiometric ceria film. (b-d) show the same region after scanning the area indicated by the square at higher bias (U_B = 6.0, 7.0 and 8.0 V respectively). The high bias imaging leads to an increased reduction in this area, while the area outside the square remains unchanged.

tip only affects the area underneath the tip. It should be noted that tip induced vacancy formation with scanning probe techniques has been observed for other oxide systems, for example on magnesium oxide films grown on silver single crystals [235].

The blurry structure observed after applying either of the two reduction methods can be explained in terms of a dynamic process involving the high defect concentration induced by the reduction. The large number of oxygen vacancies created upon reduction leads to an instability in the tunneling junction. When scanning the tip across the surface, the local defect structure might change due to the presence of the strong, local electric field between the tip and the surface. Different scenarios seem possible but a final conclusion can not be deduced from the experimental data. It seems reasonable to assume that mobile oxygen atoms that are not well embedded in the surface oxygen lattice jump in between vacancy sites, creating an instability in the tunneling current. This hopping motion requires a certain minimal defect concentration and is driven by potential changes induced by the scanning tip. The fact that the electric field induced by an STM-tip can play a crucial role in local oxidation or reduction of oxides is well known and extensively studied (see for example [236, 237] amongst many others). Tip induced migration of defects has been observed before [238] and similar physics is behind atomic and molecular manipulation performed with the STM [239, 240].

5.2.5 Electronic Properties of Ceria Islands and Step Edges

As reported in the previous sections atomically flat ceria films with large terraces have been grown on a ruthenium (0001) substrate. In total more than 70 such films have been prepared and almost all of them show growth of ceria islands on top of ceria terraces in the topographic STM images. Therefore also the electronic properties of these islands and especially their delimiting step edges are of interest.

The experiments described here help to clarify certain aspects of the origin of the electronic peculiarities found on islands and their step edges. The investigation of this topic was first proposed and started by Dr. Shamil Shaikhutdinov from the Department of Chemical Physics at the Fritz-Haber-Institut [241].

As described in section 5.1.4 of this thesis different islands are found on the film: the almost triangular ones with steps along the [110] and [100] directions and the more hexagonal ones with [211] oriented edges. Atomic models of the different island types are given in figure 5.25. From the proposed model a different electronic structure for the different edge types is expected. A cut along the different directions reveals that the facets along the [100] and the [211] direction do not expose a dipole moment, while the facet along the [110] direction is polar and is therefore expected to have different properties.

Taking topographic STM images at different bias voltages across ceria islands reveals a distinct bias dependent contrast. The different edges of the ad-islands on the oxide film show a different behavior. As shown in figure 5.23 in the upper row, the [110] oriented facets change their apparent height in a drastic way when the sample bias is increased to larger positive values. When increasing the bias above 4.0 V the three nano
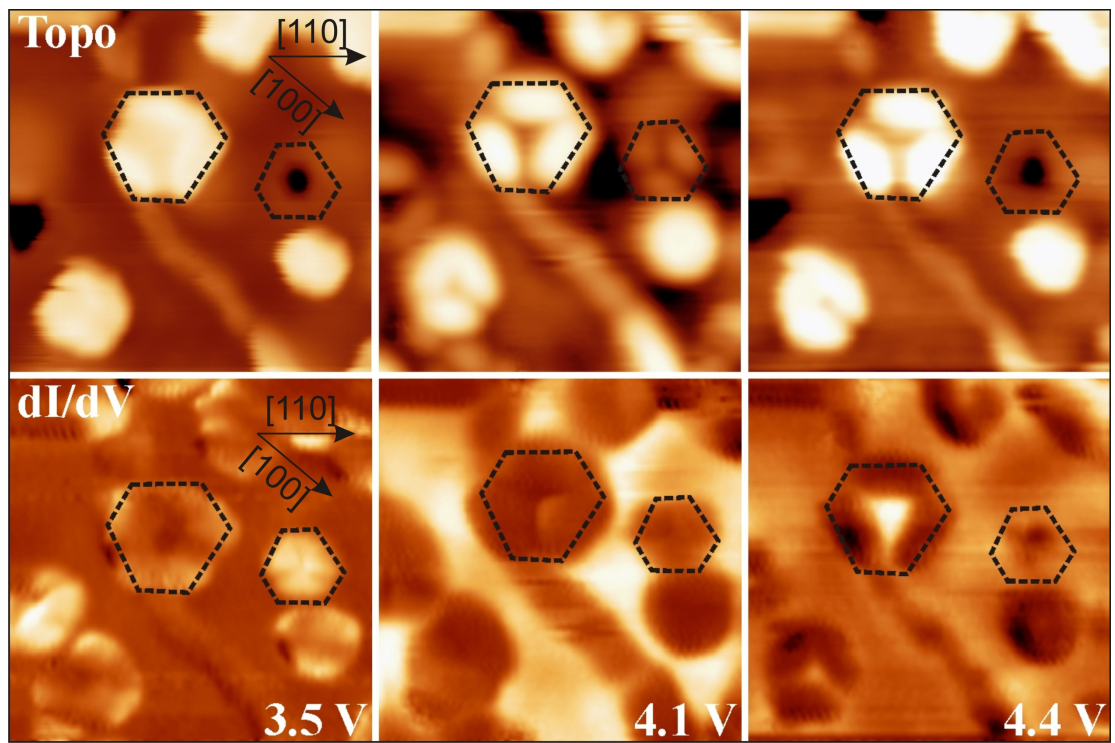
Figure 5.23: Topographic (upper row) and conductance images (lower row) of islands and pits in the CeO$_2$ (111) surface taken as a function of sample bias (16 x 16 nm^2). While the topographic images are dominated by the bright contrast of the [110] nano facets, the $\frac{dI}{dV}$ maps directly show the onset of the conduction band on the [110] nano facets (at 3.5 V), the oxide terrace (at 4.1 V) and the interior of small ad-islands (at 4.4 V).

facets along the [110] direction of the ceria island and part of the domain boundary become bright. It is also observed that the other three facets along the [111] direction and the center of the island remain dark in the investigated bias range. It can therefore be concluded that additional states become available for tunneling on selected structural sites of the surface.

Simultaneously recorded differential conductance images directly indicate the electronic nature of this effect and reveal the energetic positions at which the additional LDOS becomes available for tunneling. As shown in the lower row of figure 5.23, the additional conductance channel opens at around 3.5 eV for the nano facets along the [110] direction, while the onset for the oxide terrace and the middle of the ceria-island is determined to be around 4.1 and 4.4 eV respectively.
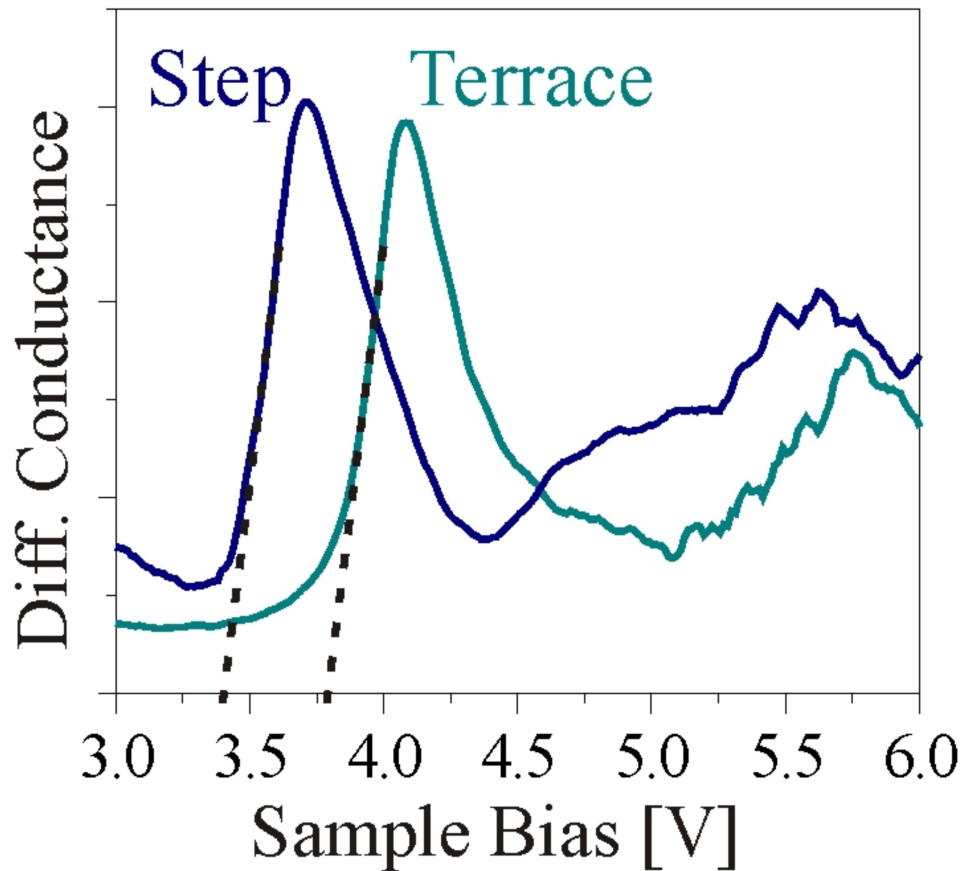

Figure 5.24: Constant current $\frac{dI}{dV}$ tunneling spectra taken on the flat film and on a [110] nano facet on the edge of a ceria island clearly show a redshift of the conduction band for the case of the edge.

This observation is further corroborated by constant current $\frac{dI}{dV}$ tunneling spectroscopy measurements performed on such step edges of ceria islands and on flat

parts of the film. This is shown in figure 5.24 where a clear redshift of the differential conductivity peak is observed for spectra taken on a [110] step edge. The value for the onset of the conductivity peaks is found to be 3.4 eV on the step and 3.8 eV on the terrace. These values differ slightly from the values observed in differential conductance images. The difference for the onset-values is due to the rather coarse steps for the bias increase in conductance imaging.

This experimentally observed opening of new conductance channels is assigned to a redshift of the conduction band along the steps. Such a shift can be caused by different factors. Defect states in the oxide band gap formed by low-coordinated atoms or vacancy sites, may be responsible for the opening of low-lying conductance channels [242]. In addition, electronic states with distinct 1D character might emerge along the oxide edges, reducing the local gap size at those positions [243, 244]. Finally, uncompensated electric fields inside the oxide lattice might trigger a rigid shift of the band onsets, as observed for instance on polar oxide materials [245]. The observed downshift of the conduction band hereby requires a positive dipole localized in vicinity of the oxide line defects [190, 246].

The experimental data is compatible only with the last scenario, as the band onset simply shifts by -0.4 V but does not display evidence for new spectral features. Therefore uncompensated dipoles induced by the different line defects are expected to responsible for the shift.
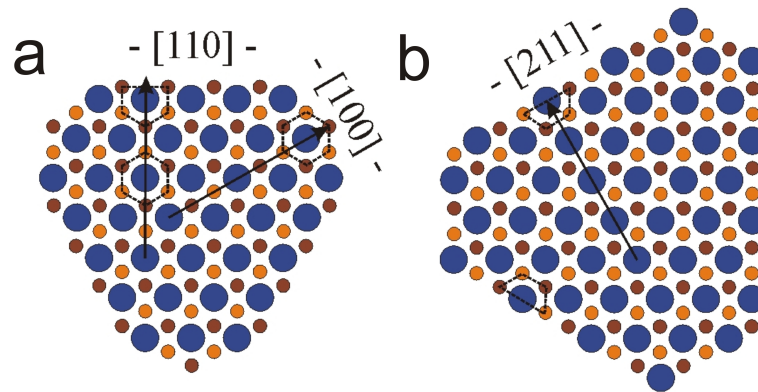

Figure 5.25: Structure model of the different step edges of ceria islands on CeO_2(111) observed in the experiment. While the [100] and [211] oriented nano facets expose no dipole moment, the [110] facet is polar and exhibits a different electronic structure.

CeO_2(111) being a layered material is especially susceptible to polar effects because any change in the occupancy of the O-Ce-O trilayer immediately leads to a residual dipole. In a regular (111) unit, one O^{2-} ion in the bottom layer faces one Ce^{4+} in the central and another O^{2-} species in the top layer, resulting in a fully compensated charge distribution as shown in figure 5.25. In contrast, the top oxygen is missing along the [110] nano-facet, while the bottom ion is stabilized via interactions with two

Ce^{4+} neighbors and the oxide plane below. Consequently, a positive surface dipole μ_z emerges, the amount of which can be determined with the formula:

$$\mu_z = \sum q_i \cdot d = 1.07 \text{ x } 10^{-19} \text{ C x } 0.775 \text{ Å} = 8 \text{ x } 10^{-30} \text{ D} \tag{5.1}$$

Hereby d is the O-Ce layer distance and q_i the fractional charge per layer and unit cell. The positive dipole triggers a band bending according to the Helmholtz formula:

$$\Delta = \frac{e}{\epsilon_0 \epsilon_r} \mu_z \rho_d \tag{5.2}$$

with ϵ_r = 16 being the ceria dielectric function and ρ_d the dipole density on the surface [247].

The derived band shift of 0.45 eV assumes a two-dimensional dipole arrangement and will therefore be larger than the one-dimensional dipole arrangement along the step edges. Already this rough estimate provides a reasonable agreement with the experimentally observed shift of 0.4 eV.

The situation observed at the polar nano facets is similar to the one at the structural defects described in section 5.2.3, where a high concentration of reduced cerium ions caused the dipole responsible for the conduction band redshift. Therefore the line defect in 5.23 behaves similar to the [110] oriented nano facets.

The model also explains the different electronic behavior of [100] and [211] oriented nano facets. No dipole moment arises in those cases, as both oxygen ions in the top and bottom layer remain on roughly bulk-like positions and keep the charge distribution balanced. This stabilizes the flat-band situation of the flat ceria surface, in correspondence with the experimental data. However, also along the [100] edges, a dipole moment can be created simply by removing oxygen ions from the top-most layer. Similarly, surface oxygen vacancies along the domain boundaries inevitably lead to a positive surface dipole, which in turn induces a local downward bending of the oxide bands. It is therefore not surprising that different point and line defects in the ceria surface cause the same bias-dependent contrast enhancement as observed for the [110] planes with their intrinsic dipole moment.

5.3 Vanadium Adsorption on Ceria Thin Films Grown on Ru(0001)

The study of vanadium oxide has received considerable attention because it is the major active component of catalysts for selective oxidation reactions [15–18]. However, the activity of supported vanadia particles strongly depends on the support material used in the experiments [17, 248]. It has been shown that vanadium oxide supported on

reducible oxide materials, especially ceria, shows a significantly higher reactivity in oxidative dehydrogenation (ODH) reactions compared to vanadia supported on silica or alumina [16, 249, 250]. The origin of this effect was found to be the ability of ceria to stabilize reduced states by accommodating electrons in localized Ce f-states [251] as discussed in section 5.2.2 of this thesis.

For this thesis experiments have been performed in order to shed light onto the adsorption sites of different vanadium induced species on the ceria film and to illucidate the agglomeration behavior upon higher vanadium loads. One has to note that the STM can contribute only part of the explanation of the points mentioned above since it is, unlike true spectroscopic methods like IRAS or XPS, insensitive to the oxidation state of the vanadium features. Therefore some hints from topographic images are presented in this section which require complementary spectroscopic and theoretical work in order to draw further conclusions.
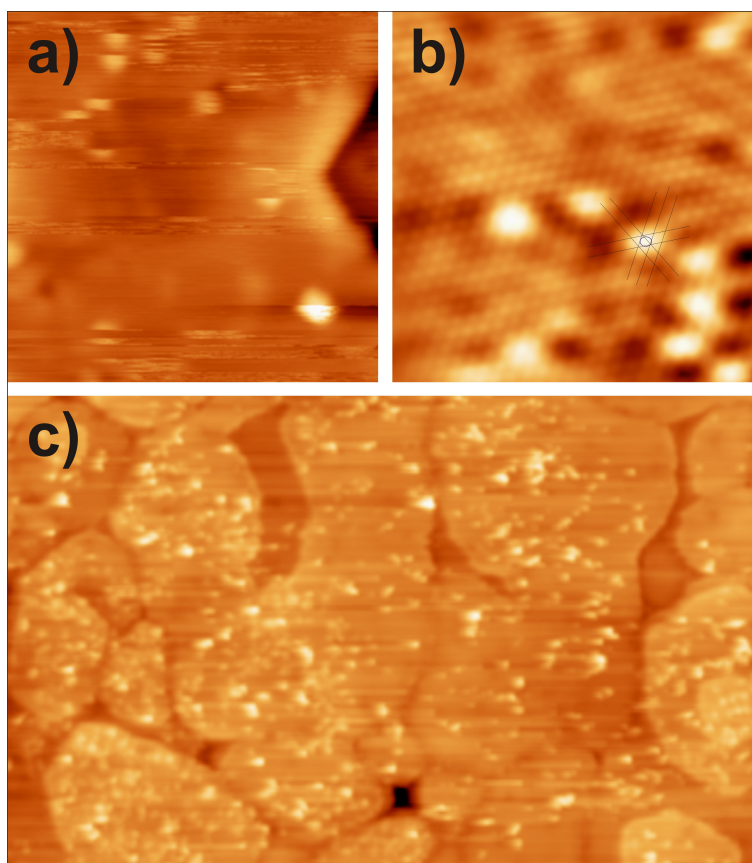

Figure 5.26: (a) Single V atoms on the ceria film deposited at 10 K in UHV (5.0 V, 20 x 20 nm^2). (b) Same situation as (a) with atomic resolution of the O sublattice (-3.5 V, 9 x 9 nm^2). (c) Overview image with unstable V features (4.0 V 150 x 100 nm^2).

The deposition of small amounts of vanadium onto the ceria surface in UHV at a temperature of 10 K leads to the observation of small protrusions in subsequently recorded STM images. Figure 5.26 shows a ceria film with such vanadium induced features. During tunneling the features proved to be rather unstable and could be easily moved with the tip. Atomically resolved images obtained at negative sample bias show that the vanadium induced features occupy oxygen-hollow sites on the ceria surface as shown in 5.26 b.

The situation changes when the system is subjected to a mild annealing in an oxygen background (400 K and 5 x 10^{-7} mbar O_2). STM images reveal that the features are stabilized and can readily be imaged. Features of different sizes are identified on images such as 5.27 a-c. For the stabilized features atomic resolution was obtained at positive sample bias, therefore it is assumed that the cerium sublattice is imaged. The features are found to sit on cerium-hollow positions.
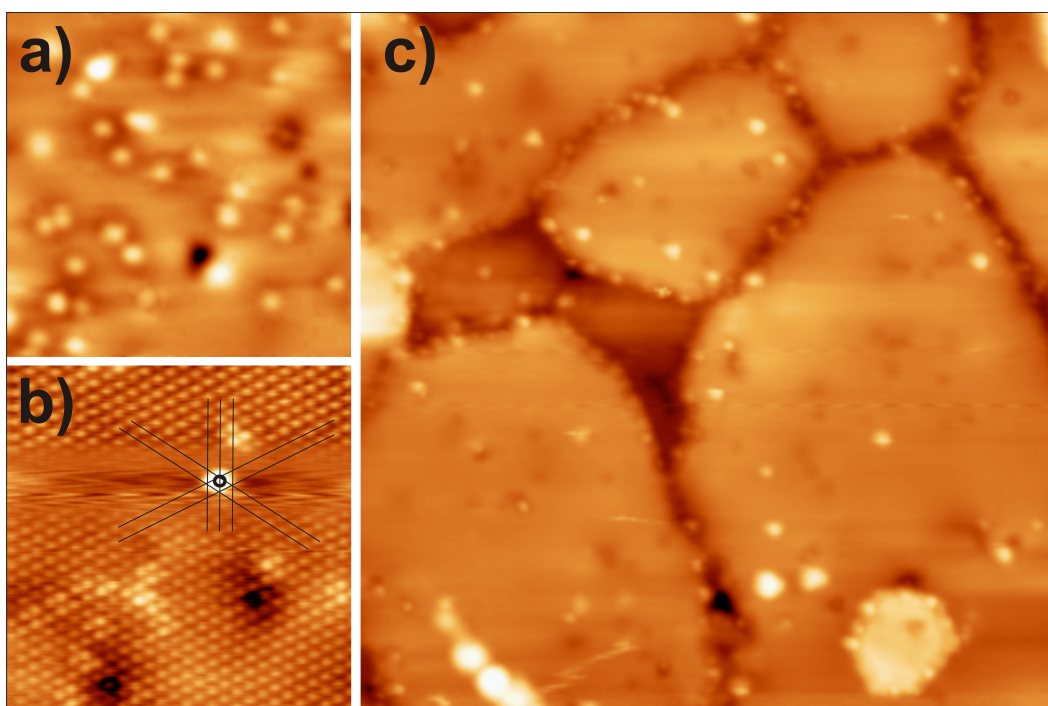

Figure 5.27: (a) Single V induced features on the ceria film after stabilizing in 5 x 10^{-7} mbar O_2 at 400 K (3.0 V, 15 x 15 nm^2). (b) Same situation as (a) with atomic resolution of the Ce sublattice (2.2 V, 10 x 10 nm^2). (c) Overview image with stable V induced features (4.0 V 50 x 50 nm^2).

Those observations can be understood in terms of oxidizing the vanadium species to vanadia on the ceria film. In turn, for the case of unstable vanadium after deposition at low temperature in UHV it is deduced that vanadium is not oxidized and therefore unstable on the ceria surface. It can be ruled out, at least for low temperatures, that the vanadium removes oxygen from the ceria surface in order to form stable V_xO_y

compounds. The stabilization upon annealing in oxygen is consequently assigned to an oxygen uptake from the gas phase that stabilizes vanadia species on the surface. This is accordance with theoretical results showing a strong binding of vanadia species on the ceria surface [227].

Those findings are further corroborated by experiments where the vanadium is evaporated onto the surface in an oxygen background. The corresponding experiments are described in the next section.

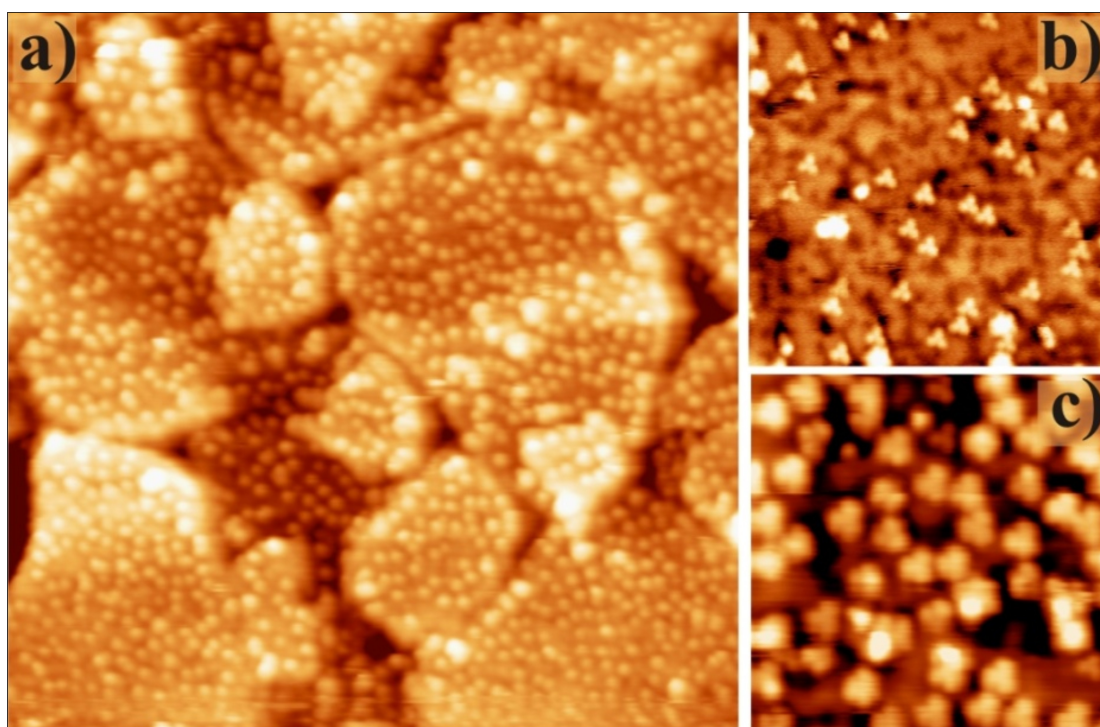### 5.3.1 Self-Organization of Magic Vanadia Clusters on Ceria

Figure 5.28: Assembly of V_xO_y features on the ceria surface after depositing vanadium in oxygen and annealing to 700 K. (a) Overview image with a coverage of 7 x 10^{13} vanadium atoms per cm^2 (5.0 V, 80 x 80 nm^2). (b) Zoom-in at coverage of 2 x 10^{13} vanadium atoms per cm^2 (5.2 V, 20 x 20 nm^2), the trimers are the most abundant species. (c) Zoom-in at coverage of 7 x 10^{13} vanadium atoms per cm^2 (3.8 V, 15 x 15 nm^2), the heptamers dominate the image.

A different situation is observed when vanadium is directly deposited at higher temperatures in an oxygen background. After evaporating vanadium at room temperature in 5 x 10^{-7} mbar O_2 and subsequent annealing to 700 K in the same oxygen background larger vanadia features are formed and a distinct formation of trimers and heptamers

is observed. As shown in figure 5.28 a the oxide surface is homogeneously covered with monolayer V_xO_y species. Closer inspection reveals that all features adapt a similar structure. At images taken after evaporation of about 2×10^{13} vanadium atoms per cm^2, such as 5.28 b, all features display a triangular shape and are therefore assigned to vanadia trimers. At higher coverage of about 7×10^{13} vanadium atoms per cm^2, as shown in figure 5.28 b, the features adopt a rather uniform, hexagonal structure which is assigned to vanadia heptamers. These structures of vanadia on ceria have been observed before by Baron *et. al.* [227]. On zoom-in images such as 5.29 b, atomic positions can be assigned for different vanadia features found on the surface. It is interesting to note that upon increasing coverages the density of heptamers increases while the density of trimers decreases but no intermediate or larger structures are observed.
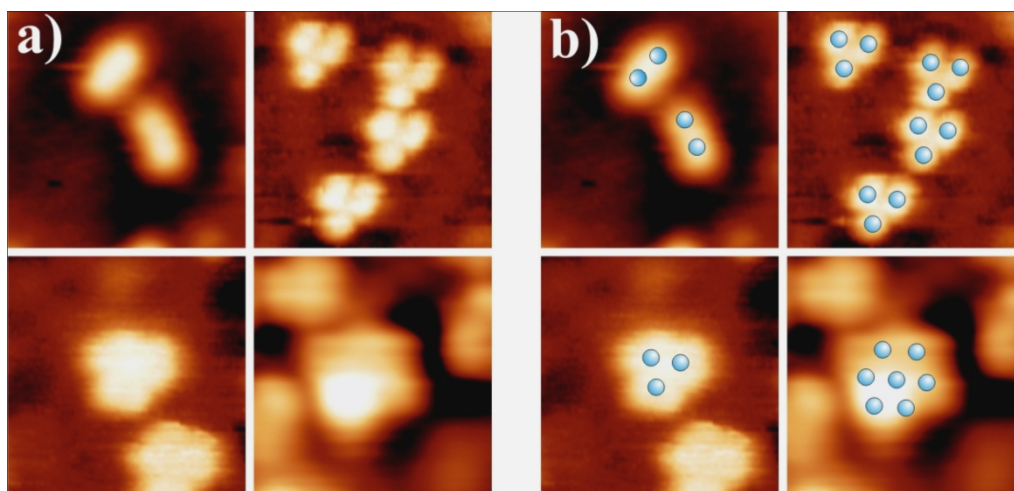

Figure 5.29: (a) Close up STM images of V_xO_y features on the ceria surface formed upon stabilization of increasing amounts of vanadium on the oxide surface (all 4 x 4 nm^2 and increasing coverage of vanadium of 5×10^{12}, 2×10^{13}, 5×10^{13}), 7×10^{13} V-atoms per cm^2.

Apparently those two different configurations represent energetically distinct structures that are more stable than other possible features. Therefore the observed features may be regarded as oxide molecules that form very defined and stable configurations similar to gas phase compounds that preferably agglomerate to magic clusters [252]. A similar behavior has been found for two-dimensional vanadia clusters on a rhodium(111) surface, which form hexameric structures with six vanadium and twelve oxygen atoms [253–255]. In contrast to these observations, where the hexagonal rings eventually connect and form a honeycomb structure, the vanadia features on ceria do not coalesce. Even for higher coverages the heptamers stay well separated and keep an almost uniform distance of 2.2 ± 0.3 nm as observed in figure 5.28 a. This difference might be explained by the presence of the oxide film. The repulsive interaction between the adspecies could be mediated by the perturbed electronic structure of the oxide film but in principle also charging effects might occur on the insulating oxide.

5.4 Conclusions

The STM is a powerful tool to gain microscopic and spectroscopic insight into morphological and electronical properties of surfaces. In this chapter this has been demonstrated for the case of ceria grown on a ruthenium single crystal. The morphological properties of thin ceria films were discussed, providing an atomistic model of the observed Moiré pattern as well as atomic resolution of different point and line defects. Beyond that the growth and distribution of ceria ad-islands on the film was discussed.

Stabilizing the tip in the ceria band gap opens a possibility to tunnel into empty and filled Ce *4f*-states and thus provides a unique, local probe of the reduction state of ceria. Experimental STM data was combined with complementary DFT calculations in order to shed light on the localization of two excess electrons that are released upon oxygen vacancy formation in the $CeO_2(111)$ surface. It could be shown that the two associated Ce^{3+} ions can occupy different coordination spheres around the defect. The exact positions of the reduced ions could be determined from atomically resolved images.

The spectroscopy determining the reduction state could also be applied to structural defects of the ceria film yielding local insight into the localization of filled *f*-states at edges and defects.

Clear signs of a changed electronic structure were found for globally reduced films. The two methods for reduction that have been explored are UHV annealing and electron injection from the tip. Both methods proved to yield the same effect on the electronic structure, namely a redshift of the band gap with respect to the ruthenium Fermilevel. It has been demonstrated that the STM-tip is well suited to induce a locally confined reduction.

Also the special electronic properties of the different step edges of ceria islands on the film have been discussed and explained in terms of dipole formation at certain edges.

This chapter provides a comprehensive and coherent description of local electronic behavior of ceria thin films from an STM perspective.

In the last section of this chapter, some results on vanadium adsorption on ceria are presented. It has been demonstrated that vanadium forms small unstable features on the ceria surface after deposition at 10 K in UHV. Only upon annealing in oxygen a stabilization of the vanadium, which is associated to an oxidation to vanadia, is observed.

Larger coverages of vanadium deposited in oxygen lead to the formation of stable and uniform features: depending on the coverage trimers and heptamers are observed but no intermediate or bigger features. The experiments on the vanadium adsorption constitute only the low-temperature STM perspective of the system. In order to draw further conclusions more input from theory and further spectroscopic data is required.

6 Conclusions and Outlook

This thesis was aimed at investigating and manipulating thin oxide films on metal surfaces. Two model systems have been studied using the scanning tunneling microscope with its powerful microscopic and spectroscopic capabilities.

The first big part of this thesis deals with the unique and very interesting properties of a mono layer film of silica (SiO_2) grown on molybdenum. For this system it could be shown that lithium atoms penetrate into the rings of the porous structure and bind to the interface. In a very productive interplay between experiment and theory fascinating new properties of the modified system were revealed: the dipole induced by the positive lithium ions at the interface leads to a workfunction reduction of the whole system. This completely changes the adsorption properties of the system and renders it susceptible to gold adsorption which was not possible before. Herewith a new method to tailor the adsorption properties has been demonstrated for one specific model system, however the extension to other metal-oxide systems seems feasible.

Furthermore the surprising properties of lithium at the metal oxide interface were described and explained in terms of a substrate mediated self organization behavior.

Beyond that it has been demonstrated that the mono layer silica film provides a suitable oxide-matrix to stabilize single atomic magnetic units. It is shown that the iron monomers are strongly bound to interfacial adsorption sites where they are well protected against thermal diffusion, aggregation and unwanted chemical reactions. By exploiting a Kondo-type conductance anomaly it is shown that they retain a magnetic moment.

In the second part of this thesis thin ceria (CeO_2) films grown on a ruthenium single crystal have been investigated. Special attention has been devoted to the defect structure of this catalytically relevant rare earth oxide. Several morphologic aspects of the system, such as a Moiré pattern at the interface, different islands types and line defects, have been explored and explained in terms of atomic models. A big step in the understanding of this complex system has been taken by directly relating the presence of defects to local changes in the electronic structure. Demonstrating the amazing capabilities of STM, a direct and local prove of filled cerium *4f*-states in the vicinity of surface oxygen vacancies is given. Again with the interplay of theory and experiment even the exact localization of the extra charges left behind upon vacancy creation could be identified. This allows a direct and local probe of the reduction state of ceria.

Beyond that also the electronic properties of different structural and line defects are investigated, elucidating the relationship between morphology and electronic structure of individual lattice irregularities.

All results presented in this thesis constitute promising starting points for new experiments and further calculations. On the way to a comprehensive understanding of thin oxide films many aspects remain to be addressed and additional riddles to be solved.
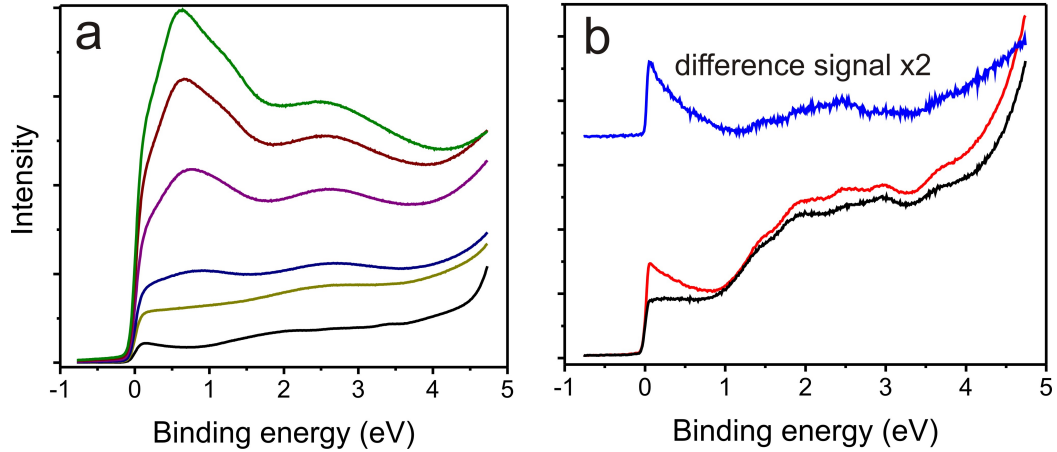

Figure 6.1: (a) Photoemission spectra of increasing amounts of Fe at the silica/Mo(112) interface, curves from bottom to top have been take for a nominal coverage of 0; 0.175, 0.25, 0.5, 1.0, 2.0 mono layers of Fe. (b) Photoemission spectra taken at 20 K with (red curve) and without Fe (black curve) in the silica matrix. The blue curve represents the difference of the two other signals and is enlarged by a factor of 2 for clarity.

Some of the more obvious next steps for the thin silica film include incorporation of defects by preparing films with titanium or aluminum impurity atoms, loading the pores with different atoms and preparing thicker, crystalline silica films. The last point has already been approached by researchers from the department of chemical physics of the Fritz-Haber-Institut by preparing a crystalline bi-layer silica film on a ruthenium single crystal [256]. However recipes for crystalline multi-layer silica films are still not available.

The method to tailor the adsorption properties of oxide films by work function tuning described in this thesis could also be applied to other systems such as magnesia (MgO) or titania (TiO_2), opening new, interesting possibilities to produce a versatile class of new materials.

The promising results on the storage of single atomic magnetic units in the silica-matrix already prompted first, preliminary photoemission experiments performed at the ELETTRA synchrotron in Trieste, Italy in collaboration with Dr. Dinesh Topwal and Prof. Dr. Carlo Carbone. As shown in figure 6.1 the incorporation of iron into the silica matrix leads to the appearance of new features in the recorded photoemission signal that relate to the iron abundance. Also a distinct peak close to the Fermi-level is observed at low temperatures which might be a sign of the Kondo resonance and therewith a proof for the magnetic properties of the embedded iron atoms. Yet further

experiments, for example employing magnetic dichroism, and theory are needed before new conclusions can be drawn [151].

Also the ceria system offers a wide range of promising new experiments based on the body of results obtained in this thesis. The unmatched spatial sensitivity of the STM can now be combined with the known spectroscopic fingerprint for ceria reduction: the filled cerium $4f$-states. This new possibility could provide new local insights into the adsorption of catalytically active species, such as vanadium or gold nanoparticles on the oxide film. The STM could hereby help to clarify charge transfer processes between adsorbates and the reducible oxide at the atomic scale.

Beyond that the capability to probe spatially confined atomic orbitals with the STM could be applied to other systems with a large band gap. A possibility would be to dope known wide band gap oxides, such as magnesia or silica with rare earth elements such as cerium or europium and probe the position of the confined f-states of the systems. Atomic scale knowledge on doped oxide films is not only mandatory to understand the unique optical activity of such systems, e.g. in solid state lasers, but is also of relevance for gaining insights into their catalytic performance. The STM and its spectroscopic applications will be of utmost importance when addressing such questions in the future, especially if it is combined with other non-local spectroscopies in particular photoelectron spectroscopy and vibrational spectroscopy.

Bibliography

[1] H.-J. Freund. Introductory lecture: Oxide surfaces. *Faraday Discussions*, 114:1–31, 1999.

[2] H.-J. Freund. Metal-supported ultrathin oxide film systems as designable catalysts and catalyst supports. *Surface Science*, 601:1438–1442, 2007.

[3] H.-J. Freund. Model Studies in Heterogeneous Catalysis. *Chemistry - a European Journal*, 16:9384–9397, 2010.

[4] H.-J. Freund, H. Kuhlenbeck, J. Libuda, G. Rupprechter, M. Bäumer, H. Hamann. Bridging the pressure and materials gaps between catalysis and surface science: clean and modified oxide surfaces. *Topics in Catalysis*, 15:201–209, 2001.

[5] N. Nilius. Properties of oxide thin films and their adsorption behavior studied by scanning tunneling microscopy and conductance spectroscopy. *Surface Science Reports*, 64:595–659, 2009.

[6] C. T. Campbell. Ultrathin metal films and particles on oxide surfaces: structural, electronic and chemisorptive properties. *Surface Science Reports*, 27:1–111, 1997.

[7] D. W. Goodman. Model Catalysts - from Extended Single-Crystals to Supported Particles. *Surface Review and Letters*, 2:9–24, 1995.

[8] C. R. Henry. Surface studies of supported model catalysts. *Surface Science Reports*, 31:231–325, 1998.

[9] S. A. Chambers. Epitaxial growth and properties of thin film oxides. *Surface Science Reports*, 39:105–180, 2000.

[10] H.-J. Freund. Models for oxidation catalyst: Characterization and reaction at the atomic level. *Catalysis Today*, 117:6–14, 2006.

[11] G. Kresse, M. Schmid, E. Napetschnig, M. Shishkin, L. Kohler, P. Varga. Structure of the ultrathin aluminum oxide film on NiAl(110). *Science*, 308:1440–1442, 2005.

[12] M. Sterrer, T. Risse, U. Martinez Pozzoni, L. Giordano, M. Heyde, H. P. Rust, G. Pacchioni, H.-J. Freund. Control of the Charge State of Metal Atoms on Thin MgO Films. *Physical Review Letters*, 98:096107, 2007.

[13] U. Martinez, J.-F. Jerratsch, N. Nilius, L. Giordano, G. Pacchioni, H.-J. Freund. Tailoring the Interaction Strength between Gold Particles and Silica Thin Films via Work Function Control. *Physical Review Letters*, 103:056801, 2009.

[14] Y.-N. Sun, Z.-H. Qin, M. Lewandowski, E. Carrasco, M. Sterrer, S. Shaikhutdinov, H.-J. Freund. Monolayer iron oxide film on platinum promotes low temperature co oxidation. *Journal of Catalysis*, 266:359 –368, 2009.

[15] B. M. Weckhuysen, D. E. Keller. Chemistry, spectroscopy and the role of supported vanadium oxides in heterogeneous catalysis. *Catalysis Today*, 78:25–46, 2003.

[16] I. E. Wachs. Recent conceptual advances in the catalysis science of mixed metal oxide catalytic materials. *Catalysis Today*, 100:79–94, 2005.

[17] M. A. Banares. Supported metal oxide and other catalysts for ethane conversion: a review. *Catalysis Today*, 51:319–348, 1999.

[18] T. Blasco, J. M. L. Nieto. Oxidative dehydrogenation of short chain alkanes on supported vanadium oxide catalysts. *Applied Catalysis A-General*, 157:117–142, 1997.

[19] H. J. Schellnhuber. Earth system analysis and the second Copernican revolution. *Nature*, 402:C19–C23, 1999.

[20] E. Abbe. Beiträge zur Theorie des Mikroskops und der Mikroskopischen Wahrnehmung. *Archiv für Mikroskopische Anatomie*, 9:413–468, 1873.

[21] E. Ruska. The Development of the Electron-Microscope and of Electron-Microscopy. *Reviews of Modern Physics*, 59:627–638, 1987.

[22] R. Young, J. Ward, F. Scire. Topografiner - Instrument for Measuring Surface Microtopography. *Review of Scientific Instruments*, 43:999, 1972.

[23] G Binnig, H Rohrer, C Gerber, E Weibel. Tunneling Through A Controllable Vacuum Gap. *Applied Physics Letters*, 40:178–180, 1982.

[24] R. Wiesendanger, editor. *Scanning Probe Microscopy and Spectroscopy: Analytical Methods*. Springer-Verlag, Berlin, Heidelberg, 1998.

[25] C. J. Chen. *Introduction to Scanning Tunneling Microscopy*. Oxford University Press, New York, Oxford, 1993.

[26] R. Wiesendanger, H. J. Guntherodt, G. Guntherodt, R. J. Gambino, R. Ruf. Observation of Vacuum Tunneling of Spin-Polarized Electrons with the Scanning Tunneling Microscope. *Physical Review Letters*, 65:247–250, 1990.

[27] B. C. Stipe, M. A. Rezaei, W. Ho. Single-molecule vibrational spectroscopy and microscopy. *Science*, 280:1732–1735, 1998.

[28] J. H. Coombs, J. K. Gimzewski, B. Reihl, J. K. Sass, R. R. Schlittler. Photon-Emission Experiments with the Scanning Tunnelling Microscope. *Journal of Microscopy-Oxford*, 152:325–336, 1988.

[29] N. Nilius, N. Ernst, H.-J. Freund. Photon emission spectroscopy of individual oxide-supported sliver clusters in a scanning tunneling microscope. *Physical Review Letters*, 84:3994–3997, 2000.

[30] J. I. Pascual, J. Méndez, J. Gómez-Herrero, A. M. Baró, N. García, Vu Thien Binh. Quantum contact in gold nanostructures by scanning tunneling microscopy. *Physical Review Letters*, 71:1852–1855, 1993.

[31] L. Limot, J. Kröger, R. Berndt, A. Garcia-Lekue, W. A. Hofer. Atom transfer and single-adatom contacts. *Physical Review Letters*, 94:126102, 2005.

[32] V. M. Hallmark, S. Chiang, J. F. Rabolt, J. D. Swalen, R. J. Wilson. Observation of Atomic Corrugation on Au(111) by Scanning Tunneling Microscopy. *Physical Review Letters*, 59:2879–2882, 1987.

[33] H. M. Benia. *Spatially Resolved Optical Measurements on Supported Metal Particles and Oxide Surfaces with the STM*. PhD thesis, Humboldt-Universität zu Berlin, 2008.

[34] M. F. Crommie, C. P. Lutz, D. M. Eigler. Imaging Standing Waves in a 2-Dimensional Electron-Gas. *Nature*, 363:524–527, 1993.

[35] Y. Hasegawa, P. Avouris. Direct Observation of Standing-Wave Formation at Surface Steps using Scanning Tunneling Spectroscopy. *Physical Review Letters*, 71:1071–1074, 1993.

[36] J. T. Li, W. D. Schneider, R. Berndt. Local density of states from spectroscopic scanning-tunneling-microscope images: Ag(111). *Physical Review B*, 56:7656–7659, 1997.

[37] R. M. Feenstra, W. A. Thompson, A. P. Fein. Real-Space Observation of Pi-Bonded Chains and Surface Disorder on Si(111)2x1. *Physical Review Letters*, 56:608–611, 1986.

[38] H. F. Hess, R. B. Robinson, R. C. Dynes, J. M. Valles, J. V. Waszczak. Scanning-Tunneling-Microscope Observation of the Abrikosov Flux Lattice and the Density of States near and inside a Fluxoid. *Physical Review Letters*, 62:214–216, 1989.

[39] M. F. Crommie, C. P. Lutz, D. M. Eigler. Spectroscopy of a Single Adsorbed Atom. *Physical Review B*, 48:2851–2854, 1993.

[40] W. D. Tian, S. Datta, S. H. Hong, R. Reifenberger, J. I. Henderson, C. P. Kubiak. Conductance spectra of molecular wires. *Journal of Chemical Physics*, 109:2874–2882, 1998.

[41] J. Viernow, D. Y. Petrovykh, A. Kirakosian, J. L. Lin, F. K. Men, M. Henzler, F. J. Himpsel. Chemical imaging of insulators by STM. *Physical Review B*, 59:10356–10361, 1999.

[42] J.-F. Jerratsch, N. Nilius, H.-J. Freund, U. Martinez, L. Giordano, G. Pacchioni. Lithium incorporation into a silica thin film: Scanning tunneling microscopy and density functional theory. *Physical Review B*, 80:245423, 2009.

[43] J. A. Stroscio, R. M. Feenstra, A. P. Fein. Electronic-Structure of the Si(111) 2x1 Surface by Scanning-Tunneling Microscopy. *Physical Review Letters*, 57:2579–2582, 1986.

[44] W. J. Kaiser, R. C. Jaklevic. Spectroscopy of Electronic States of Metals with a Scanning Tunneling Microscope. *Ibm Journal of Research and Development*, 30:411–416, 1986.

[45] T. Jung, Y. W. Mo, F. J. Himpsel. Identification of Metals in Scanning-Tunneling-Microscopy via Image States. *Physical Review Letters*, 74:1641–1644, 1995.

[46] R. S. Becker, J. A. Golovchenko, B. S. Swartzentruber. Electron Interferometry at Crystal-Surfaces. *Physical Review Letters*, 55:987–990, 1985.

[47] G. Binnig, K. H. Frank, H. Fuchs, N. Garcia, B. Reihl, H. Rohrer, F. Salvan, A. R. Williams. Tunneling Spectroscopy and Inverse Photoemission - Image and Field States. *Physical Review Letters*, 55:991–994, 1985.

[48] J. I. Pascual, N. Lorente, Z. Song, H. Conrad, H. P. Rust. Selectivity in vibrationally mediated single-molecule chemistry. *Nature*, 423:525–528, 2003.

[49] R. Wiesendanger. *Scanning Probe Microscopy and Spectroscopy: Methods and Applications*. Cambridge University Press, 1994.

[50] J. Tersoff, D. R. Hamann. Theory and Application for the Scanning Tunneling Microscope. *Physical Review Letters*, 50:1998–2001, 1983.

[51] J. Tersoff, D. R. Hamann. Theory of the Scanning Tunneling Microscope. *Physical Review B*, 31:805–813, 1985.

[52] J. Bardeen. Tunnelling from a Many-Particle Point of View. *Physical Review Letters*, 6:57, 1961.

[53] C. J. Chen. Origin of Atomic Resolution on Metal-Surfaces in Scanning Tunneling Microscopy. *Physical Review Letters*, 65:448–451, 1990.

[54] M. R. Castell, S. L. Dudarev, C. Muggelberg, A. P. Sutton, G. A. D. Briggs, D. T. Goddard. Microscopy of metal oxide surfaces. *Microscopy and Microanalysis*, 6:324–328, 2000.

[55] D. A. Bonnell. Scanning tunneling microscopy and spectroscopy of oxide surfaces. *Progress In Surface Science*, 57:187–252, 1998.

[56] U. Diebold. The surface science of titanium dioxide. *Surface Science Reports*, 48:53–229, 2003.

[57] S. Schintke, W. D. Schneider. Insulators at the ultrathin limit: electronic structure studied by scanning tunnelling microscopy and scanning tunnelling spectroscopy. *Journal of Physics-Condensed Matter*, 16:R49–R81, 2004.

[58] T. Bertrams, A. Brodde, H. Neddermeyer. Tunneling through an Epitaxial Oxide Film - Al_2O_3 on NiAl(110). *Journal of Vacuum Science and Technology B*, 12:2122–2124, 1994.

[59] W. Hebenstreit, J. Redinger, Z. Horozova, M. Schmid, R. Podloucky, P. Varga. Atomic resolution by STM on ultra-thin films of alkali halides: experiment and local density calculations. *Surface Science*, 424:L321–L328, 1999.

[60] S. Schintke, S. Messerli, M. Pivetta, F. Patthey, L. Libioulle, M. Stengel, A. De Vita, W.D. Schneider. Insulator at the ultrathin limit: MgO on Ag(001). *Physical Review Letters*, 87:276801, 2001.

[61] M. Bäumer, H.-J. Freund. Metal deposits on well-ordered oxide films. *Progress in Surface Science*, 61:127–198, 1999.

[62] N. Nilius, A. Corper, G. Bozdech, N. Ernst, H.-J. Freund. Experiments on individual alumina-supported adatoms and clusters. *Progress in Surface Science*, 67:99–121, 2001.

[63] K. H. Hansen, T. Worren, E. Laegsgaard, F. Besenbacher, I. Stensgaard. Bias dependent apparent height of an Al_2O_3 thin film on NiAl(110), and of supported Pd clusters. *Surface Science*, 475:96–102, 2001.

[64] I. Horcas, R. Fernandez, J. M. Gomez-Rodriguez, J. Colchero, J. Gomez-Herrero, A. M. Baro. WSXM: A software for scanning probe microscopy and a tool for nanotechnology. *Review of Scientific Instruments*, 78:013705, 2007.

[65] K. Besocke. An Easily Operable Scanning Tunneling Microscope. *Surface Science*, 181:145–153, 1987.

[66] G. Meyer. A simple low-temperature ultrahigh-vacuum scanning tunneling microscope capable of atomic manipulation. *Review of Scientific Instruments*, 67:2960–2965, 1996.

[67] S. Ulrich. *Design and Construction of a Low-Temperature Scanning Tunneling Microscope for Spectroscopic Applications on Model Catalysts*. PhD thesis, Technische Universität Berlin, Unpublished.

[68] H. Li, M. Eddaoudi, M. O'Keeffe, O. M. Yaghi. Design and synthesis of an exceptionally stable and highly porous metal-organic framework. *Nature*, 402:276–279, 1999.

[69] S. Y. Chou, P. R. Krauss, W. Zhang, L. J. Guo, L. Zhuang. Sub-10 nm imprint lithography and applications. *Journal of Vacuum Science and Technology B*, 15:2897–2904, 1997.

[70] G. M. Whitesides, J. P. Mathias, C. T. Seto. Molecular Self-Assembly and Nanochemistry - A Chemical Strategy for the Synthesis of Nanostructures. *Science*, 254:1312–1319, 1991.

[71] Z. J. Li, M. Jaroniec. Colloidal imprinting: A novel approach to the synthesis of mesoporous carbons. *Journal of the American Chemical Society*, 123:9208–9209, 2001.

[72] L. Tapaszto, G. Dobrik, P. Lambin, L. P. Biro. Tailoring the atomic structure of graphene nanoribbons by scanning tunnelling microscope lithography. *Nature Nanotechnology*, 3:397–401, 2008.

[73] T. Schroeder, J. B. Giorgi, A. Hammoudeh, N. Magg, M. Bäumer, H.-J. Freund. Oxygen-induced p(2x3) reconstruction on Mo(112) studied by LEED and STM. *Phys. Rev. B*, 65:115411, 2002.

[74] J. Weissenrieder, S. Kaya, J.-L. Lu, H.-J. Gao, S. Shaikhutdinov, H.-J. Freund, M. Sierka, T.K. Todorova, J. Sauer. Atomic structure of a thin silica film on a Mo(112) substrate: a two-dimensional network of SiO_4 tetrahedra. *Physical Review Letters*, 95:076103, 2005.

[75] M. S. Chen, A. K. Santra, D. W. Goodman. Structure of thin SiO_2 films grown on Mo(112). *Physical Review B*, 69:155404, 2004.

[76] T. K. Todorova, M. Sierka, J. Sauer, S. Kaya, J. Weissenrieder, J. L. Lu, H. J. Gao, S. Shaikhutdinov, H.-J. Freund. Atomic structure of a thin silica film on a Mo(112) substrate: A combined experimental and theoretical study. *Physical Review B*, 73:249902, 2006.

[77] L. Giordano, D. Ricci, G. Pacchioni, P. Ugliengo. Structure and vibrational spectra of crystalline SiO_2 ultra-thin films on Mo(112). *Surface Science*, 584:225–236, 2005.

[78] S. Kaya, M. Baron, D. Stacchiola, J. Weissenrieder, S. Shaikhutdinov, T. K. Todorova, M. Sierka, J. Sauer, H.-J. Freund. On the geometrical and electronic structure of an ultra-thin crystalline silica film grown on Mo(112). *Surface Science*, 601:4849–4861, 2007.

[79] J. Seifert, D. Blauth, H. Winter. Evidence for 2d-network structure of monolayer silica film on mo(112). *Physical Review Letters*, 103:017601, 2009.

[80] T. Schroeder, M. Adelt, B. Richter, M. Naschitzki, M. Baumer, H.-J. Freund. Epitaxial growth of SiO_2 on Mo(112). *Surface Review and Letters*, 7:7–14, 2000.

[81] S. Kaya. *Structural and Catalytic Investigations on Vanadium Oxide Nanoparticles Supported on Silica Films Grown on a Mo(112) Substrate*. PhD thesis, Humboldt-Universität zu Berlin, 2007.

[82] D. Ricci, G. Pacchioni. Structure of ultrathin crystalline SiO_2 films on Mo(112). *Physical Review B*, 69:161307, 2004.

[83] J. B. Giorgi, T. Schroeder, M. Baumer, H.-J. Freund. Study of CO adsorption on crystalline-silica-supported palladium particles. *Surface Science*, 498:L71–L77, 2002.

[84] S. Ulrich, N. Nilius, H.-J. Freund, U. Martinez, L. Giordano, G. Pacchioni. Evidence for a size-selective adsorption mechanism on oxide surfaces: Pd and Au atoms on SiO$_2$/Mo(112). *ChemPhysChem*, 9:1367–1370, 2008.

[85] S. Ulrich, N. Nilius, H.-J. Freund, U. Martinez, L. Giordano, G. Pacchioni. Realization of an atomic sieve: silica on Mo(112). *Surface Science*, 603:1145–9, 2009.

[86] S. Ulrich, N. Nilius, H.-J. Freund, U. Martinez, L. Giordano, G. Pacchioni. Modifying the Adsorption Characteristic of Inert Silica Films by Inserting Anchoring Sites. *Physical Review Letters*, 102:016102, 2009.

[87] M. Baron, D. Stacchiola, S. Ulrich, N. Nilius, S. Shaikhutdinov, H. J. Freund, U. Martinez, L. Giordano, G. Pacchioni. Adsorption of Au and Pd atoms on thin SiO$_2$ films: The role of atomic structure. *Journal of Physical Chemistry C*, 112:3405–3409, 2008.

[88] D. W. Breck. *Zeolite molecular sieves: structure, chemistry, and use.* Wiley, 1973.

[89] L. Giordano, G. Pacchioni, J. Goniakowski, N. Nilius, E. D. L. Rienks, H.-J. Freund. Charging of Metal Adatoms on Ultrathin Oxide Films: Au and Pd on FeO/Pt(111). *Physical Review Letters*, 101:026102, 2008.

[90] U. Martinez, L. Giordano, G. Pacchioni. Tuning the work function of ultrathin oxide films on metals by adsorption of alkali atoms. *Journal of Chemical Physics*, 128:164707, 2008.

[91] Ertl, G. and Knözinger, H. and Weitkamp, J., editor. *Handbook of heterogeneous catalysis, 2nd ed.* Wiley-VCH, 2008.

[92] J. H. Lunsford. The Catalytic Oxidative Coupling of Methane. *Angewandte Chemie-International Edition*, 34:970–980, 1995.

[93] M. Armand, J. M. Tarascon. Building better batteries. *Nature*, 451:652–657, 2008.

[94] H. P. Bonzel. Alkali-Metal-Affected Adsorption of Molecules on Metal-Surfaces. *Surface Science Reports*, 8:43–125, 1988.

[95] R. D. Diehl, R. McGrath. Structural studies of alkali metal adsorption and coadsorption on metal surfaces. *Surface Science Reports*, 23:43, 1996.

[96] D. M. Riffe, G. K. Wertheim, P. H. Citrin. Alkali-Metal Adsorbates on W(110) - Ionic, Covalent, or Metallic. *Physical Review Letters*, 64:571–574, 1990.

[97] S. R. Chubb, E. Wimmer, A. J. Freeman, J. R. Hiskes, A. M. Karo. All-Electron Local-Density-Functional Theory of Alkali-Metal Adsorption on Transition-Metal Surfaces - Cs on Mo(001). *Physical Review B*, 36:4112–4122, 1987.

[98] I. N. Yakovkin. Monte-Carlo Simulation of Order-Disorder Transitions in Linear Structures of Alkali and Alkaline-Earth Adsorbates. *Surface Science*, 282:195–201, 1993.

[99] I. N. Yakovkin. Atomic wires on furrowed transition metal surfaces. *Journal of Nanoscience and Nanotechnology*, 1:357–374, 2001.

[100] A. Fedorus, D. Kolthoff, V. Koval, I. Lyuksyutov, A. G. Naumovets, H. Pfnür. Phase transitions in the adsorption system Li/Mo(112). *Physical Review B*, 62:2852–2861, 2000.

[101] G. Doyen, D. Drakova, J. V. Barth, R. Schuster, T. Gritsch, R. J. Behm, G. Ertl. Scanning-Tunneling-Microscope Imaging of Clean and Alkali-Metal-Covered Cu(110) and Au(110) Surfaces. *Physical Review B*, 48:1738–1749, 1993.

[102] J. Kliewer, R. Berndt. Low temperature scanning tunneling microscopy of Na on Cu(111). *Surface Science*, 477:250–258, 2001.

[103] I. Langmuir, K. H. Kingdon. Thermionic effects caused by alkali vapors in vacuum tubes. *Science*, 57:58–60, 1923.

[104] I. Langmuir. Vapor pressures, evaporation, condensation and adsorption. *Journal of the American Chemical Society*, 54:2798–2832, 1932.

[105] R. W. Gurney. Theory of electrical double layers m adsorbed films. *Physical Review*, 47:479–482, 1935.

[106] J. Friedel. Metallic alloys. *Nuovo Cimento*, 7:287–311, 1958.

[107] T. Einstein. *Physical Structure of Solid Surfaces*. Elsevier, 1996.

[108] R. Casanova, T. T. Tsong. Pair Interaction of Metal Atoms on a Metal-Surface. *Physical Review B*, 22:5590–5598, 1980.

[109] T. T. Tsong, R. Casanova. Direct Measurement of Pair Energies in Adatom-Adatom Interactions on a Metal-Surface. *Physical Review B*, 24:3063–3072, 1981.

[110] V. Simic-Milosevic, M. Heyde, N. Nilius, M. Nowicki, H.-P. Rust, H.-J. Freund. Substrate-mediated interaction and electron-induced diffusion of single lithium atoms on Ag(001). *Physical Review B*, 75:195416, 2007.

[111] J. Repp, F. Moresco, G. Meyer, K. H. Rieder, P. Hyldgaard, M. Persson. Substrate mediated long-range oscillatory interaction between adatoms: Cu/Cu(111). 85:2981–2984, 2000.

[112] I. N. Yakovkin. Self-consistent electronic structure of the Mo(112) surface. *Surface Science*, 389:48–54, 1997.

[113] Z. D. Zhang, D. N. Mcilroy, P. A. Dowben. Changes in Electron Localization and Density-of-States Near E_F across the Nonmetal-Metal Transition in Mg Overlayers. *Physical Review B*, 49:13780–13786, 1994.

[114] A. Kiejna, R. M. Nieminen. First-principles calculation of Li adatom structures on the Mo(112) surface. *Physical Review B*, 66:85407, 2002.

[115] N. F. Mott. Charged Defects in Vitreous Silica .1. Electrical-Properties. *Journal of non-Crystalline Solids*, 40:1–6, 1980.

[116] J. Hoelz, F. K. Schulte. *Work Function of Metals*. Springer-Verlag, Berlin, 1979.

[117] J. Bansmann, S. H. Baker, C. Binns, J. A. Blackman, J. P. Bucher, J. Dorantes-Davila, V. Dupuis, L. Favre, D. Kechrakos, A. Kleibert, K. H. Meiwes-Broer, G. M. Pastor, A. Perez, O. Toulemonde, K. N. Trohidou, J. Tuaillon, Y. Xie. Magnetic and structural properties of isolated and assembled clusters. *Surface Science Reports*, 56:189–275, 2005.

[118] W. Schindler, D. Hofmann, J. Kirschner. Nanoscale electrodeposition: A new route to magnetic nanostructures? *Journal of Applied Physics*, 87:7007–7009, 2000.

[119] C. Noguez. Optical properties of isolated and supported metal nanoparticles. *Optical Materials*, 27:1204–1211, 2005.

[120] M. Haruta. Size- and support-dependency in the catalysis of gold. *Catalysis Today*, 36:153–166, 1997.

[121] T. Risse, S. Shaikhutdinov, N. Nilius, M. Sterrer, H.-J. Freund. Gold supported on thin oxide films: From single atoms to nanoparticles. *Accounts of Chemical Research*, 41:949–956, 2008.

[122] I. Yudanov, G. Pacchioni, K. Neyman, N. Rosch. Systematic density functional study of the adsorption of transition metal atoms on the MgO(001) surface. *Journal of Physical Chemistry B*, 101:2786–2792, 1997.

[123] P. A. Cox Victor E. Henrich. *The surface science of metal oxides*. Cambridge University Press, 1996.

[124] G. Pacchioni, L. Giordano, M. Baistrocchi. Charging of metal atoms on ultrathin MgO/Mo(100) films. *Physical Review Letters*, 94:226104, 2005.

[125] L. Giordano, F. Cinquini, G. Pacchioni. Tuning the surface metal work function by deposition of ultrathin oxide films: Density functional calculations. *Physical Review B*, 73:045414, 2006.

[126] P. Frondelius, H. Hakkinen, K. Honkala. Adsorption of gold clusters on metal-supported MgO: Correlation to electron affinity of gold. *Physical Review B*, 76:073406, 2007.

[127] D. Ricci, A. Bongiorno, G. Pacchioni, U. Landman. Bonding trends and dimensionality crossover of gold nanoclusters on metal-supported MgO thin films. *Physical Review Letters*, 97:036106, 2006.

[128] M. Sterrer, T. Risse, M. Heyde, H. P. Rust, H.-J. Freund. Crossover from three-dimensional to two-dimensional geometries of Au nanostructures on thin MgO(001) films: A confirmation of theoretical predictions. *Physical Review Letters*, 98:206103, 2007.

[129] N. Nilius, M. V. Ganduglia-Pirovano, V. Brazdova, M. Kulawik, J. Sauer, H.-J. Freund. Counting electrons transferred through a thin alumina film into Au chains. *Physical Review Letters*, 100:096802, 2008.

[130] N. Nilius, E. D. L. Rienks, H. P. Rust, H.-J. Freund. Self-organization of gold atoms on a polar FeO(111) surface. *Physical Review Letters*, 95:066101, 2005.

[131] L. Giordano, G. Pacchioni, J. Goniakowski, N. Nilius, E. D. L. Rienks, H.-J. Freund. Charging of metal adatoms on ultrathin oxide films: Au and pd on FeO/Pt(111). *Physical Review Letters*, 101:026102, 2008.

[132] L. Giordano, A. Del Vitto, G. Pacchioni. Au and Pd atoms adsorbed on pure and Ti-doped SiO_2/Mo(112) films. *Journal of Chemical Physics*, 124:034701, 2006.

[133] B. K. Min, W. T. Wallace, A. K. Santra, D. W. Goodman. Role of defects in the nucleation and growth of Au nanoclusters on SiO_2 thin films. *Journal of Physical Chemistry B*, 108:16339–16343, 2004.

[134] J. Repp, G. Meyer, F. E. Olsson, M. Persson. Controlling the charge state of individual gold adatoms. *Science*, 305:493–495, 2004.

[135] G. E. Moore. Cramming more components onto integrated circuits (Reprinted from *Electronics*, pg 114-117, April 19, 1965). *Proceedings of the IEEE*, 86:82–85, 1998.

[136] G Binasch, P Grünberg, F Saurenbach, W Zinn. Enhanced Magnetoresistance In Layered Magnetic-Structures With Antiferromagnetic Interlayer Exchange. *Physical Review B*, 39:4828–4830, 1989.

[137] J. Zhang, D. Repetto, V. Sessi, J. Honolka, A. Enders, K. Kern. Magnetism of Fe clusters formed by buffer-layer assisted growth on Pt(997). *European Physical Journal D*, 45:515–520, 2007.

[138] P. Gambardella, S. Rusponi, M. Veronese, S. S. Dhesi, C. Grazioli, A. Dallmeyer, I. Cabria, R. Zeller, P. H. Dederichs, K. Kern, C. Carbone, H. Brune. Giant magnetic anisotropy of single cobalt atoms and nanoparticles. *Science*, 300:1130–1133, 2003.

[139] A. J. Heinrich, J. A. Gupta, C. P. Lutz, D. M. Eigler. Single-atom spin-flip spectroscopy. *Science*, 306:466–469, 2004.

[140] C. F. Hirjibehedin, C.-Y. Lin, A. F. Otte, M. Ternes, C. P. Lutz, B. A. Jones, A. J. Heinrich. Large magnetic anisotropy of a single atomic spin embedded in a surface molecular network. *Science*, 317:1199–1203, 2007.

[141] A. D. Zhao, Q. X. Li, L. Chen, H. J. Xiang, W. H. Wang, S. Pan, B. Wang, X. D. Xiao, J. L. Yang, J. G. Hou, Q. S. Zhu. Controlling the Kondo effect of an adsorbed magnetic ion through its chemical bonding. *Science*, 309:1542–1544, 2005.

[142] L. Gao, W. Ji, Y. B. Hu, Z. H. Cheng, Z. T. Deng, Q. Liu, N. Jiang, X. Lin, W. Guo, S. X. Du, W. A. Hofer, X. C. Xie, H.-J. Gao. Site-specific Kondo effect at ambient temperatures in iron-based molecules. *Physical Review Letters*, 99:106402, 2007.

[143] J.-F. Jerratsch, N. Nilius, D. Topwal, U. Martinez, L. Giordano, H.-J. Pacchioni, G. Freund. Stabilizing Monomeric Iron Species in a Porous Silica/Mo(112) Film. *ACS Nano*, 4:863–868, 2010.

[144] All DFT calculations for this chapter have been performed by the workgroup of Prof. G. Pacchioni from the University of Milano-Bicocca.

[145] J. Kondo. Resistance Minimum in Dilute Magnetic Alloys. *Progress of Theoretical Physics*, 32:37, 1964.

[146] J. T. Li, W. D. Schneider, R. Berndt, B. Delley. Kondo scattering observed at a single magnetic impurity. *Physical Review Letters*, 80:2893–2896, 1998.

[147] V. Madhavan, W. Chen, T. Jamneala, M. F. Crommie, N. S. Wingreen. Tunneling into a single magnetic atom: Spectroscopic evidence of the Kondo resonance. *Science*, 280:567–569, 1998.

[148] V. Madhavan, W. Chen, T. Jamneala, M. F. Crommie, N. S. Wingreen. Local spectroscopy of a Kondo impurity: Co on Au(111). *Physical Review B*, 64:165412, 2001.

[149] P. Wahl, L. Diekhoner, M. A. Schneider, L. Vitali, G. Wittich, K. Kern. Kondo temperature of magnetic impurities at surfaces. *Physical Review Letters*, 93:176603, 2004.

[150] U. Fano. Effects of Configuration Interaction on Intensities and Phase Shifts. *Physical Review*, 124:1866, 1961.

[151] D. Topwal, M. Unnikrishnan, S. Gardonio, J.-F. Jerratsch, N Nilius, C. Carbone. Iron atoms in a porous silca film grown on Mo(112) investigated with photoelectron emission spectroscopy. *In preparation*.

[152] X. D. Wu, R. C. Dye, R. E. Muenchausen, S. R. Foltyn, M. Maley, A. D. Rollett, A. R. Garcia, N. S. Nogar. Epitaxial CeO_2 Films as Buffer Layers for High-Temperature Superconducting Thin-Films. *Applied Physics Letters*, 58:2165–2167, 1991.

[153] R. P. Netterfield, W. G. Sainty, P. J. Martin, S. H. Sie. Properties of CeO_2 Thin-Films Prepared by Oxygen-Ion-Assisted Deposition. *Applied Optics*, 24:2267–2272, 1985.

[154] A. G. Frangoul, K. B. Sundaram, P. F. Wahid. The Fabrication of Metal-Oxide Semiconductor Transistors using Cerium Dioxide as a Gate Oxide Material. *Journal of Vacuum Science and Technology B*, 9:181–183, 1991.

[155] Z. T. Aldhhan, C. A. Hogarth. Electrical-Conduction in Thin-Films of CeO_2 and GeO_2. *Journal of Materials Science*, 23:2205–2212, 1988.

[156] T. Inoue, M. Osonoe, H. Tohda, M. Hiramatsu, Y. Yamamoto, A . Yamanaka, T. Nakayama. Low-Temperature Epitaxial-Growth of Cerium Dioxide Layers on (111) Silicon Substrates. *Journal of Applied Physics*, 69:8313–8315, 1991.

[157] S. Y. Zheng, A. M. Anderssonfaldt, B. Stjerna, C. G. Granqvist. Optical-Properties of Sputter-Deposited Cerium Oxyfluoride Thin-Films. *Applied Optics*, 32:6303–6309, 1993.

[158] H. J. Beie, A. C. Gnorich. Oxygen Gas Sensors Based on CeO_2 Thick and Thin-Films. *Sensors and Actuators B-Chemical*, 4:393–399, 1991.

[159] R. G. Schwab, R. A. Steiner, G. Mages, H. J. Beie. Properties of CeO_2 and CeO_{2-x} films. 2. High-temperature properties. *Thin Solid Films*, 207:288–293, 1992.

[160] G. A. Deluga, J. R. Salge, L. D. Schmidt, X. E. Verykios. Renewable hydrogen from ethanol by autothermal reforming. *Science*, 303:993–997, 2004.

[161] ISI Web of Knowledge. http://www.isiknowledge.com. *Internet Resource*.

[162] A. Trovarelli. *Structural properties and nonstoichiometric behavior of CeO_2*, volume 2 series *Catalytic Science Series*. Imperial College Press, 2002.

[163] Q. Fu, H. Saltsburg, M. Flytzani-Stephanopoulos. Active nonmetallic Au and Pt species on ceria-based water-gas shift catalysts. *Science*, 301:935–938, 2003.

[164] J. B. Park, J. Graciani, J. Evans, D. Stacchiola, S. D. Senanayake, L. Barrio, P. Liu, J. F.. Sanz, J. Hrbek, J. A. Rodriguez. Gold, Copper, and Platinum Nanoparticles Dispersed on CeO_x/TiO_2(110) Surfaces: High Water-Gas Shift Activity and the Nature of the Mixed-Metal Oxide at the Nanometer Level. *Journal of the American Chemical Society*, 132:356–363, 2010.

[165] A. Pfau, K. D. Schierbaum. The Electronic-Structure of Stoichiometric and Reduced CeO_2 Surfaces - An XPS, UPS and HREELS Study. *Surface Science*, 321:71–80, 1994.

[166] J.-L. Lu, H.-J. Gao, S. Shaikhutdinov, H.-J. Freund. Gold supported on well-ordered ceria films: nucleation, growth and morphology in CO oxidation reaction. *Catalysis Letters*, 114:8–16, 2007.

[167] P. A. Cox. *Transition Metal Oxides*. Clarendon Press, 1992.

[168] N.V. Skorodumova, S.I. Simak, B.I. Lundqvist, I.A. Abrikosov, B. Johansson. Quantum origin of the oxygen storage capability of ceria. *Physical Review Letters*, 89:166601, 2002.

[169] T. Ami, Y. Ishida, N. Nagasawa, A. Machida, M. Suzuki. Room-temperature epitaxial growth of CeO_2(001) thin films on Si(001) substrates by electron beam evaporation. *Applied Physics Letters*, 78:1361–1363, 2001.

[170] T. Chikyow, S. M. Bedair, L. Tye, N. A. Elmasry. Reaction and Regrowth Control of CeO_2 on Si(111) Surface for the Silicon-on-Insulator Structure. *Applied Physics Letters*, 65:1030–1032, 1994.

[171] S. Yaegashi, T. Kurihara, H. Hoshi, H. Segawa. Epitaxial-Growth of CeO_2 Films on Si(111) by Sputtering. *Japanese Journal of Applied Physics*, 33:270–274, 1994.

[172] D. P Norton, J. D. Budai, M. F. Chisholm. Hydrogen-assisted pulsed-laser deposition of (001) CeO_2 on (001) Ge. *Applied Physics Letters*, 76:1677–1679, 2000.

[173] C. Y. Tian, Y. Du, S. W. Chan. Preparation and microstructural study of CeO_2 thin films. *Journal of Vacuum Science and Technology A-Vacuum Surfaces and Films*, 15:85–92, 1997.

[174] M. Alexandrou, R. M. Nix. The Growth, Structure and Stability of Ceria Overlayers on Pd(111). *Surface Science*, 321:47–57, 1994.

[175] A. G. Zaitsev, G. Ockenfuss, D. Guggi, R. Wordenweber, U. Kruger. Structural perfection of (001) CeO_2 thin films on (1102) sapphire. *Journal of Applied Physics*, 81:3069–3072, 1997.

[176] R. P. Wang, Y. L. Zhou, S. H. Pan, H. Zhang, X. X. Guo, X. M. Xiong, H. B. Lu, Z. H. Zhen, G. Z. Yang. Structural characteristics of CeO_2 films grown on biaxially textured nickel (001). *Journal of Applied Physics*, 84:1994–1997, 1998.

[177] D. R. Mullins, S. H. Overbury, D. R. Huntley. Electron spectroscopy of single crystal and polycrystalline cerium oxide surfaces. *Surface Science*, 409:307–319, 1998.

[178] C. Hardacre, G. M. Roe, R. M. Lambert. Structure, Composition and Thermal-Properties of Cerium Oxide-Films on Platinum(111). *Surface Science*, 326:1–10, 1995.

[179] D. R. Mullins, P. V. Radulovic, S. H. Overbury. Ordered cerium oxide thin films grown on Ru(0001) and Ni(111). *Surface Science*, 429:186–198, 1999.

[180] D. N. Belton, S. J. Schmieg. Low-Temperature Oxidation and Reduction of Ceria Particles on Rh(111). *Journal of Vacuum Science and Technology A-Vacuum Surfaces and Films*, 11:2330–2335, 1993.

[181] S. Eck, C. Castellarin-Cudia, S. Surnev, M. G. Ramsey, F. P. Netzer. Growth and thermal properties of ultrathin cerium oxide layers on Rh(111). *Surface Science*, 520:173–185, 2002.

[182] K. D. Schierbaum. Ordered ultra-thin cerium oxide overlayers on Pt(111) single crystal surfaces studied by LEED and XPS. *Surface Science*, 399:29–38, 1998.

[183] F. Sutara, M. Cabala, L. Sedlacek, T. Skala, M. Skoda, V. Matolin, K. C. Prince, V. Chab. Epitaxial growth of continuous CeO_2 (111) ultra-thin films on Cu(111). *Thin Solid Films*, 516:6120–6124, 2008.

[184] M. Baron. *Untersuchung Ceroxid-basierter Modellkatalysatoren*. PhD thesis, Humboldt-Universität zu Berlin, 2010.

[185] J.-L. Lu, H.-J. Gao, S. Shaikhutdinov, H.-J. Freund. Morphology and defect structure of the CeO_2(111) films grown on Ru(0001) as studied by scanning tunneling microscopy. *Surface Science*, 600:5004–10, 2006.

[186] E. Bauer. Phänomenologische Theorie der Kristallabscheidung an Oberflächen. *Zeitschrift für Kristallographie*, 110:372–394, 1958.

[187] M. Nolan, S. Grigoleit, D. C. Sayle, S. C. Parker, G. W. Watson. Density functional theory studies of the structure and electronic structure of pure and defective low index surfaces of ceria. *Surface Science*, 576:217–229, 2005.

[188] M. Fronzi, A. Soon, B. Delley, E. Traversa, C. Stampfl. Stability and morphology of cerium oxide surfaces in an oxidizing environment: a first-principles investigation. *Journal of Chemical Physics*, 131:104701, 2009.

[189] E. Bauer, J. H. Vandermerwe. Structure and growth of crystalline superlattices - from monolayer to superlattice. *Physical Review B*, 33:3657–3671, 1986.

[190] H. M. Benia, P. Myrach, N. Nilius, H. J. Freund. Structural and electronic characterization of the MgO/Mo(001) interface using STM. *Surface Science*, 604:435–441, 2010.

[191] D. M. Meadows, W. O. Johnson, J. B. Allen. Generation of Surface Contours by Moire Patterns. *Applied Optics*, 9:942, 1970.

[192] S. J. Altenburg, J. Kröger, B. Wang, M.-L. Bocquet, N. Lorente, R. Berndt. Graphene on Ru(0001): Contact Formation and Chemical Reactivity on the Atomic Scale. *Physical Review Letters*, 105:236101, 2010.

[193] C. Castellarin-Cudia, S. Surnev, G. Schneider, R. Podlucky, M. G. Ramsey, F. P. Netzer. Strain-induced formation of arrays of catalytically active sites at the metal-oxide interface. *Surface Science*, 554:L120–L126, 2004.

[194] F. Esch, S. Fabris, L. Zhou, T. Montini, C. Africh, P. Fornasiero, G. Comelli, R. Rosei. Electron localization determines defect formation on ceria substrates. *Science*, 309:752–755, 2005.

[195] A. Trovarelli. Catalytic properties of ceria and CeO_2 containing materials. *Catalysis Reviews - Science and Engineering*, 38:439–520, 1996.

[196] E. Paparazzo. XPS Studies of Damage Induced by X-Ray-Irradiation on CeO_2 Surfaces. *Surface Science*, 234:L253–L258, 1990.

[197] W. D. Xiao, Q. L. Guo, E. G. Wang. Transformation of $CeO_2(111)$ to $Ce_2O_3(0001)$ films. *Chemical Physics Letters*, 368:527–531, 2003.

[198] E. Wuilloud, B. Delley, W. D. Schneider, Y. Baer. Spectroscopic Evidence for Localized and Extended *F*-Symmetry States In CeO_2. *Physical Review Letters*, 53:202–205, 1984.

[199] S. Torbruegge, M. Reichling, A. Ishiyama, S. Morita, O. Custance. Evidence of subsurface oxygen vacancy ordering on reduced $CeO_2(111)$. *Physical Review Letters*, 99:056101, 2007.

[200] S. Benedetti, P. Torelli, S. Valeri, H. M. Benia, N. Nilius, G. Renaud. Structure and morphology of thin MgO films on Mo(001). *Physical Review B*, 78:195411, 2008.

[201] S. Torbrugge, M. Cranney, M. Reichling. Morphology of step structures on $CeO_2(111)$. *Applied Physics Letters*, 93:073112, 2008.

[202] D. D. Koelling, A. M. Boring, J. H. Wood. The Electronic-Structure of CeO_2 and PrO_2. *Solid State Communications*, 47:227–232, 1983.

[203] P. Wachter. Empty *f*-states, Kondo insulators - or what? *Physica B-Condensed Matter*, 300:105–120, 2001.

[204] P. Wachter, H. Boppart, editors. *Valence Instabilities. Proceedings of the International Conference*, Amsterdam, Netherlands, 1982. North-Holland. 13-16 April 1982, Zurich, Switzerland.

[205] A. Fujimori. Mixed-Valent Ground-State of CeO_2. *Physical Review B*, 28:2281–2283, 1983.

[206] J. W. Allen. Valence Fluctuations in Narrow-Band Oxides. *Journal of Magnetism and Magnetic Materials*, 47-8:168–174, 1985.

[207] M. Matsumoto, K. Soda, K. Ichikawa, S. Tanaka, Y. Taguchi, K. Jouda, O. Aita, Y. Tezuka, S. Shin. Resonant Photoemission-Study of CeO_2. *Physical Review B*, 50:11340–11346, 1994.

[208] T. Hanyu, H. Ishii, M. Yanagihara, T. Kamada, T. Miyahara, H. Kato, K. Naito, S. Suzuki, T. Ishii. On the Valence States of Cerium in CeO_2. *Solid State Communications*, 56:381–383, 1985.

[209] H. Dexpert, R. C. Karnatak, J. M. Esteva, J. P. Connerade, M. Gasgnier, P. E. Caro, L. Albert. X-Ray Absorption Studies of CeO_2, PrO_2, and TbO_2. II. Rare-earth Valence State By L_{iii} Absorption Edges. *Physical Review B*, 36:1750–1753, 1987.

[210] R. C. Karnatak, J. M. Esteva, H. Dexpert. X-Ray Absorption Studies of CeO_2, PrO_2, and TbO_2. 1. Manifestation of Localized and Extended f-States in the $3d$-Absorption-Spectra. *Physical Review B*, 36:1745–1749, 1987.

[211] F. Marabelli, P. Wachter. Covalent Insulator CeO_2 - Optical Reflectivity Measurements. *Physical Review B*, 36:1238–1243, 1987.

[212] A. Fujimori. Correlation effects in the electronic structure and photoemission spectra of mixed valence Cerium compounds. *Physical Review B*, 28:4489–4499, 1983.

[213] A. Fujimori. $4f$ level and core level photoemission satellites in Cerium compounds. *Physical Review B*, 27:3992–4001, 1983.

[214] G. Kaindl, G. K. Wertheim, G. Schmiester, E. V. Sampathkumaran. Mixed Valency Versus Covalency In Rare-Earth Core-Electron Spectroscopy. *Physical Review Letters*, 58:606–609, 1987.

[215] R. M. Feenstra. Tunneling Spectroscopy of the (110)-Surface of Direct-Gap iii-V Semiconductors. *Physical Review B*, 50:4561–4570, 1994.

[216] S. L. Dudarev, M. R. Castell, G. A. Botton, S. Y. Savrasov, C. Muggelberg, G. A. D. Briggs, A. P. Sutton, D. T. Goddard. Understanding STM images and EELS spectra of oxides with strongly correlated electrons: a comparison of nickel and uranium oxides. *Micron*, 31:363–372, 2000.

[217] N. Nilius, T. M. Wallis, M. Persson, W. Ho. Distance dependence of the interaction between single atoms: Gold dimers on NiAl(110). *Physical Review Letters*, 90:196103, 2003.

[218] M. Grobis, A. Wachowiak, R. Yamachika, M. F. Crommie. Tuning negative differential resistance in a molecular film. *Applied Physics Letters*, 86, 2005.

[219] S. Fabris, G. Vicario, G. Balducci, S. de Gironcoli, S. Baroni. Electronic and atomistic structures of clean and reduced ceria surfaces. *Journal of Physical Chemistry B*, 109:22860–22867, 2005.

[220] M. V. Ganduglia-Pirovano, J. L. F. Da Silva, J. Sauer. Density-Functional Calculations of the Structure of Near-Surface Oxygen Vacancies and Electron Localization on $CeO_2(111)$. *Physical Review Letters*, 102:026101, 2009.

[221] H.-Y. Li, H.-F. Wang, X.-Q. Gong, Y.-L. Guo, Y. Guo, G. Lu, P. Hu. Multiple configurations of the two excess $4f$ electrons on defective $CeO_2(111)$: Origin and implications. *Physical Review B*, 79:193401, 2009.

[222] C. Zhang, A. Michaelides, D. A. King, S. J. Jenkins. Oxygen vacancy clusters on ceria: Decisive role of cerium f electrons. *Physical Review B*, 79:075433, 2009.

[223] C. Loschen, S. T. Bromley, K. M. Neyman, F. Illas. Understanding ceria nanoparticles from first-principles calculations. *Journal of Physical Chemistry C*, 111:10142–10145, 2007.

[224] A. Migani, K.M. Neyman, F. Illas, S.T. Bromley. Exploring Ce^{3+}/Ce^{4+} cation ordering in reduced ceria nanoparticles using interionic-potential and density-functional calculations. *Journal of Chemical Physics*, 131:064701, 2009.

[225] D. C. Grinter, R. Ithnin, C. L. Pang, G. Thornton. Defect Structure of Ultrathin Ceria Films on Pt(111): Atomic Views from Scanning Tunnelling Microscopy. *Journal of Physical Chemistry C*, 114:17036–17041, 2010.

[226] J.-F. Jerratsch, X. Shao, N. Nilius, H.-J. Freund, C. Popa, M. V. Ganduglia-Pirovano, A. M. Burow, J. Sauer. Electron localization in defective ceria films: An STM and DFT study. *submitted*, 2011.

[227] M. Baron, H. Abbott, O. Bondarchuk, D. Stacchiola, A. Uhl, S. Shaikhutdinov, H.-J. Freund, C. Popa, M. V. Ganduglia-Pirovano, J. Sauer. Resolving the Atomic Structure of Vanadia Monolayer Catalysts: Monomers, Trimers, and Oligomers on Ceria. *Angewandte Chemie-International Edition*, 48:8006–8009, 2009.

[228] Joachim Sauer. Direct communication.

[229] P. Johansson, R. Monreal, P. Apell. Theory for light emission from a scanning tunneling microscope. *Physical Review B*, 42:9210–9213, 1990.

[230] J. M. Pitarke, F. Flores, P. M. Echenique. Tunneling Spectroscopy - Surface Geometry and Interface Potential Effects. *Surface Science*, 234:1–16, 1990.

[231] J. P. Perdew, J. A. Chevary, S. H. Vosko, K. A. Jackson, M. R. Pederson, D. J. Singh, C. Fiolhais. Atoms, Molecules, Solids, and Surfaces - Applications of the Generalized Gradient Approximation for Exchange and Correlation. *Physical Review B*, 48:4978, 1993.

[232] G. Kresse, J. Furthmuller. Efficiency of ab-initio total energy calculations for metals and semiconductors using a plane-wave basis set. *Computational Materials Science*, 6:15–50, 1996.

[233] H. Nörenberg, G. A. D. Briggs. Defect Structure of Nonstoichiometric CeO_2(111) Surfaces Studied by Scanning Tunneling Microscopy. *Physical Review Letters*, 79:4222–4225, 1997.

[234] J. A. Farmer, C. T. Campbell. Ceria Maintains Smaller Metal Catalyst Particles by Strong Metal-Support Bonding. *Science*, 329:933–936, 2010.

[235] T. König, G. H. Simon, H.-P. Rust, G. Pacchioni, M. Heyde, H.-J. Freund. Measuring the Charge State of Point Defects on MgO/Ag(001). *Journal of the American Chemical Society*, 131:17544–17545, 2009.

[236] J. W. Yan, Z. X. Xie, Z. X. Cao, C. J. Zhou, J. Y. Kang, B. W. Mao. Formation and STM tip-induced reduction of ultra thin SnO film on Au(111). *Chemical Physics Letters*, 373:575–579, 2003.

[237] F. S. S. Chien, J. W. Chang, S. W. Lin, Y. C. Chou, T. T. Chen, S. Gwo, T. S. Chao, W. F. Hsieh. Nanometer-scale conversion of Si_3N_4 to SiO_x. *Applied Physics Letters*, 76:360–362, 2000.

[238] P. Ebert, M. G. Lagally, K. Urban. Scanning-Tunneling-Microscope Tip-Induced Migration of Vacancies on GAP(110). *Physical Review Letters*, 70:1437–1440, 1993.

[239] D. M. Eigler, E. K. Schweizer. Positioning Single Atoms with a Scanning Tunneling Microscope. *Nature*, 344:524–526, 1990.

[240] S. W. Hla, L. Bartels, G. Meyer, K. H. Rieder. Inducing all steps of a chemical reaction with the scanning tunneling microscope tip: Towards single molecule engineering. *Physical Review Letters*, 85:2777–2780, 2000.

[241] M. Baron, J.-F. Jerratsch, X. Shao, J.-L. Lu, F. Vines Solana, K.M. Neyman, N. Nilius, S. Shaikhutdinov, H.-J. Freund. Structural and electronic properties of step edges in CeO_2(111) films. *in preparation*.

[242] M. Sterrer, M. Heyde, M. Novicki, N. Nilius, T. Risse, H. P. Rust, G. Pacchioni, H.-J. Freund. Identification of color centers on MgO(001) thin films with scanning tunneling microscopy. *Journal of Physical Chemistry B*, 110:46–49, 2006.

[243] M. M. Branda, C. Loschen, K. M. Neyman, F. Illas. Atomic and Electronic Structure of Cerium Oxide Stepped Model Surfaces. *Journal of Physical Chemistry C*, 112:17643–17651, 2008.

[244] M.V. Bollinger, V. Lauritsen, K.W. Jacobsen, J.K. Norskov, S. Helveg, F. Besenbacher. One-dimensional metallic edge states in MoS_2. *Physical Review Letters*, 87:196803, 2001.

[245] J. Goniakowski, F. Finocchi, C. Noguera. Polarity of oxide surfaces and nanostructures. *Reports on Progress in Physics*, 71:016501, 2008.

[246] M. Schmid, M. Shishkin, G. Kresse, E. Napetschnig, P. Varga, M. Kulawik, N. Nilius, H. P. Rust, H.-J. Freund. Oxygen-deficient line defects in an ultrathin aluminum oxide film. *Physical Review Letters*, 97:046101, 2006.

[247] M. C. Shekar, V. H. Babu. Dielectric-Properties of Vacuum-Deposited Cerium Oxide-Films. *Journal of Materials Science Letters*, 3:600–604, 1984.

[248] A. Khodakov, B. Olthof, A. T. Bell, E. Iglesia. Structure and catalytic properties of supported vanadium oxides: Support effects on oxidative dehydrogenation reactions. *Journal of Catalysis*, 181:205–216, 1999.

[249] A. Dinse, B. Frank, C. Hess, D. Habel, R. Schomacker. Oxidative dehydrogenation of propane over low-loaded vanadia catalysts: Impact of the support material on kinetics and selectivity. *Journal of Molecular Catalysis A-Chemical*, 289:28–37, 2008.

[250] W. Daniell, A. Ponchel, S. Kuba, F. Anderle, T. Weingand, D. H. Gregory, H. Knozinger. Characterization and catalytic behavior of VO_x-CeO_2 catalysts for the oxidative dehydrogenation of propane. *Topics In Catalysis*, 20:65–74, 2002.

[251] M. V. Ganduglia-Pirovano, C. Popa, J. Sauer, H. Abbott, A. Uhl, M. Baron, D. Stacchiola, O. Bondarchuk, S. Shaikhutdinov, H.-J. Freund. Role of Ceria in Oxidative Dehydrogenation on Supported Vanadia Catalysts. *Journal of the American Chemical Society*, 132:2345–2349, 2010.

[252] O. Echt, K. Sattler, E. Recknagel. Magic numbers for sphere packings: Experimental verification in free xenon clusters. *Physical Review Letters*, 47:1121–1124, 1981.

[253] J. Schoiswohl, G. Kresse, S. Surnev, M. Sock, M. G. Ramsey, F. P. Netzer. Planar vanadium oxide clusters: two-dimensional evaporation and diffusion on Rh(111). *Physical Review Letters*, 92:206103, 2004.

[254] F. P. Netzer. Small and beautiful - The novel structures and phases of nano-oxides. *Surface Science*, 604:485–489, 2010.

[255] J. Schoiswohl, S. Surnev, F. P. Netzer, G. Kresse. Vanadium oxide nanostructures: from zero- to three-dimensional. *Journal of Physics-Condensed Matter*, 18:R1–R14, 2006.

[256] D. Löffler, J. J. Uhlrich, M. Baron, B. Yang, X. Yu, L. Lichtenstein, L. Heinke, C. Büchner, M. Heyde, S. Shaikhutdinov, H.-J. Freund, R. Włodarczyk, M. Sierka, J. Sauer. Growth and Structure of Crystalline Silica Sheet on Ru(0001). *Physical Review Letters*, 105:146104, 2010.

List of Figures

Curriculum Vitae

For reasons of data protection,
the curriculum vitae is not included in the online version

List of Publications

1. Umberto Martinez, Jan-Frederik Jerratsch, Niklas Nilius, Livia Giordano, Gianfranco Pacchioni and Hans-Joachim Freund. Tailoring the Interaction Strength between Gold Particles and Silica Thin Films via Work Function Control. *Physical Review Letters*, 103: 056801 (2009).

2. Jan-Frederik Jerratsch, Niklas Nilius, Hans-Joachim Freund, Umberto Martinez, Livia Giordano and Gianfranco Pacchioni. Lithium incorporation into a silica thin film: Scanning tunneling microscopy and density functional theory. *Physical Review B*, 80: 245423 (2009).

3. Jan-Frederik Jerratsch, Niklas Nilius, Dinesh Topwal, Umberto Martinez, Livia Giordano, Gianfranco Pacchioni and Hans-Joachim Freund. Stabilizing Monomeric Iron Species in a Porous Silica/Mo(112) Film. *ACS Nano*, 4: 863 (2010).

4. Jan-Frederik Jerratsch, Xiang Shao, Niklas Nilius, Cristina Popa, M. Veronica Ganduglia-Pirovano, Hans-Joachim Freund, Asbjörn M. Burow and Joachim Sauer. Electron localization in defective ceria films: An STM and DFT study. *Submitted* (2011).

5. Xiang Shao, Jan-Frederik Jerratsch, Niklas Nilius and Hans-Joachim Freund. Probing the f-states of Ceria by tunneling spectroscopy. *In preparation* (2011).

6. Martin Baron, Jan-Frederik Jerratsch, Xiang Shao, Jun-Ling Lu, Francesc Vines, Konstantin M. Neyman, Niklas Nilius, Shamil Shaikhutdinov and Hans-Joachim Freund. Structural and electronic properties of step edges in CeO_2(111) films. *In preparation* (2011).

7. Jan-Frederik Jerratsch, Xiang Shao, Niklas Nilius and Hans-Joachim Freund. Vanadium deposition on CeO_2(111) thin films. *In preparation* (2011).

8. Dinesh Topwal, Manju Unnikrishnan, Sandra Gardonio, Jan-Frederik Jerratsch, Niklas Nilius and Carlo Carbone. Iron atoms in a porous silca film grown on Mo(112) investigated with photoelectron emission spectroscopy. *In preparation* (2011).

Conference Contributions

1. Annual Meeting of the COST Action D41: Inorganic Oxides: Surfaces and Interfaces. Talk: *Modifying the adsorption characteristics of SiO$_2$ on Mo(112) by inserting specific surface anchors*. Barcelona, Spain (2008).

2. Jahrestagung der deutschen physikalischen Gesellschaft. Talk: *Tailoring the adsorption properties of SiO$_2$ thin films*. Dresden, Germany (2009)

3. Annual Meeting of the COST Action D41: Inorganic Oxides: Surfaces and Interfaces. Talk: *The SiO$_2$ thin-film: a template for single-atom magnetic units*. Paris, France (2009).

4. Forschungsseminar der Arbeitsgruppe Prof. Dr. José Ignacio Pascual. Talk: *Tailoring the properties of oxide thin films: SiO$_2$ - An STM case study*. Berlin, Germany (2010).

5. European Conference on Surface Science. Talk: *Probing filled and empty Ce 4f-states in thin Ceria films at the atomic level*. Groningen, Netherlands (2010).

Invited Talk

1. JungChemikerForum Berlin. Talk: *Tracing catalytic properties down to the atomic level: Oxygen vacancies in ceria*. Berlin, Germany (2011).

Acknowledgements

I want to thank everybody who contributed to the success of this thesis.

First of all I am deeply thankful to Prof. Dr. Hans-Joachim Freund for giving me the oppotunity to work in his department and for providing all the means necessary to perform the experiments for this thesis and for his scientific guidiance.

I am very thankful to Prof. Dr. José Ignacio Pascual for agreeing to referee this thesis and for giving me the opportunity to present the progress of my work in his research seminar.

A special thanks goes to Dr. Niklas Nilius for his truly tireless support throughout all stages of this thesis. His vast knowledge and experience made the success of this thesis possible.

I am very grateful for the fruitful colaboration with the theory groups of Prof. Dr. Pacchioni in Milano and of Prof. Dr. Sauer in Berlin.

Beyond that I would like to thank all current and former members of the scanning probe spectroscopy group for all the fruitful discussions and hands-on support in the lab, especially Dr. Xiang Shao, Stefan Ulrich, Dr. Philipp Myrach, Dr. Hadj Mohammed Benia, Dr. Shao Lin, Dr. Bing Yang, Dr. Fernando Stavale and Yi Pan.

I am also thankful to all members of the Department of Chemical Physics of the Fritz-Haber-Institute and the International Max Planck Research School for Complex Surfaces in Materials Science for fruitful discussions and enjoyable three years at the institute.

Furthermore I would like to thank Klaus-Peter Vogelgesang and all members of the workshops of the Fritz-Haber-Institute for their quick and competent support.

Selbständigkeitserklärung

Ich erkläre, dass ich die vorliegende Arbeit selbständig und nur unter Verwendung der angegebenen Literatur und Hilfsmittel angefertigt habe.

Berlin, den 03.03.2011

Jan-Frederik Jerratsch